A Critical Assessment of the Effects of Pulsed Irradiation on Materials

N.M. Ghoniem and G.L. Kulcinski

August 19, 1979

UWFDM-311

Nucl. Technology/Fusion 2, 165 (1978).

FUSION TECHNOLOGY INSTITUTE

UNIVERSITY OF WISCONSIN

MADISON WISCONSIN

A Critical Assessment of the Effects of Pulsed Irradiation on Materials

N.M. Ghoniem and G.L. Kulcinski

Fusion Technology Institute
University of Wisconsin
1500 Engineering Drive
Madison, WI 53706

http://fti.neep.wisc.edu

August 19, 1979

UWFDM-311

Nucl. Technology/Fusion 2, 165 (1978).

A CRITICAL ASSESSMENT OF THE EFFECTS OF PULSED IRRADIATION ON MATERIALS

N. M. Ghoniem
School of Engineering and Applied Science, UCLA
Los Angeles, CA 90024

G. L. Kulcinski
Nuclear Engineering Department, University of Wisconsin
Madison, WI 53706

August 10, 1979

UWFDM-311

1. INTRODUCTION

Several alternative approaches to the production of useful energy from controlled fusion have been proposed. However, difficulties in plasma confinement have resulted in a pulsed mode of operation for most of the fusion devices (with the possible exception of the mirror approach). A principal distinction between these approaches is the time scale over which the energy is released from the thermonuclear reaction. The duration and magnitude of this energy release will determine the response of materials which are used in the design of a fusion reactor. Of particular interest is the response of the first walls which directly face the plasma. The present paper reviews recent advances in theoretical and experimental investigations devoted to understanding the effects of pulsed irradiation on fusion reactor materials.

2. BACKGROUND

The complicated and interactive nature of fusion reactor design requires sound understanding of the behavior of irradiated materials for reliable and safe reactor operation. The rate at which atomic displacements are produced varies substantially from one fusion reactor concept to the other. Even within the same reactor, components are exposed to different damage rates. As an illustration of this point, Fig. (1) shows the damage rates expected in a variety of fusion reactor designs compared to the damage rate in a fission reactor like EBR-II. It is readily seen that the first wall and blanket receive most of the damage inflicted by thermonuclear radiation. On the other hand, the shield and magnets (or last

Figure 1

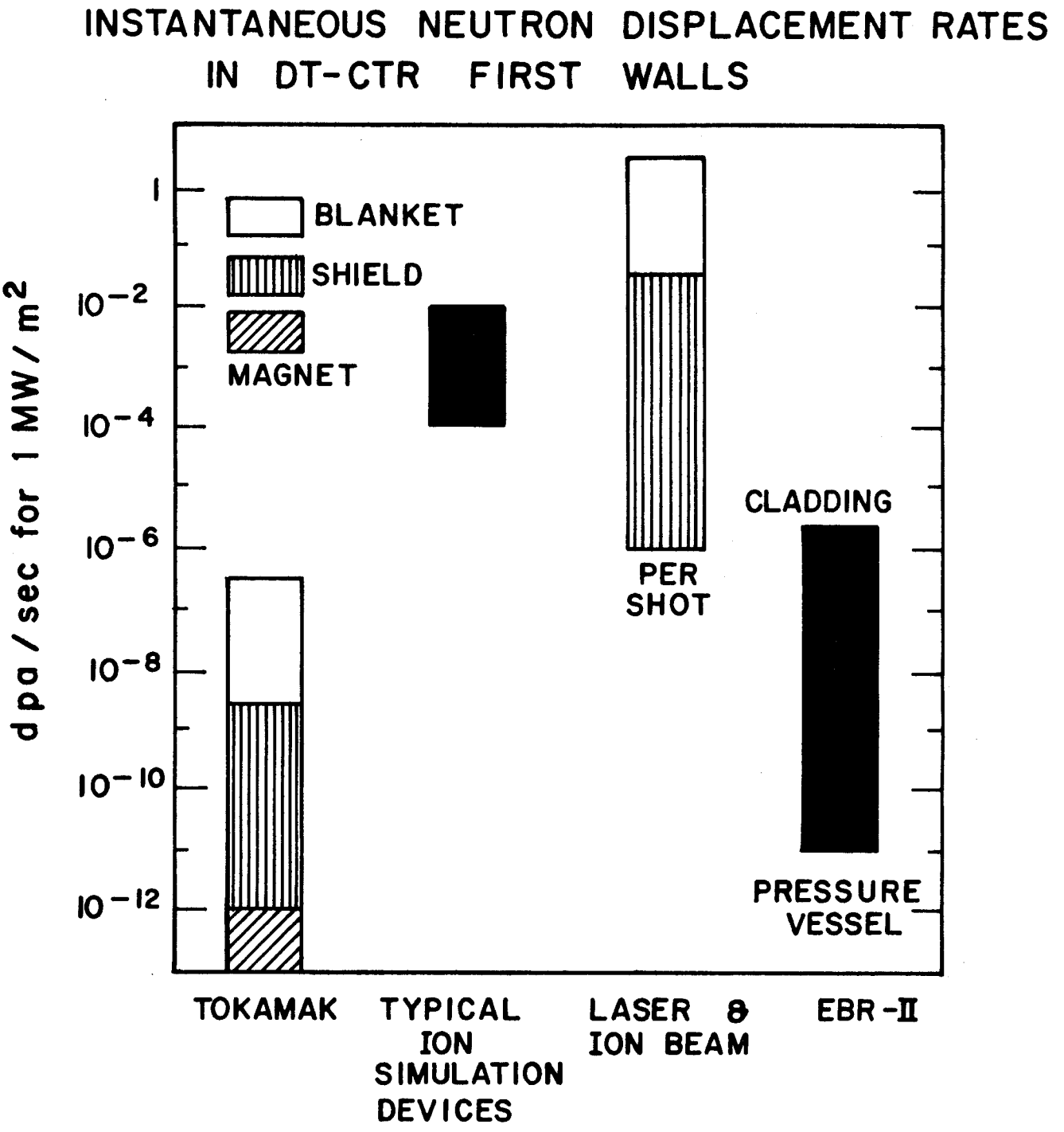
INSTANTANEOUS NEUTRON DISPLACEMENT RATES
IN DT-CTR FIRST WALLS
dpa / sec for 1 MW / m2
1
10-2
10-4
10-6
10-8
10-10
10-12
BLANKET
SHIELD
MAGNET
PER SHOT
CLADDING
PRESSURE VESSEL
TOKAMAK
TYPICAL ION SIMULATION DEVICES
LASER & ION BEAM
EBR-II

focussing elements in Inertial Confinement Fusion Reactors (ICFRs)) are exposed to lower levels of the damaging radiation. While most of the experience on the performance of materials in fission reactors is obtained with an average damage rate of 10^{-8} to 10^{-6} dpa/s, fusion reactors will encompass a wider range of displacement damage rates. Structural components in Tokamak and Mirror Fusion Reactors are expected to function under a dose rate of 10^{-12}-10^{-6} dpa/s. On the other hand, the first walls of ICFRs should be designed to handle instantaneous damage rates of 0.1 to 10 dpa/s. The interesting factor here is that the average displacement rate at the first wall (integrated over say 1 hour) of the various concepts is approximately the same even though the instantaneous rate is vastly different. We have also included in Fig. (1) the displacement rates normally experienced in simulation facilities such as Electron or Heavy Ion Accelerators that are designed to study the effects of pulsed radiation damage. In summary, instantaneous damage rates in the range of 10^{-12}–10 dpa/s are thus expected in fusion facilities.

The phenomenology associated with pulsed irradiation in a fusion environment is outlined in Fig. (2). It is first necessary to describe the irradiation source and the first wall concept. The primary pulsed fusion radiation source can usually be described by the spectra of neutrons, charged particles and photons produced in each pulse and transported to the point of consideration. The primary interaction of the source neutrons is with the target nuclei while the photon interaction is with the target electrons. Ions interact with both electrons and nuclei. The partitioning of interaction energy between nuclei and electrons is crucial to the ultimate response of the material. Only the nuclear energy losses will result in damage in the form of atomic displacements while the electronic energy

Figure 2

THEORETICAL AND CALCULATIONAL PROCEDURES FOR RESEARCH ON RADIATION DAMAGE IN PULSED SYSTEMS

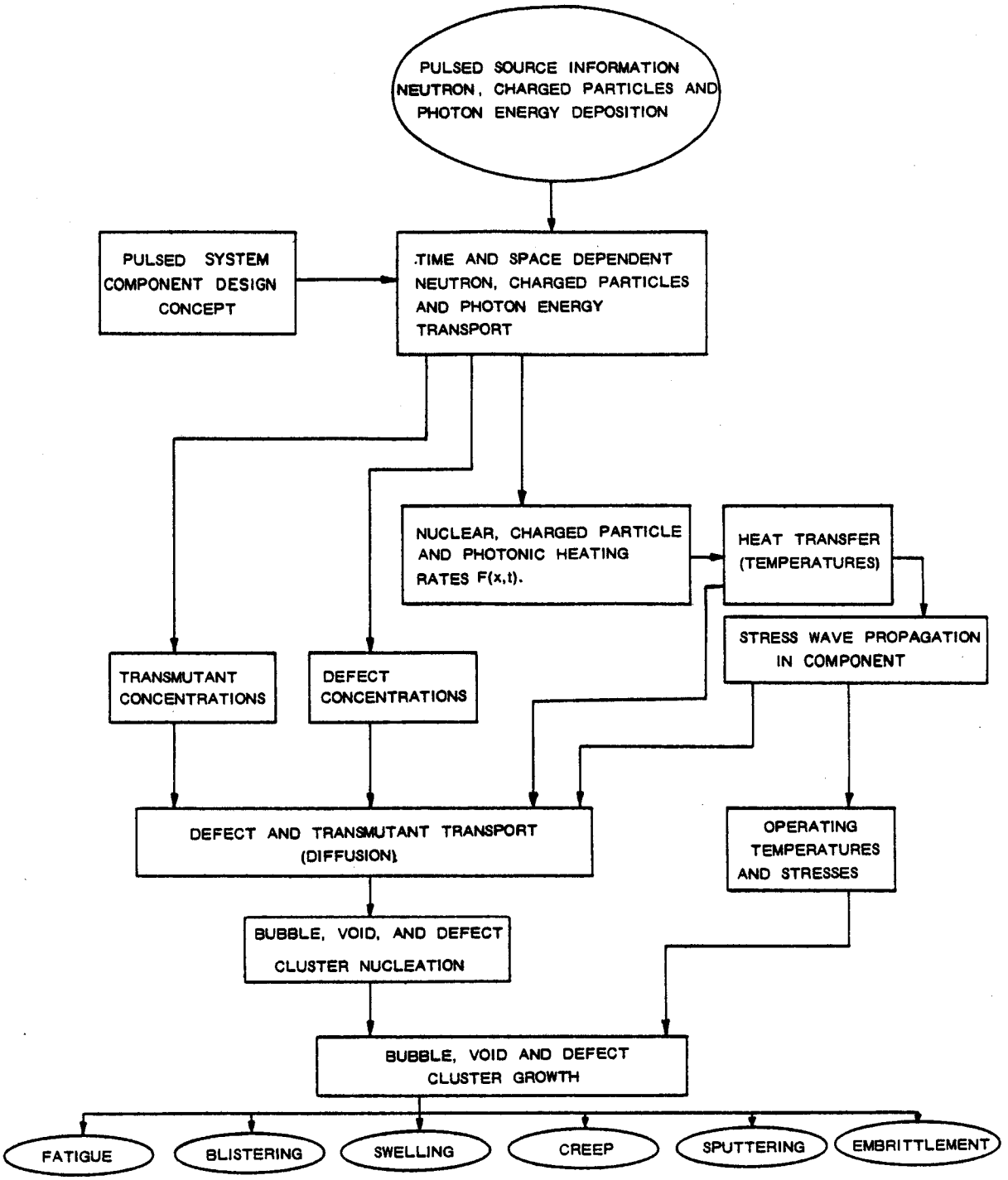

will (in the case of metals) mainly produce ionization leading to a local energy deposition (heat).

The nuclear energy transfers first appear as primary knock-ons (PKA's) which then produce subsequent displacements as they travel through the material. The resulting concentration of point defects (vacancies and interstitials) will undergo recombination, migration and agglomeration into submicroscopic and microscopic clusters. The accumulation of single and clustered defects can also result in macroscopic effects such as swelling, creep, blistering, embrittlement and loss of ductility. The ultimate life of the first wall and to a large degree the economics of fusion reactors, are determined by the deterioration of mechanical and physical properties due to these radiation induced phenomena.

The above processes do not occur independently from the thermodynamic state of the material, since the defect density is strongly influenced by the local temperature and stress state. The ultimate temperature history will be determined by the energy deposition time and the thermal response of the material, and an equilibrium operating temperature is approached following each energy pulse. Similarly, the stress history will be determined by the rate of energy deposition and the elastic response of the material.

In this paper, we will outline the recent progress in the area of pulsed irradiation effects on materials. First, a brief description of pulsed fusion reactors will be given in section 3, in order to define the boundary conditions of the various research topics in this rapidly progressing field. A discussion of the work on the primary damage state will then follow in section 4. The resultant energy deposition will appear as atom displacements and as local heat. Section 5 will analyze these temperature and stress transients. The state of knowledge on the

behavior of the microstructure during irradiation will then be outlined in section 6. The effects of pulsed irradiation on mechanical properties is given in section 7, and finally conclusions and recommendations are provided in section 8.

3. PULSED FUSION SYSTEMS

With the possible exception of mirrors, most confinement systems for thermonuclear fusion operate in a pulsed mode. Tokamak systems operate in a pseudo-steady state manner but they are probably limited in pulse duration to a few hundred seconds by impurity buildup in the plasma and the available magnetic flux for plasma current.

Inertial confinement systems, which include lasers, electron beams and ion beams, rely on the rapid deposition of energy in the periphery of a small fuel pellet. This energy will cause the pellet to be compressed and heated to thermonuclear conditions which will exist on the order of 1 to 10 nanoseconds before the pellet flies apart.

Conceptual design studies have been performed for each of the above confinement schemes [1-4]. A general comparison of the burn characteristics and neutron wall loading is shown in Table 1 and it reveals the widespread variation in time scales over which the systems operate.

The dynamic response of a first wall to pulsed radiation sources can only be significantly different from the steady state response if the duration of the irradiation pulse is smaller or the same order as the response time of interest. Consequently, the systems most likely to have significant dynamic response modes will be the inertial confinement approaches and most of the following discussion will address the phenomenology associated with these systems.

TABLE 1

PULSED FUSION SOURCE CHARACTERISTICS FROM TYPICAL FUSION REACTOR DESIGNS

	Mirror[2]	Tokamak[3]	Laser[4]
Thermonuclear Burn Time (sec)	$2\text{-}3\times10^{6}$	225	10^{-11} - 10^{-10}
Thermonuclear Energy/pulse (GJ)	$4\text{-}6\times10^{6}$	470	0.10
Wall Area (m^2)	980	360	310
Ave. 14 MeV Fluence/pulse (n/cm^2)	2×10^{20}	4×10^{16}	1.1×10^{13}
Peak Wall Flux (n/cm^2 sec)	9×10^{13}	1.9×10^{14}	1.0×10^{21}
Time Between Burns (sec)	$\sim10^{5}$	20	~0.1
Average 14 MeV Neutron Wall Loading (MW/m^2)	2.0	4	2.5

The significance of such dynamic behavior is that many materials phenomena are quite sensitive to the rate at which the damage is produced. A qualitative comparison of displacement rates in metals for various environments in which displacement damage has been observed or is anticipated is given in Table 2. Aside from the fact that damage is produced in ICFRs at a rate 10^{6} to 10^{7} times faster than in fission reactors or magnetically confined fusion plasma reactors, the time structure is also quite different. Damage is produced at very high rates for a short interval of time in an ICFR followed by a quiescent phase in which the material is free to recover with no further damage being produced. Both the duration of the pulse and the interval between pulses can be of the same order as the lifetime of the interstitials and vacancies whose migration ultimately determines the microstructure of an irradiated material. In addition, the defect migration is occurring during a period in which the temperature is oscillating with the frequency of the radiation pulses.

TABLE 2 [5,6]

COMPARISON OF INSTANTANEOUS DISPLACEMENT RATES IN SOLID COMPONENTS OF NUCLEAR SYSTEMS

	dpa/sec
Tokamak or Mirror Fusion First Wall	3×10^{-7}
Thermal Fission Reactor Cladding	10^{-7}
Fast Fission Reactor Cladding	10^{-6}
HV Electron Microscope	10^{-3}
Heavy Ion Bombardment	10^{-4} - 10^{-1}
Inertial Confinement Fusion Reactor First Wall*	1-10

*Neutrons only.

4. THE PRIMARY DAMAGE STATE

4.1 Neutron Damage

Several methods to calculate the neutron spectra from ICF targets have been reported. Southworth and Campbell [7] used collision probability theory to generate the spectrum. Using the Wigner Rational Approximation, the escaping flux is determined as the sum of the uncollided flux and the first and second collided fluxes. They note that 20% of the neutrons are downscattered in an equimolar DT pellet with $\rho R = 2$ g/cm^2 (ICF pellets are often characterized by the term ρR, which is the product of the pellet density and the radius in the compressed state). Various assumptions are inherent in a calculation of this type, such as the assumption that the pellet density and neutron source are both spatially uniform and time independent, and that the interaction cross-sections are energy and angle independent. A Monte Carlo code, SPECIFIC II, has been used by Beynon and Constantine [8] to generate a spectrum from a pellet with $\rho R = 1.2$ g/cm^2. The result for this case, employing a steady state technique with a uniform source is that less than 1% of the neutrons are downscattered.

Beranek and Conn [9] studied the effects of neutron moderation on the ICF reactor vessel damage and radioactivity inventory. The neutron pellet spectra is obtained using a modified form of time-dependent discrete ordinate code, TDA [10]. The spatial profiles of the neutron source and pellet density are allowed to be both non-uniform in space and time-dependent. The interaction cross-sections are energy dependent (multigroup) and anisotropic. Neutron damage to a reactor chamber, both time-dependent and time-integrated, is shown to be significantly altered when moderation in the pellet is included.

Figure (3) shows the neutron energy spectra from bare and tamped pellets of the same $\rho R = 3\ g/cm^2$. It can be noticed that most of the neutrons hitting the first wall have energies in the 14 MeV range. However, a significant fraction is downscattered to lower energies. Softening of the spectra due to neutron fuel interactions causes a time-of-flight broadening of the neutron arrival time distribution at the chamber wall. Figure (4) shows the time history of the damage produced from one single pulse in dpa/s. Beranek and Conn concluded from their work that the total number of displacements per atom produced in a graphite first wall increases with the ρR of the pellet because of neutron multiplication. However, the total helium production was found to decrease with increasing ρR because the extra neutrons were born at energies below the threshold for helium production.

Finally, Ragheb and Lewis [11,12] have calculated the displacement rate in a stainless steel first wall placed 7 m from the pellet resulting from a pure 14.1 MeV neutron source. They determined the spectra from a pellet with a tungsten tamper and then the neutron spectrum after it has passed through a 50 cm

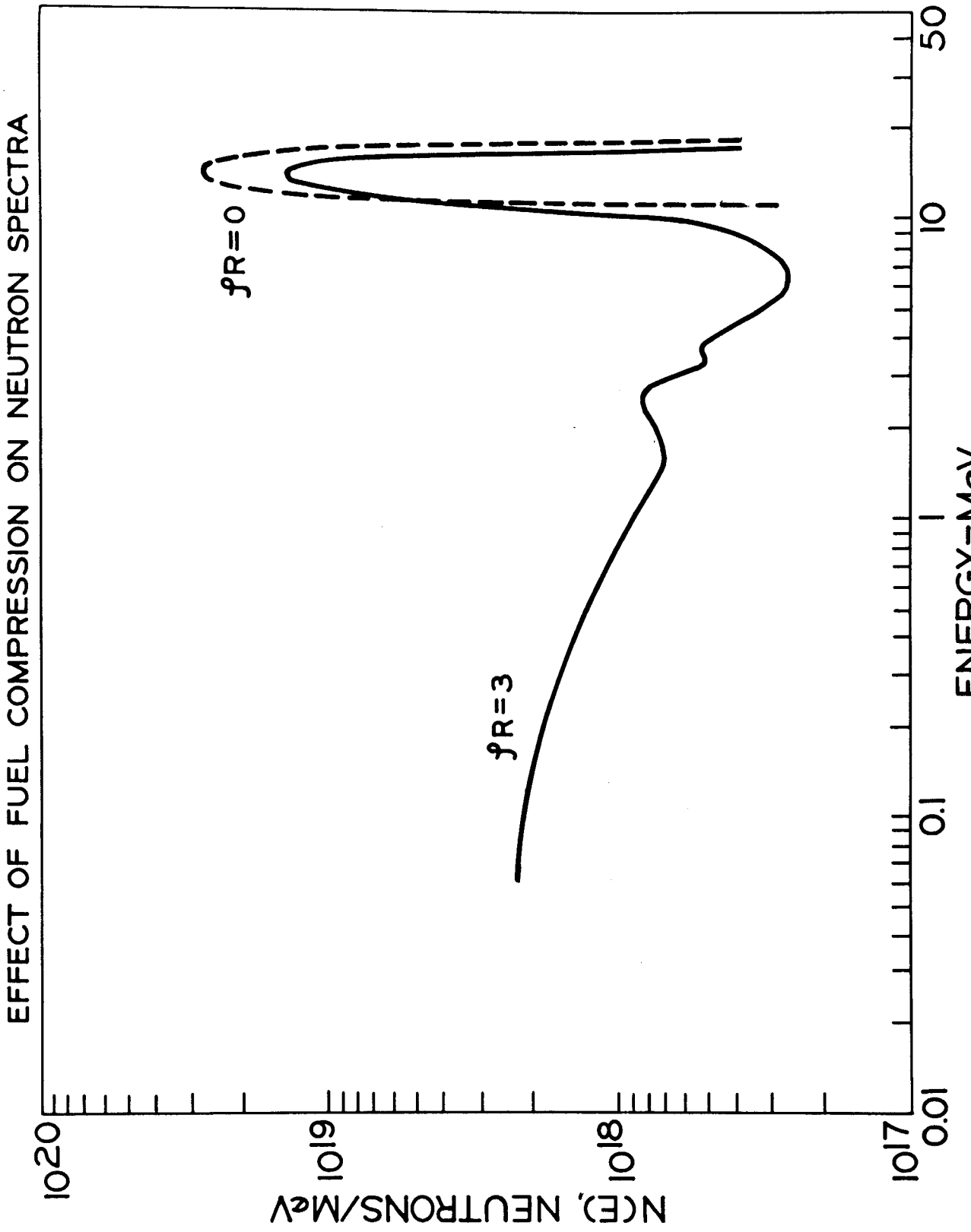
EFFECT OF FUEL COMPRESSION ON NEUTRON SPECTRA
ρR=0
ρR=3
N(E), NEUTRONS/MeV
ENERGY-MeV
10^20
10^19
10^18
10^17
0.01
0.1
1
10
50

Figure 3

Figure 4

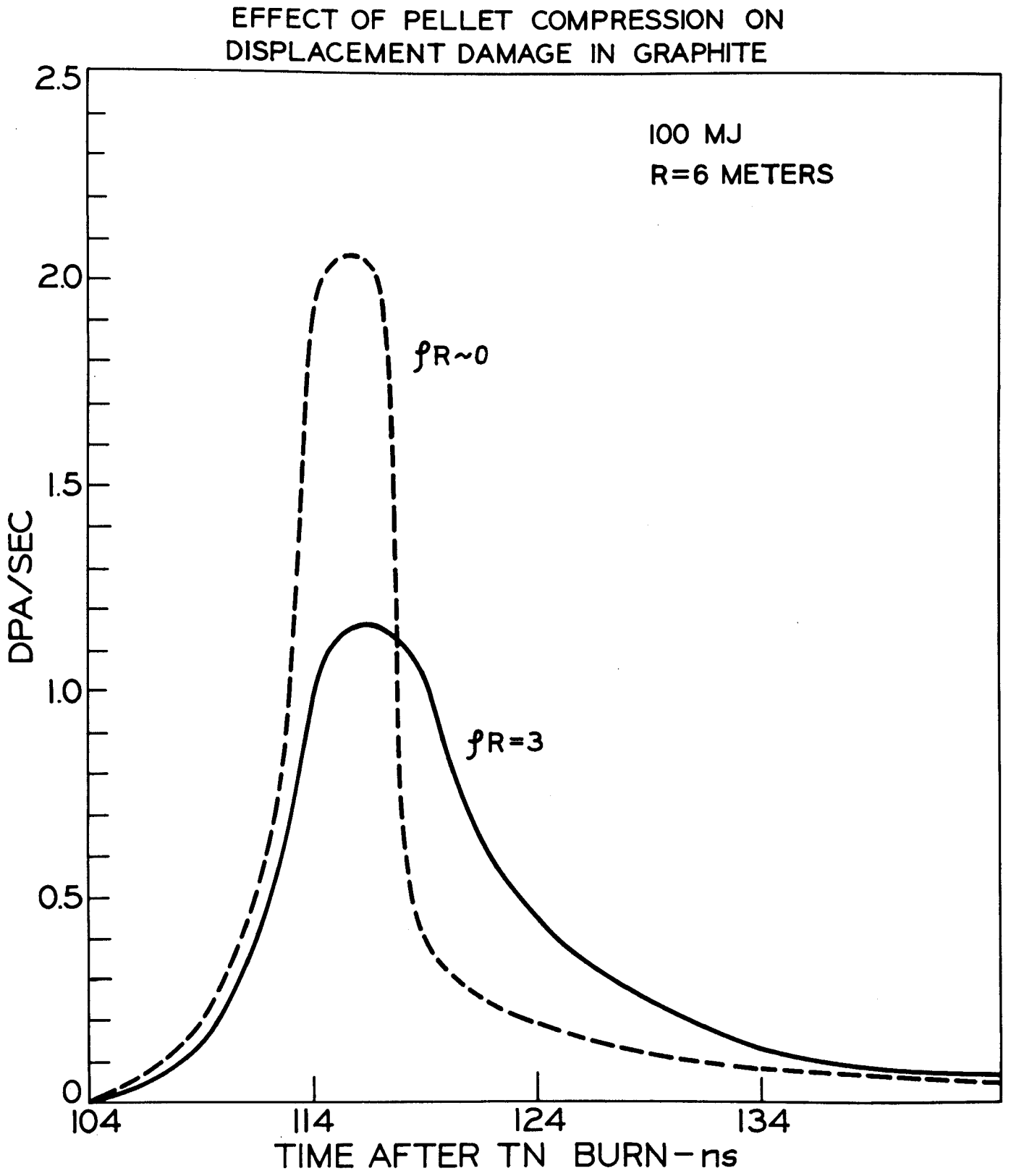
EFFECT OF PELLET COMPRESSION ON
DISPLACEMENT DAMAGE IN GRAPHITE
100 MJ
R=6 METERS
ρR~0
ρR=3
DPA/SEC
2.5
2.0
1.5
1.0
0.5
0
104
114
124
134
TIME AFTER TN BURN – ns

liquid Li layer similar to that used in the Hylife Concept [12]. Their results are summarized in Figure (5) where the fraction of dpa damage that is produced is plotted versus the dpa rate. The main point is that half of the damage in either case is produced at dpa rates of 0.1 sec^{-1} and above, 90% is produced above 0.001 sec^{-1} for the liquid Li case or 0.01 sec^{-1} for the bare pellet cases, and 30% is produced between 1 and 3 dpa sec^{-1} for the bare pellet cases. Hence it is not a single damage rate but a range of rates which one needs to be concerned with.

4.2 Ion Damage

4.2.1 Displacements for Ions of Z < 2

Hunter and Kulcinski (HK) [13] developed models for calculating the time and space dependent damage in ICF conditions. The mean ion energy was first calculated as a function of position, and then appropriate displacement cross-sections were used. A Lindhard (LSS) model [14] based on Thomas-Fermi potential was used in their calculations. The energy partition model derived by Robinson [15] was used to calculate the part of the ion energy causing damage. This was given by

$$T_{damage} = \frac{T}{g(\varepsilon)} \tag{1}$$

where

$$g(\varepsilon) = 1+k\varepsilon+0.40244k\varepsilon^{3/4}+3.4008k\varepsilon^{1/6} \tag{2}$$

k = LSS stopping parameter, which is for PKA's

$$k = 0.1337\ Z^{2/3}/A^{1/2}\ , \tag{3}$$

$$\varepsilon = \frac{T}{E_L} = \text{Lindhard reduced energy,} \tag{4}$$

and

$$E_L = 0.08693Z^{7/3} \tag{5}$$

Figure 5

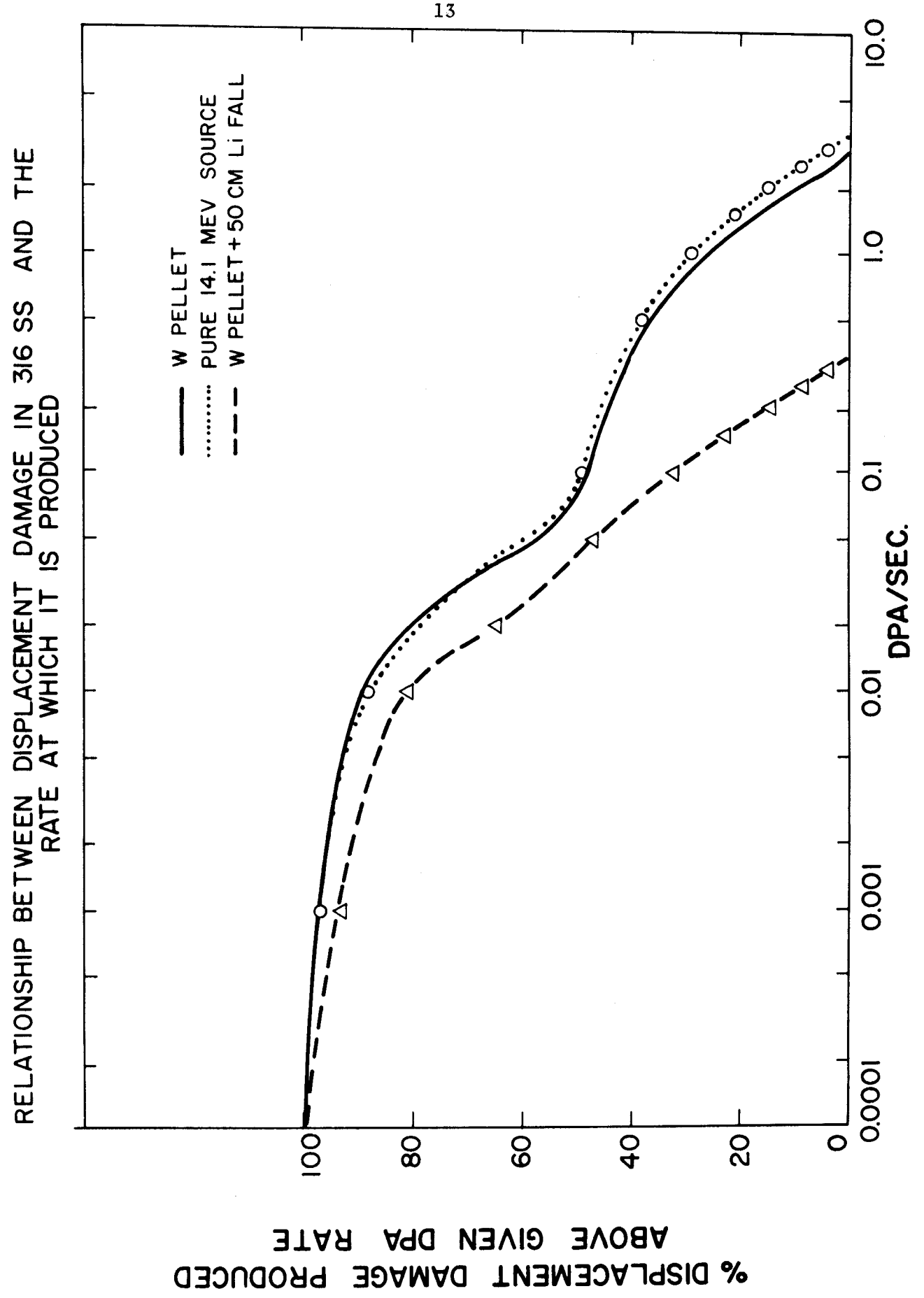
RELATIONSHIP BETWEEN DISPLACEMENT DAMAGE IN 316 SS AND THE RATE AT WHICH IT IS PRODUCED
W PELLET
PURE 14.1 MEV SOURCE
W PELLET + 50 CM Li FALL
% DISPLACEMENT DAMAGE PRODUCED ABOVE GIVEN DPA RATE
100
80
60
40
20
0
0.0001
0.001
0.01
0.1
1.0
10.0
DPA/SEC.

The displacement cross-section was calculated using the secondary displacement model of Doran [16], and was expressed as

$$\sigma_d(E) = \frac{B\gamma^2}{E} \int_{E_d}^{2E_d} \frac{dT}{T^2} + \int_{2E_d}^{T_{max}} \frac{0.8T}{3E_d} \frac{dT}{g(T)} \qquad (6)$$

where B is a constant, γ is the effective charge, E_d is the displacement energy and

$$T_{max} = \frac{4m_1m_2}{(m_1+m_2)^2} E \quad . \qquad (7)$$

HK proceeded to evaluate the local displacement rate for light ions as follows:

$$\dot{D}(x,t) = f(t)\sigma_d\{E(x,E^*)\} \qquad (8)$$

where $\dot{D}(x,t)$ is the spatial and time-dependent light ion displacement rate, $f(t)$ is the instantaneous flux of ions of energy E^* at the exposed surface and $E(x,E^*)$ is the energy of an ion of incident energy E^* at position x.

4.2.2 Displacements for Ions of Z > 2

The effects of scattering and straggling are more pronounced for heavy ions, and therefore ion implantation codes were used by HK [13] in order to calculate the displacement damage. The displacement damage rate at any position was simply calculated as:

$$\dot{D}(x,t) = f(t)\sigma(E^*,x) \quad . \qquad (9)$$

The damage cross-section, σ, was determined by performing a single set of ion implantation calculations using the Brice codes RASE4 [17] and DAMG2 [18] at selected ion energies covering all potential spectra of interest. The results were then parametrized by determining a numerical fitting function which is described in more detail elsewhere [13].

3.2.3 Application to Specific Pulsed Fusion Spectra

The damage rates experienced by an unprotected first wall can be illustrated by investigating the response to a single laser fusion pellet spectrum. We are forced to use such an approach because; 1) there are no targets which have actually achieved breakeven conditions, and 2) because the much higher yield pellets which are anticipated to work are classified. Therefore we will use a sprectum which might have all of the components or reasonable representations to make our points. Such a sprectum is listed in Table 3 for a 100 MJ yield [19].

TABLE 3

REFERENCE SPECTRA AND ENERGIES FOR 100 MJ PELLET

	Energy (MJ)	Spectra
Laser	0.2	10.6 μ
X-ray	2.0	1.0 keV - BB
D	4.6	160 keV - M
T	6.9	240 keV - M
He (slow)	1.2	320 keV - M
He (fast)	5.4	2 ± .5 MeV - G
Silicon	2.7	800 keV - M
Neutron	77.0	14 ± 1 MeV - G

BB = blackbody; M = Maxwellian; G = Gaussian

The various components strike the wall at different times and for different pulse durations because of the spread in their energies. The X-rays strike the wall for essentially the compression and disassembly

time ($10^{-9} - 10^{-8}$ seconds). It takes R_w/c for the first X-rays to reach the wall, where R_w is the ICF reactor cavity radius and c is the speed of light. This is typically 20 ns. The time over which the neutrons strike the first wall is determined by the downscattering of 14.1 Mev neutrons in the dense plasma. An example of the chronology of particle arrival for the above spectra is shown in Fig. (6) [19] with and without gas in the cavity chambers.

The displacement rate from each component at the surface of a stainless steel first wall is shown in Fig. (7), and at 0.1 micron from the surface in Fig. (8). All the ionic debris interact with higher displacement cross-sections as their energies are reduced near the end-of-range.

4.2.4 Effect of Buffer Gases

Survival of first walls and other components in Inertial Confinement Fusion systems may require the use of protective systems to reduce the energy flux of ions and photons. Numerous methods have been proposed which include magnetic fields [20], liquid walls [21], flexible carbon cloth [22] and gas layers [23] and these are reviewed elsewhere [19]. This section is based on the work by HK [24] and McCarville, Hassanein, and Kulcinski (MHK) [25] who investigated the effects of buffer gas.

To account for the transport of ions through a buffer gas layer, separate treatments were used for heavy ions (or low energy light ions) and light ions of higher energy. The former was based on a diffusion approximation to the transport of ions, while the latter was based on the stopping power functions.

The instantaneous flux of particles passing through any position was determined as the product of the concentration (C) and the normal velocity (v) as

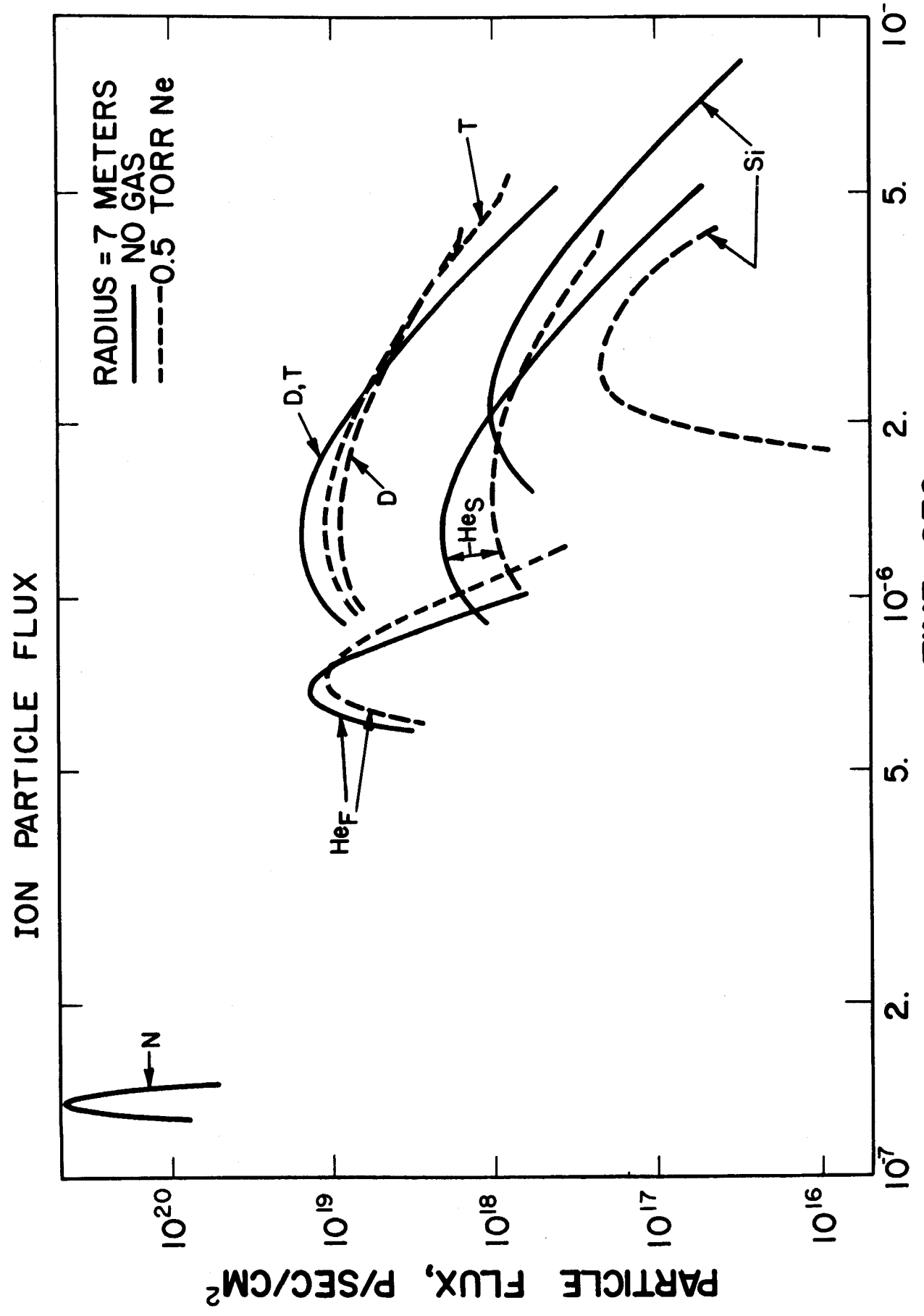
ION PARTICLE FLUX
RADIUS = 7 METERS
NO GAS
0.5 TORR Ne
N
D,T
D
T
He_F
He_S
Si
PARTICLE FLUX, P/SEC/CM²
TIME, SEC
10²⁰
10¹⁹
10¹⁸
10¹⁷
10¹⁶
10⁻⁷
2.
5.
10⁻⁶
2.
5.
10⁻⁵

Figure 6

Figure 7

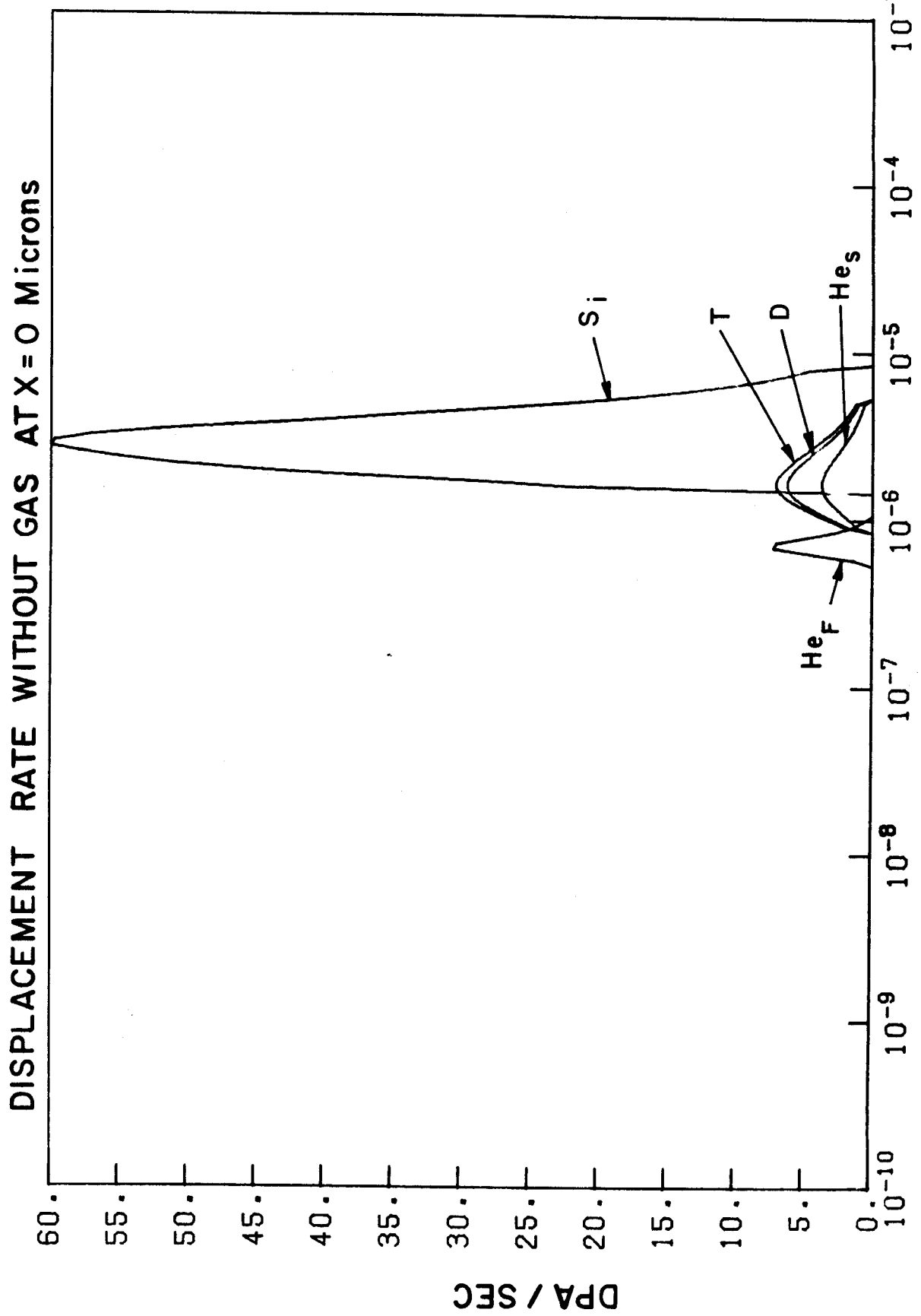
DISPLACEMENT RATE WITHOUT GAS AT X = 0 Microns
DPA / SEC
60.
55.
50.
45.
40.
35.
30.
25.
20.
15.
10.
5.
0.
10^{-10}
10^{-9}
10^{-8}
10^{-7}
10^{-6}
10^{-5}
10^{-4}
10^{-3}
TIME AFTER X-RAY ARRIVAL, sec
Si
T
D
He_S
He_F

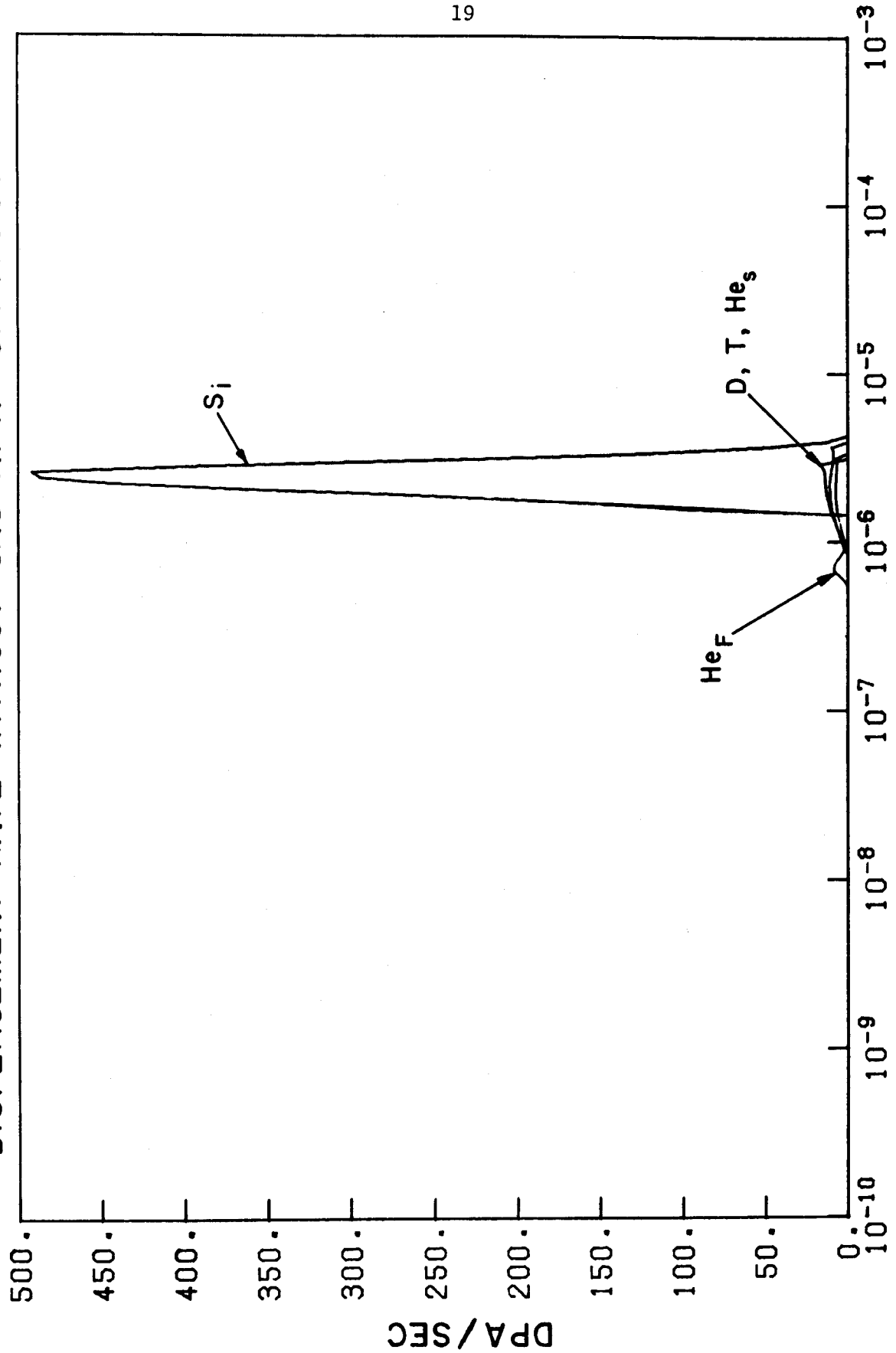
DISPLACEMENT RATE WITHOUT GAS AT X =0.4 Microns
DPA/SEC
500.
450.
400.
350.
300.
250.
200.
150.
100.
50.
0.
10^{-10}
10^{-9}
10^{-8}
10^{-7}
10^{-6}
10^{-5}
10^{-4}
10^{-3}
TIME AFTER X-RAY ARRIVAL, sec
S_i
D, T, He_s
He_F

Figure 8

$$F(t,x) = C(t,x)v(t,x) \qquad (10)$$

The concentration was determined by considering the diffusion of monoenergetic ions in the center-of-mass, and the motion of the center-of-mass. The flux of ions at a position x due to an incident spectrum was evaluated by summing up the contributions of each ion at a specific time, i.e., integrating equation (10) over the energy spectrum.

The flux and arrival times associated with each species for the reference pellet spectra of Table 3 are depicted in Fig. (6) with and without 0.5 torr of Ne. Each pulse is lowered in peak amplitude and spread in time by the gas. The silicon component, however, is reduced in magnitude and shortened in time since the ions which would normally arrive at late times do not reach the exposed surface. The deuterium and tritium flux were originally the same without gas protection; yet, because of their different stopping powers in neon, the deuterium spectrum was much more degraded than that of tritium.

The displacement rate at the front surface of a steel first wall is reduced by 30% when 0.5 torr of Ne gas is introduced (Fig. (9)). This is primarily due to the fact that, although the energy and number of silicon ions are reduced, the lower ion energies are characterized by significantly higher effective displacement cross sections. At greater depths, such as at 1 micron in Fig. (10) the significant reduction of damage is apparent since the silicon ions are less energetic after passing through the gas and do not penetrate to this position. The displacement production by the neutrons is essentially uniform throughout the material and at depths greater than 10 microns, the neutrons are the only reaction products capable of producing damage. The most revealing comparison of the displacement

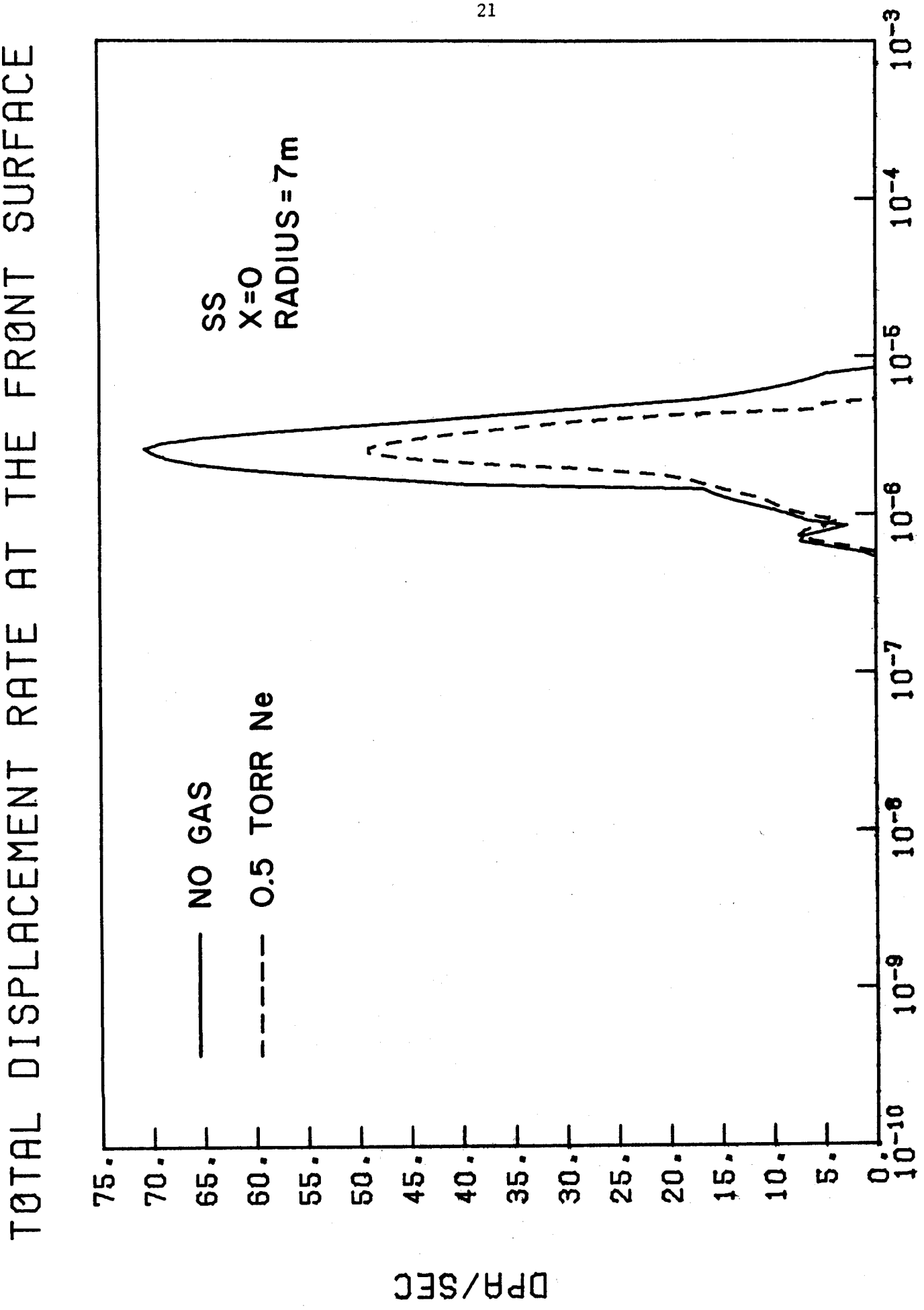
TOTAL DISPLACEMENT RATE AT THE FRONT SURFACE
SS
X=0
RADIUS=7m
NO GAS
0.5 TORR Ne
DPA/SEC
TIME AFTER X-RAY ARRIVAL, SEC
75.
70.
65.
60.
55.
50.
45.
40.
35.
30.
25.
20.
15.
10.
5.
0.
10^{-10}
10^{-9}
10^{-8}
10^{-7}
10^{-6}
10^{-5}
10^{-4}
10^{-3}

Figure 9

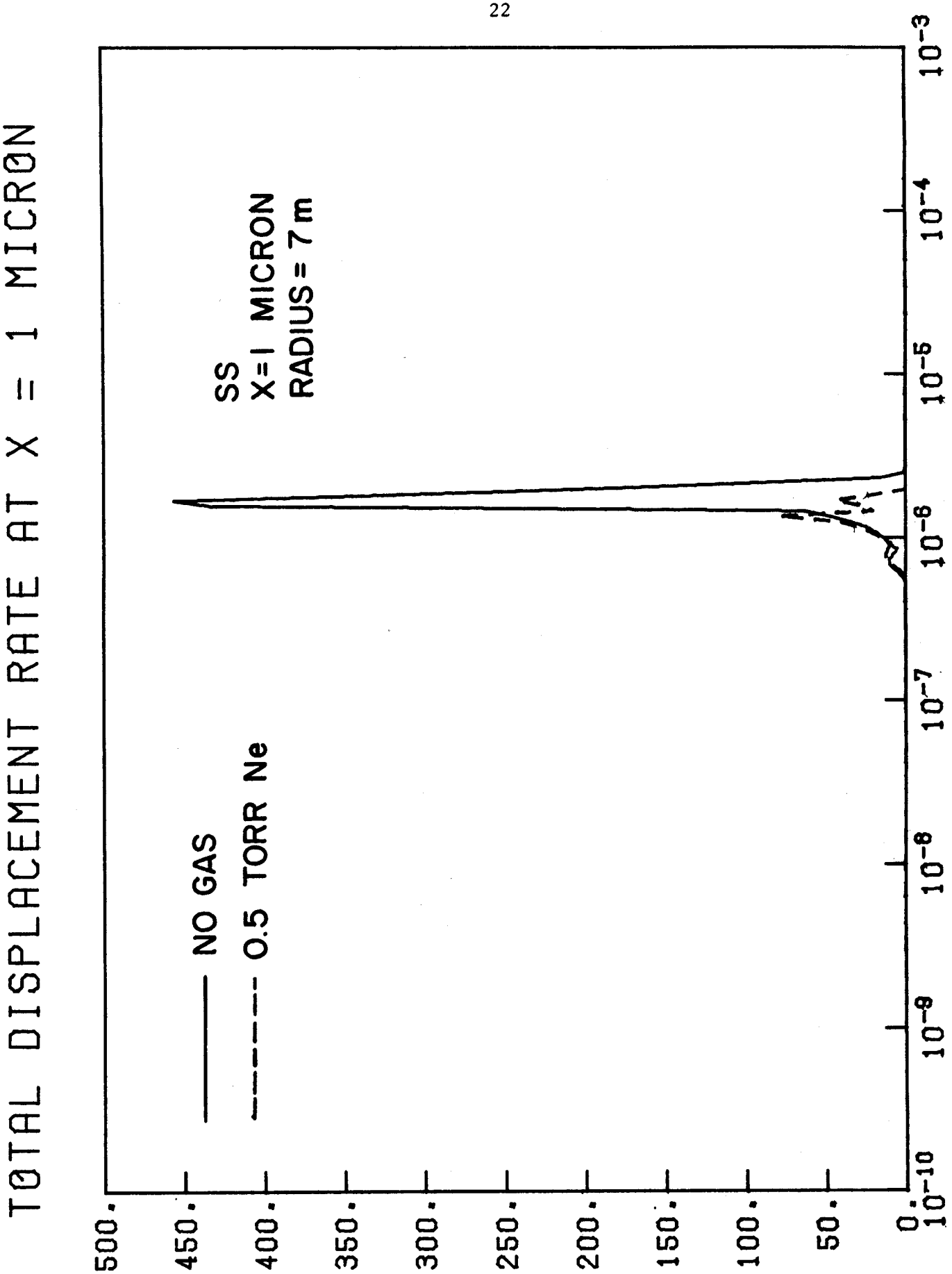
TOTAL DISPLACEMENT RATE AT X = 1 MICRON
SS
X=1 MICRON
RADIUS = 7 m
NO GAS
0.5 TORR Ne
DPA/SEC
500.
450.
400.
350.
300.
250.
200.
150.
100.
50.
0.
10^{-10}
10^{-9}
10^{-8}
10^{-7}
10^{-6}
10^{-5}
10^{-4}
10^{-3}
TIME AFTER X-RAY ARRIVAL, SEC

Figure 10

production is given in Fig. (11) which shows the composite spatial distribution of all the ion components after the deposition pulse. The peak damage is reduced from 1.2×10^{-3} dpa per pulse to about 3.6×10^{-4} dpa per pulse by the addition of the gas.

5. THERMAL RESPONSE

5.1 Energy Deposition

It is necessary to treat the pellet debris in three broad categories; photons, ions, and neutrons. The primary interactions of photons with materials that need to be analyzed are the photoelectric effect, coherent scattering and incoherent scattering. Hovingh [26] has proposed a simple relation based on the propagation of electromagnetic radiation to describe the absorption and reflection of laser light at the surface of the first wall. HK [13] and MHK [25] have used the Briggs Library of X-ray absorption cross sections to handle a spectrum of X-ray energies transported through various gaseous media and absorbed in the first wall.

The deposition of energy by the various ionic components has been described previously. The main problem here is to calculate the spatial and time dependent variations for input into the heat conduction equations. The use of uniform deposition profiles or instantaneous deposition rates can sometimes give misleading results.

The local heating due to neutrons can be determined from the neutron flux and knowledge of an energy dependent kerma* factor. Recent work by Abdou [28] has determined such kerma factors for most potential fusion materials. Determination of the neutron and gamma flux in the first wall multiplied by the kerma factor will yield the total heating. Calculations of this kind have been performed with the ANISN [29] code for simple

---

*Kerma = Kinetic Energy Released in Materials.

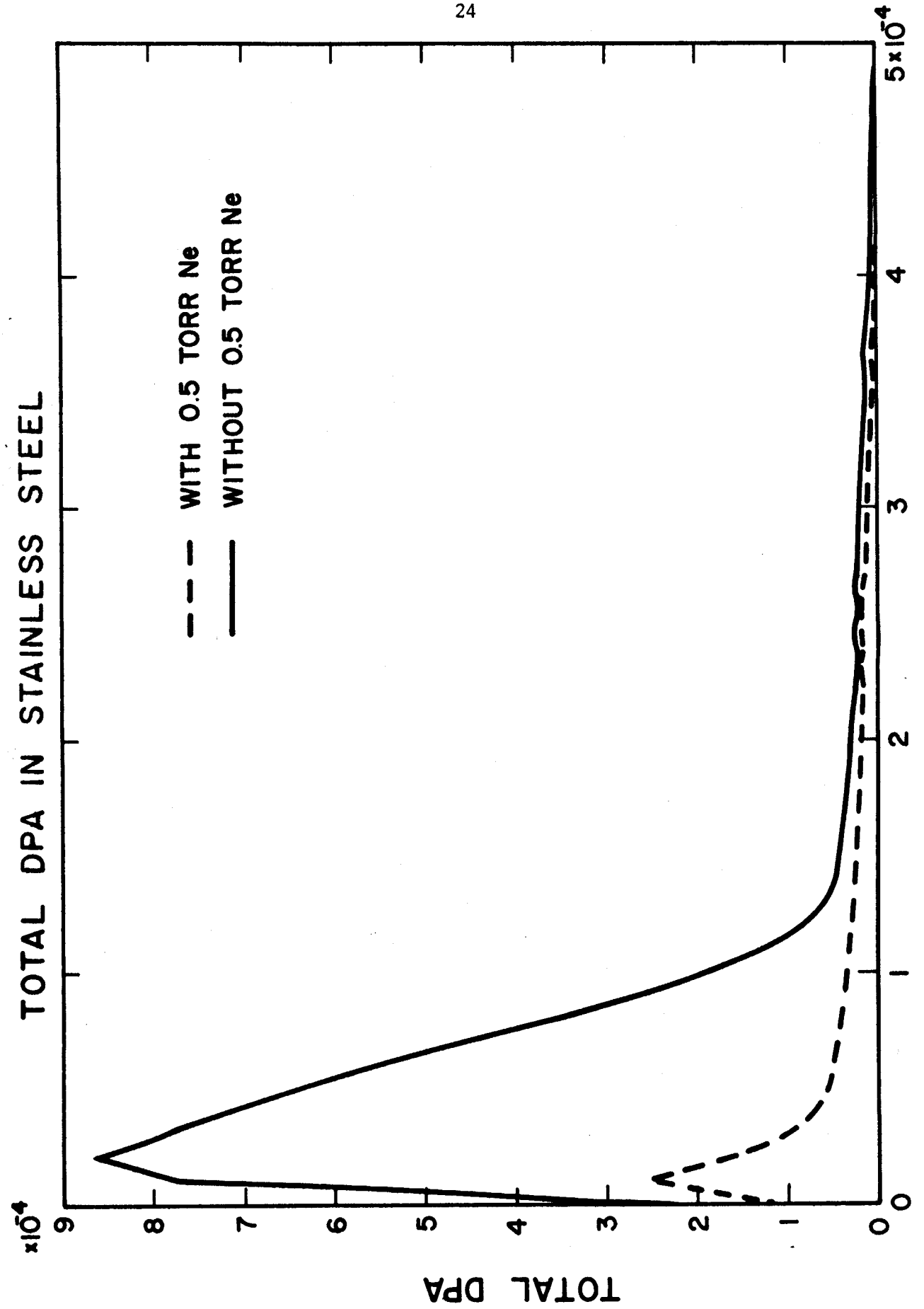
TOTAL DPA IN STAINLESS STEEL
WITH 0.5 TORR Ne
WITHOUT 0.5 TORR Ne
TOTAL DPA
DISTANCE INTO FIRST WALL, cm
x10⁻⁴
5x10⁻⁴
0
1
2
3
4
5
6
7
8
9

Figure 11

spherical blankets and the neutronic heat deposited was found to represent an insignificant perturbation to the total pulse heating (i.e., <5°K).

5.2 Temperature Response

The temperature excursion from neutron irradiation has been found to be small in pulsed fusion environments [13], and therefore will not be considered here. Hovingh [26] and HK [13] have developed models for the photon and ion temperature response. The photon energy deposition was assumed by HK to be given by

$$q(t,x) = \sum_{n=0}^{M-1} \delta(t-n\omega)\mu F_o e^{-\mu x} \tag{11}$$

where $\delta(t-n\omega)$ is the unit delta function, μ is the attenuation coefficient, F_o is the incident intensity (energy/unit area), M is the total number of pulses and ω is the time between pulses. By separation of variables and transform methods, the heat conduction equation was solved for a finite slab to yield the time and spatial temperature distribution due to photons.

For ions, a model was developed to calculate the temperature response from energy deposition profiles. An analysis of the temperature distribution at any position within the first wall can be described as follows.

$$T(x,t) = \int_{t'} \int_{x'} \frac{f(t')}{\rho C_o} g(x')G(x,t,x',t')dx'dt' \tag{12}$$

where f(t') is the function that describes the arrival of various photon and ionic species,

g(x') is the energy deposition function for the various forms of radiation,

ρ is the material density,

C_o is the heat capacity

G(x,t,x',t') is the Green's function for a semi-infinite slab [30].

The solution of this equation is contained in the computer program, T*DAMEN [31].

The temperature increase due to each of the components from a multi-specie pellet design is given in Fig. (12). The data is for stainless steel at 7 meters from the pellet. The very high temperatures generated at 7 meters from a 100 MJ explosion are indicative of the magnitude of the problem faced by reactor designers.

4.3 Stress Response

The stresses will be produced in irradiated first walls by four different mechanisms:

1. Momentum of the pellet debris, P_m.
2. Shock waves generated by material ablated off the first wall, P_A.
3. The thermoelastic response to deposited energy, P_t.
4. Shock waves generated by chamber gases when used for first wall protection, P_g.

The magnitude of the first effect can be estimated as follows [32]:

$$P_m = \frac{\sqrt{fYM}}{2\pi\sqrt{2}R_w^2\tau} \tag{13}$$

where M is the mass of the pellet,

τ is the duration of the pulse to the wall and f is the fraction of yield in ions.

For typical high pellet designs, f = 0.2, Y = 500 MJ, M = 1 g and $\tau = 10^{-5}$ sec, one finds that

$$P_m \equiv \frac{3.5}{R_w^2(m)} \text{ MPa} \tag{14}$$

Thus, a 7 meter radius chamber wall would experience on the order of 0.7 atmosphere pressure from the momentum of the pellet debris.

Bohachevsky [32] estimated the wall pressure due to wall material ablation to be,

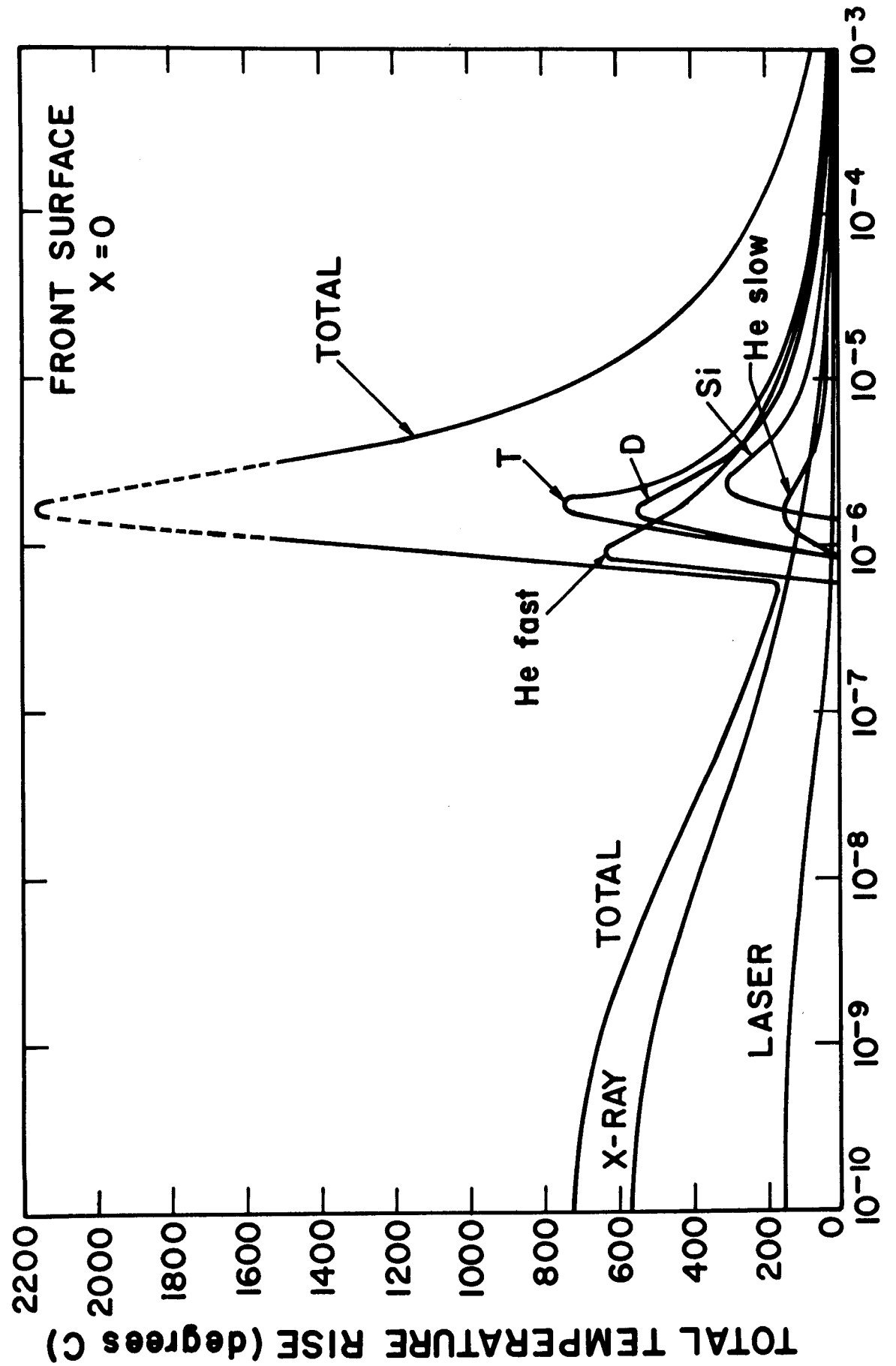

Figure 12 - Temperature Increases in Stainless Steel Due to the Pellet Spectra of Table 1 (R_W = 7m).

$$P_A = \frac{\eta f_x Y}{4\pi R_w^2 \tau \sqrt{2H}} \tag{15}$$

where η is the effectiveness coefficient to account for the fact that not all the ablated material moves with the maximum velocity into the chamber, H is the heat of vaporization and f_x is the fraction of energy in X-rays. For typical values of X-ray deposition in steel one finds that using $\eta = 0.15$, $f_x = 0.02$, Y = 500 MJ, H $\simeq$ 6.3 kJ/g and τ = 100 ns, gives

$$P_A \simeq \frac{333}{R_w^2(m)} \text{ MPa} \quad . \tag{16}$$

For a wall radius of 7 meters and Bohachevsky's assumptions on the mass of the metal ablated, the recoil shock wave would be equal to 7 MPa ($\sim$70 atmospheres).

One method of calculating the thermoelastic stress response was evaluated by HK [33], starting from the defining equation for stress wave propagation:

$$\frac{\partial^2 \sigma}{\partial x^2} - \frac{1}{c^2} \frac{\partial^2 \sigma}{\partial t^2} = A \frac{\partial^2 T}{\partial t^2} \tag{17}$$

where $c = [E/\rho(1-\nu)]/(1+\nu)(1-2\nu)$ is the longitudinal wave velocity, σ is the stress, t is the time, T is the temperature and

$$A = \rho\alpha \frac{(1+\nu)}{(1-\nu)} \tag{18}$$

where ρ is the density, α is the linear thermal expansion coefficient and ν is the Poisson's ratio. Coupling the stress wave propagation equation with the constitutive relation for uniaxial strain, and the heat equation, HK [33] showed that the thermal stress wave amplitude approaches zero as the pulse length gets longer than $\sim 3 \times 10^{-8}$ seconds. The amplitude is reduced for times longer than this because the stress propagates away faster than it is created.

The last of the four stress mechanisms can be estimated by the theory of Taylor and Sedov [34] when the chamber gas density exceeds 10^{-7} g/cm^3 (i.e.,

0.3 torr of Xe). The following expression is used [32]

$$P_g = \frac{K(\gamma) f_i Y}{R_w^3} \tag{19}$$

where $K(\gamma)$ is a function of γ, the ratio of specific heats of the gas, and where $\gamma = 1.4$, $K = 2.39$. f_i is the fraction of yield in ions. For $f_i = 0.2$, $Y = 500$ MJ, the above equation predicts

$$P_g \simeq \frac{230}{R_w^3(m)} \text{ MPa} \tag{20}$$

Hence, for a 7 meter radius chamber the shock overpressure is $\sim$7 atmospheres.

It is generally felt that the surface area of unprotected metal walls will have to be extremely large to withstand the thermal and pressure loading from economically attractive pellets. The inclusion of sputtering and chemical interactions will only make the situation worse. Hence, it is easy to understand the motivation behind various cavity protection schemes and much more work needs to be done to understand how those schemes affect the damage production rate.

6. EFFECT OF PULSED IRRADIATION ON THE MICROSTRUCTURE

Considerable interest in the effects of pulsed irradiation on the microstructure development of metals has emerged only during the past five years. In 1975, the first theoretical and experimental papers began to appear on investigations of void swelling during pulsed irradiation. More recently, other aspects of the microstructure have been considered. In this section, we will present a summary of the experimental work, and the current theoretical understanding of microstructural evolution during pulsed irradiation.

6.1 Experimental Evidence

Few experiments were performed to date on the effects of pulsed irradiation on materials. The production of vacancies and voids by laser bombardment

was first reported by Metz and Smidt (MS) [35,36]. Laser irradiation was examined as a potentially useful technique for producing a large number of microscopy samples from a relatively thin sheet of test materials. Vacancy condensates were observed in a variety of materials but MS [36] concluded that quenching in the conventional sense cannot account for the high vacancy concentrations because they were two orders of magnitude higher than the 10^{-5} to 10^{-4} values commonly found at the melting point. They speculated that the vacancy generation mechanism was the nonconservative motion of jogs on screw dislocations. The mechanism by which the voids are formed, however, was not immediately obvious.

Kressel and Brown [37] observed enhanced vacancy production in nickel shock loaded to pressures of 70 to 330 kbars. Dislocation densities of the order of $2x10^{10}$ cm/cm^3 were observed, although the vacancy concentration did not exceed $6x10^{-5}$. Shock waves were generated in the MS experiments by laser bombardment as a consequence of the rapid thermal expansion of the specimen's front face, but the peak stress was estimated to be only of the order of 10 kbars for the power density used in these experiments, far lower than in the Kressel and Brown experiment.

At the Naval Research Laboratory (NRL), experiments were conducted to study the methods used to obtain a uniform ion dose across the surface of the bombarded specimens. Specimens of >99.99% nickel were examined by transmission electron microscopy following bombardment with 2.8 MeV $^{58}Ni^+$ ions to a fluence of $5.68x10^{15}$ ions/cm^2 at temperatures between 365°C and 775°C [38]. Two methods of bombardment were used to produce these specimens. One set of irradiations was performed with a focused ion beam scanned over the specimen surface in a raster pattern with a horizontal scan frequency of 10 kHz and a vertical scan frequency of 100 Hz. The other set of

irradiations was made with the central portion of a defocused ion beam which was held in one position over the specimen.

The temperature dependence of the damage produced by these two modes of bombardments was very different as shown in Figure (13), which is a plot of the mean void diameter as a function of the irradiation temperature. The mean diameter of the voids produced by the defocused beam irradiations increased with increasing bombardment temperature which is the typical dependence normally observed in neutron-irradiated metals. The mean diameter of the voids in the scanned-beam specimens, on the other hand, decreased with increasing bombardment temperature. Both methods of bombardment produced the highest swelling near 600°C, and all of the data points were found to fall near the same swelling curve, although the swelling of the defocused beam specimen at 620°C was significantly higher than that observed in the scanned beam specimen at the same temperature.

The square cross-section beam was assumed to have uniform intensity and was scanned in a raster pattern. This produced an ion flux at the center of the specimen as shown in Fig. (14): A series of 50 pulses, 2.5×10^{-5} sec long separated by 2.5×10^{-3} sec was used. The point defect production rate during each pulse of ions was chosen to be 0.32 dpa/sec to give time-averaged production rates of 8×10^{-2} dpa/sec.

Taylor, Potter and Wiedersich [39,40] conducted experiments to study the effects of pulsed irradiation on void microstructures in nickel. The time structure of the pulses and the irradiation conditions corresponded to irradiation pulses long compared with the interstitial lifetime and shorter than the vacancy lifetime.

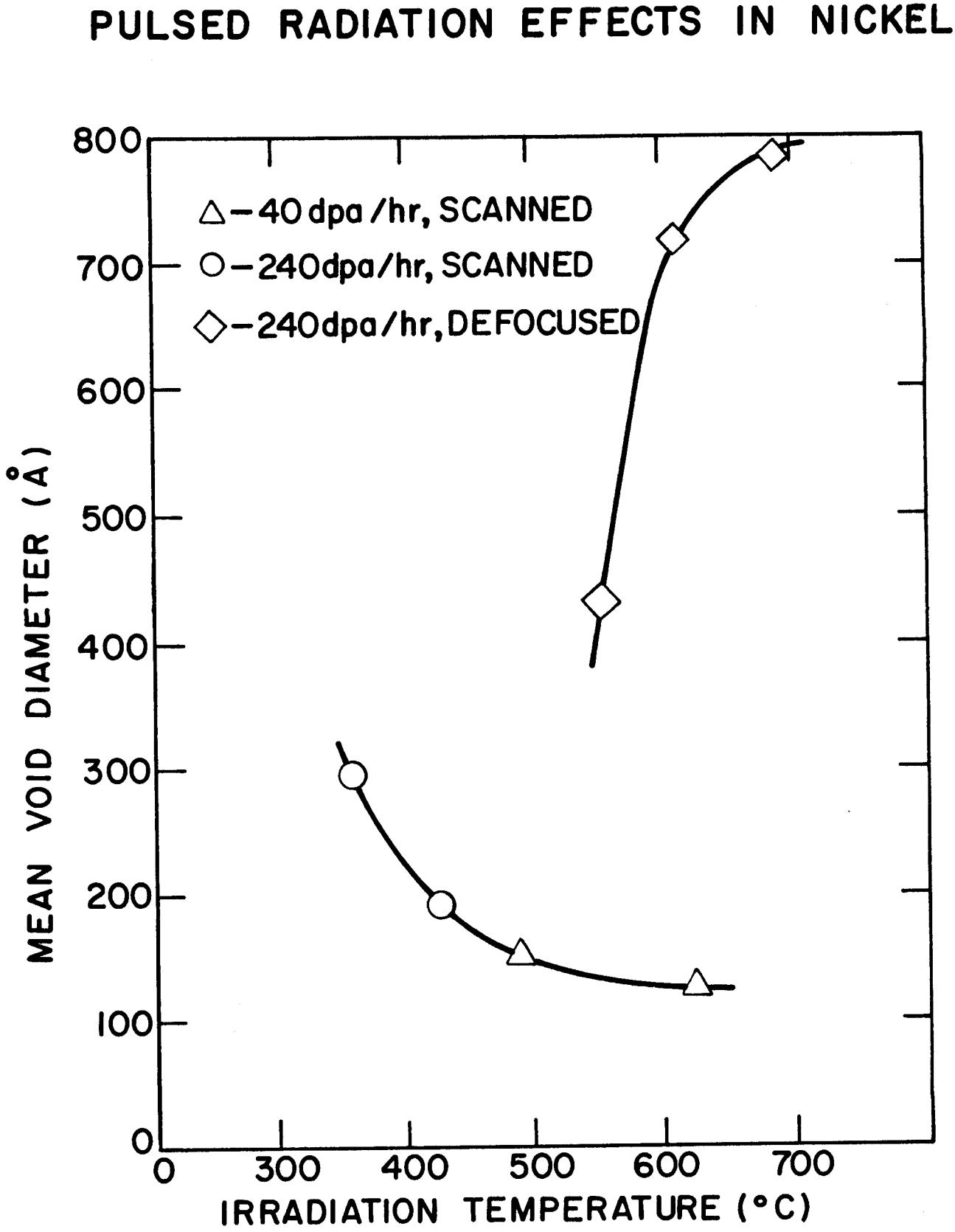

Figure 13 - Experimental Results of Ni Ion Irradiated Ni for Steady Defocused and Scanned Beams.

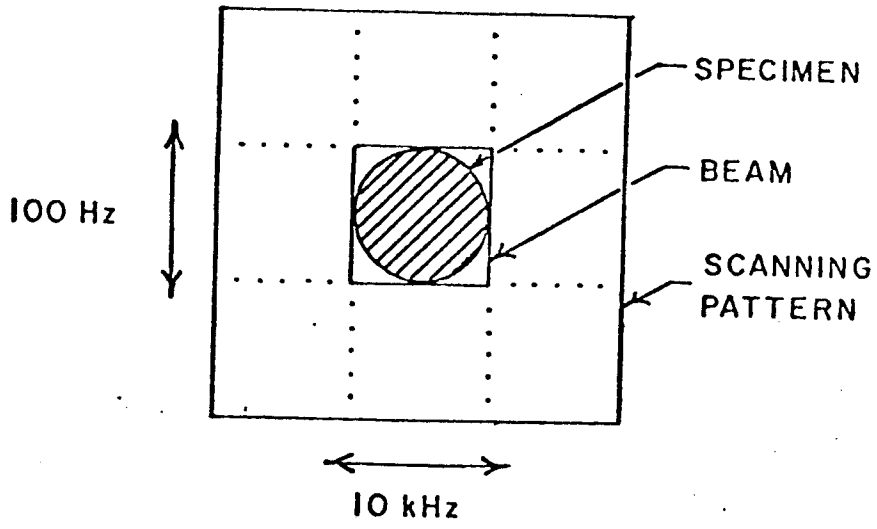

(a) IDEALIZED SCANNING PATTERN

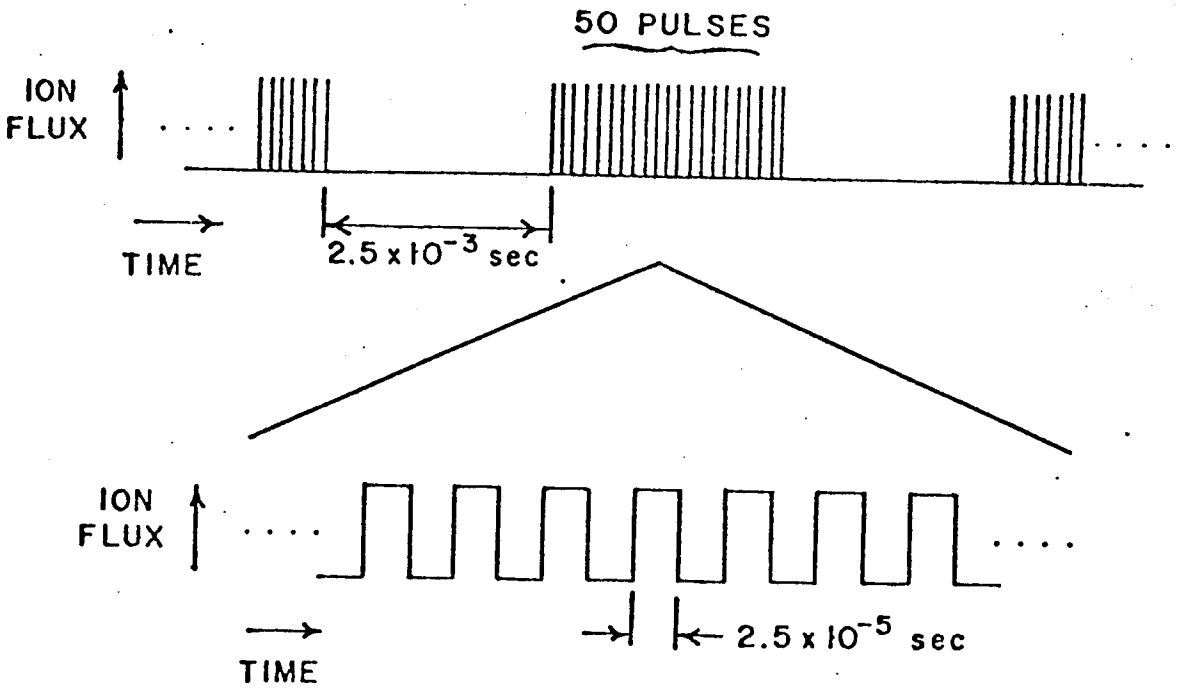

(b) IDEALIZED ION FLUX

Figure 14

Two sets of experiments were conducted. One set was done at 600°C using equal on-off pulses of 13 ms duration. These samples are compared with those undergoing steady or d.c. beam irradiation to the same dose level of ∿5 dpa. The results show variation in both void number density and void size, suggesting both void nucleation and growth are affected by pulsed beam irradiation. The second set was pre-voided by irradiation at 600°C, then subjected to pulsed-beam irradiation at 500°C. This latter approach allowed some insight into pulsed-beam effects on void growth alone.

The results of the pulsed-ion irradiation performed at 600°C are presented in Table 4 and compared with previous results of Ryan [41] for the same material irradiated with a d.c. beam. The doses listed are those at the completion of irradiation and the dose rates are the mean values during irradiation, i.e., dose per cycle divided by the cycle period. The samples should be compared in two sets, those irradiated to 2.3 and 2.6 dpa and those irradiated to 6.2 and 7.7 dpa. In both cases the pulsed-beam had an equal on-off time of 13 ms. However, in the first case the pulsed-beam-on intensity was twice that of the constant intensity beam, giving the same time averaged intensity. In the second case, the pulsed-beam-on intensity was the same as the constant beam intensity, giving the mean pulsed-beam intensity half the value of the constant intensity. This factor of two in the beam intensity or in displacement rate produced no significant difference in results.

Both the lower and higher dose results showed the same effects when the pulsed-beam mode of irradiation is compared with the d.c. mode. The void volume fraction is essentially unchanged, but the void microstructure is significantly altered. The void number density in the pulsed mode is an order of magnitude lower than in the d.c. mode of irradiation. The void size is nearly doubled for the pulsed-beam as compared with the constant

TABLE 4

Results of pulsed-beam and constant-beam irradiation of nickel at 600°C

Time Structure of Beam	Mean Void Diameter nm.	Void Number Density $10^{21}m^{-3}$	Void Volume $\Delta V/V\%$	Dislocation Density, m^{-2}	Mean Dose Rate, dpa/s	Dose, dpa
Constant Intensity	26	1.6	1.8	$4.8x10^{9}$	$6x10^{-3}$	2.3
13 ms on-13 ms off	48	.26	1.5	$7.0x10^{9}$	$6x10^{-3}$	2.6
Constant Intensity	35	1.7	2.4	$8.3x10^{9}$	$6x10^{-3}$	6.2
13 ms on-13 ms off	60	.18	2.4	$1.8x10^{10}$	$4.x10^{-3}$	7.7

TABLE 5

Results from samples pre-voided at 600°C to ∿5 dpa and subsequently irradiated to ∿5 dpa at 500°C using various pulsed-beam structures listed below.

Time Structure of Beam	Mean Void Diameter nm.	Void Number Density $10^{21}m^{-3}$	Void Volume $\Delta V/V\%$	Mean Dose Rate dpa/s	600°C Dose dpa	500°C Dose dpa
as pre-voided control	13	6.3	.84	$2.4x10^{-3}$	3.7	
constant 5 dpa	20	3.3	1.4	10^{-2}	4.9	5.2
3.35 sec on-0.4 sec off	20	3.2	1.5	$4x10^{3}$	5.0	5.1
1.7 sec on-6.8 sec off	15	5.4	1.1	$2.0x10^{-3}$	5.0	5.4
6.75 sec on-6.75 sec off	24	2.3	.017	$7.0x10^{-3}$	5.1	4.5

beam. Taylor et al. suggested that pulsed-beam irradiation reduces the void nucleation rate and enhances the void growth rate.

Though the above experiment indicated an effect of beam pulsing on void microstructure, it was not clear whether the increased growth rate of voids was due to beam pulsing or to the decreased number of voids available to accept the irradiation produced point defects. In an attempt to investigate the influence of various pulse structures on void growth, a void structure was developed in several He pre-injected samples at 600°C using a dose rate of 3×10^{-3} dpa/sec and a dose level of $\sim$5 dpa. These samples were given subsequent $\sim$5 dpa pulsed irradiations at 500°C using an instantaneous dose rate of 9×10^{-3} dpa/sec. Details of the pulse and void structures are given in Table 5. The pulse times were increased to counterbalance the increase in vacancy lifetime at 500°C as compared to that of 600°C. It should be noted that the "pre-voided" sample showed swelling which was only about half that expected from data by Ryan [41]. The reason for this was not known but it may reflect a slightly lower irradiation temperature in this experiment as compared to Ryan's.

Continued irradiation at 500°C using a constant intensity beam produced further swelling, an increase in void size, and a decrease in void number density, indicating that a significant fraction of the voids introduced at the higher temperatures are stable under further irradiation. The effects of the pulsed beam structures were as follows. The long on-short off beam structure produced the same swelling as the constant beam and the void microstructures were equivalent. The short on-long off beam structure produced very little additional swelling. The sample shows a number density close to the pre-voided value and its mean void size of 15 nm is only slightly larger than the value of 13 nm for the pre-voided sample. The void size is less than the

20 nm size observed after constant beam irradiation. Thus, it appears that the short on-long off pulsed-beam results in a reduced void growth rate. The equal on-off pulsed irradiation produced the greatest increase in void swelling. The void number density is close to that for the constant beam situation and the void size of 24 nm for the equal on-off pulsed condition as compared to the 20 nm size for the constant beam condition suggests that the void growth rate is increased for this pulsed-beam structure.

The results reported in this note suggest that pulsed beam irradiations reduce the void nucleation rate and alter the void growth rate as compared to constant irradiation conditions. Short on-long off pulses showed the lowest void growth rates, long on-short off growth rates most closely reproduced constant beam growth rates, while the greatest increase in void sizes was observed for equal on-off times.

In another experimental study, a simple Fe-Ni-Cr alloy, of nominal composition 15 wt % Cr and 25 wt % Ni, was used by Powell and Odette [42] to study the effects of pulsed HVEM irradiation on the microstructure evolution. Electron irradiations were performed at 1 MeV in a JEOL JEM-1000 using a double tilting gonimeter heating stage. Pulsing of the electron beam was accomplished by deflection with two pairs of electrostatic deflector plates alternately charged and discharged with square wave voltage pulse generators. Rise and fall times of the voltage pulse were less than 1 msec and the positional stability of the electron beam was excellent.

An irradiation temperature of 600°C (including heating due to the electron beam) was used for all irradiations. Peak displacement rate for all pulsed and steady state irradiations was 1.3×10^{-3} dpa/sec. Pulse periods of 2.5 seconds to 60 seconds with 40 to 60% duty factors were employed in their investigation.

The dose dependence of swelling for steady state and pulsed conditions is shown in Figures (15) and (16). These data indicated that: 1) the swelling rate was lower under pulsed conditions compared to the steady state value, 2) the swelling rate decreased with decreasing duty factor (i.e., longer beam-off period), 3) the major effect of pulsing on swelling is a significant reduction in void size, 4) the void concentrations increase in the pulsed study compared to steady state irradiations.

In another recent experimental investigation, Kaletta [43] studied the microstructure of vanadium bombarded with 2 MeV helium ions under pulsed irradiation conditions typical of Tokamak reactors. The sub-surface damage in vanadium induced by helium ions of a mean range of 4.3 ± 0.14 μm was investigated. The samples were prepared from annealed 0.2 mm pure (99.94) vanadium foils and were electropolished prior to irradiation. The irradiation temperatures of 848°K and 948°K were chosen to be 50°K below and above the critical temperature of 898°K at which the coalescence of bubbles becomes the dominant growth mode in vanadium [44]. The analysis of the implanted samples were done by means of transmission electron microscopy (TEM) techniques at various sample depths corresponding to different ratios of helium to displacement damage. It was observed that pulsed irradiation resulted in a large increase in bubble diameters and a strong reduction in the concentration of bubbles. This effect was attributed to an altered microstructure during each shut-down cycle. The thermal generation of vacancies during the beam-off period was speculated to enhance the growth and mobility of small He-vacancy clusters. Vacancy absorption at the small He-vacancy clusters was postulated to reduce the strain fields and thereby enhance their mobility. In the high temperature case,

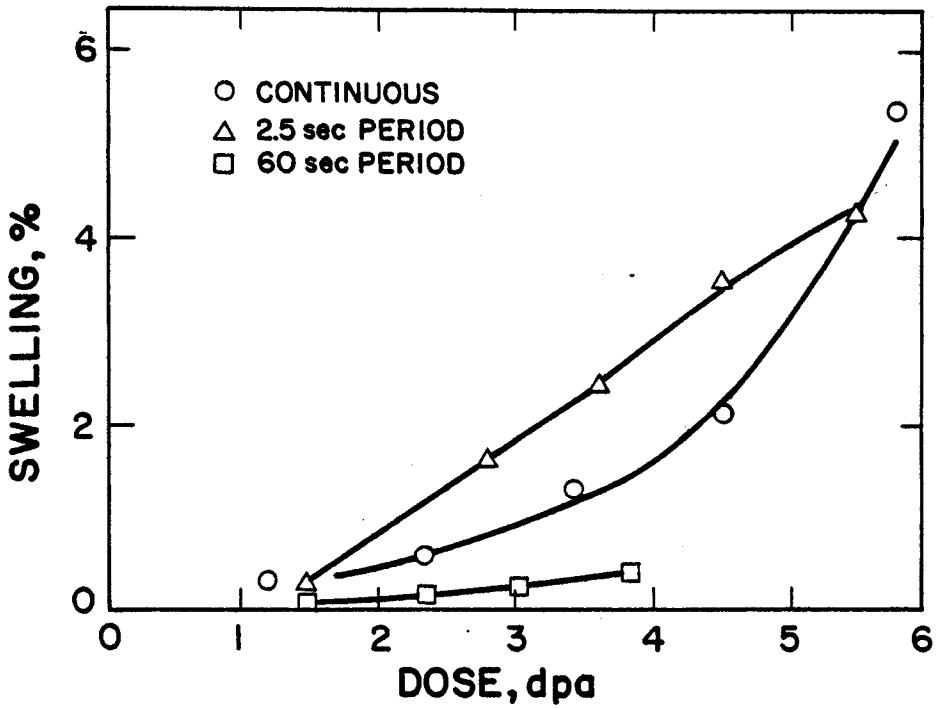

Figure 15 - Fluence dependence of swelling for the continuous irradiation, the shortest pulse period irradiation and the longest pulse period irradiation.

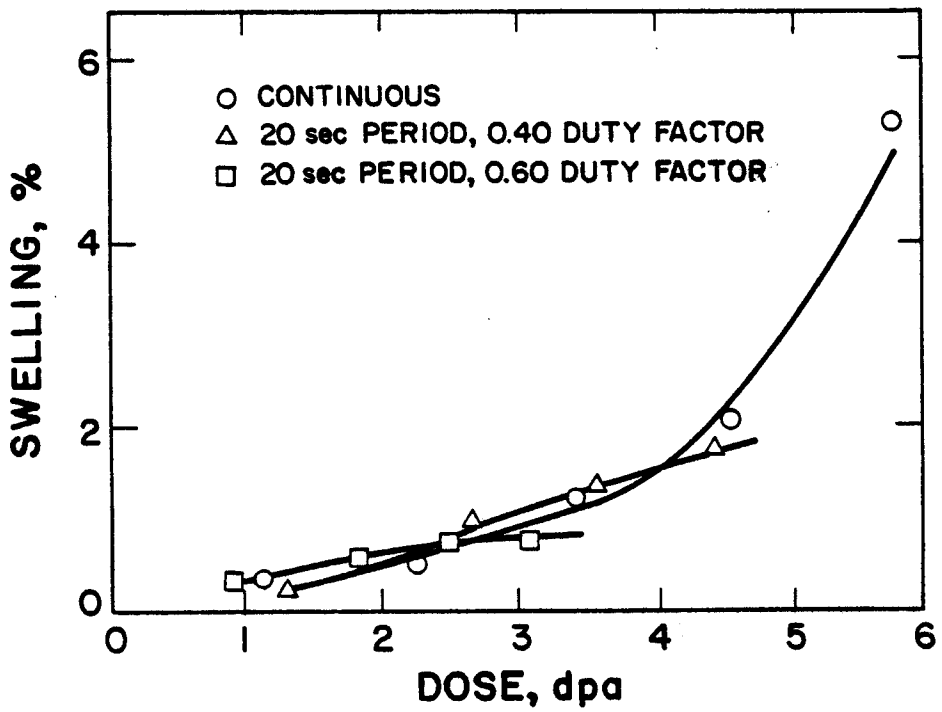

Figure 16 - Fluence dependence of swelling for the continuous irradiation and two pulsed irradiations with equal pulse periods but different duty factors.

where the temperature was above the critical temperature for coalescence, beam cycling was found to enhance the coalescence effect. The effect on bubble growth was seen to be considerable, and very large bubbles were observed. The critical temperature of T = 898°K at which bubble growth by coalescence is the dominant growth process was concluded to be reduced by about 50°K when beam cycling takes place.

Michel, Hendrick and Pieper [45] irradiated Ni samples with deuteron beams to study the transient phase of irradiation-induced creep. This could be important to startup and shutdown phases of Tokamaks or Mirror reactors. Their experimental results indicated that 22 MeV deuteron irradiation of Ni at 224°C produces a transient creep stage that is essentially complete after irradiation for 8 hours. Microstructural characterization of specimens irradiated for 2,4 and 8 hours revealed a rapid decrease in dislocation density and a similar increase in defect cluster/loop density with increased irradiation time. Assuming the obstacle height in the climb-glide mechanism to be the average loop diameter, and using the time-dependent loop number densities, they concluded that the climb-glide mechanism correlates well with the experimental findings.

More recently, Simonen and Hendrick [46] conducted experiments to study the light ion irradiation-induced creep in nickel. The creep response at 200°C of both cyclic and steady state deuteron irradiated nickel was analyzed and compared with experiments. We will report on their experiments in this section, and the theory will be presented in the next section. The cycle characteristics were chosen to be similar to one operating scenario possible for a Tokamak Reactor, i.e., 1000 seconds irradiation followed by 100 seconds of annealing. Specimen strain (creep) was measured continuously with a non-contacting laser extensometer. The 0.15 mm, 25% cold-worked, sheet specimens were irradiated in uniaxial tension with a 17 MeV deuteron beam. The cyclic

irradiation temperature was 447°K (test 2-10-1), whereas the continuous beam irradiation temperatures were 500°K (test 2-7-1) and 459°K (test 2-4-1). The imposed stress was 205 MPa for all three tests. The continuous beam fluxes were 10.9 $\mu a/cm^2$ (2-7-1) and 11.3 $\mu a/cm^2$ (2-4-1) and the time averaged cyclic beam current was 11.6 $\mu a/cm^2$. The displacement damage rate was calculated with the computer code E-DEP-1 [46], using a modified electronic stopping power [47]. The time averaged damage rate used for the cyclic creep theory calculations was 5.9×10^{-7} dpa/sec.

The creep response for both the cyclic and continuous irradiations is shown in Fig. (17). The effect of pulsing the irradiation produced a threefold enhancement of both the primary and secondary creep rates. In addition, the transition from primary to secondary creep was extended by the pulsing.

6.2 Theoretical Treatments

Koehler considered point defect generation in pulsed impure solids [49]. In his analysis, he assumed that a shock wave, such as that generated by laser bombardment, will deliver equal momenta to both the solid and impurity atoms. Thus, a relative velocity of the impurities is produced. In one example of silver impurities in aluminum bombarded by a 23 joule laser pulse, he concluded that the effective relative energy of the moving silver atoms is $\sim$50 keV. This is sufficient to produce about 580 pairs of point defects. In his analysis, Koehler pointed out the possibility that this mechanism can be responsible for the high vacancy concentrations found in the MS simulation experiments [38].

6.2.1 Nucleation of Microstructural Features

Choi, Bement and Russell [50] studied the effects of Fusion Reactor Burn Cycles on void nucleation in the absence of impurities. The flow of voids between size classes n to (n+1) was given by:

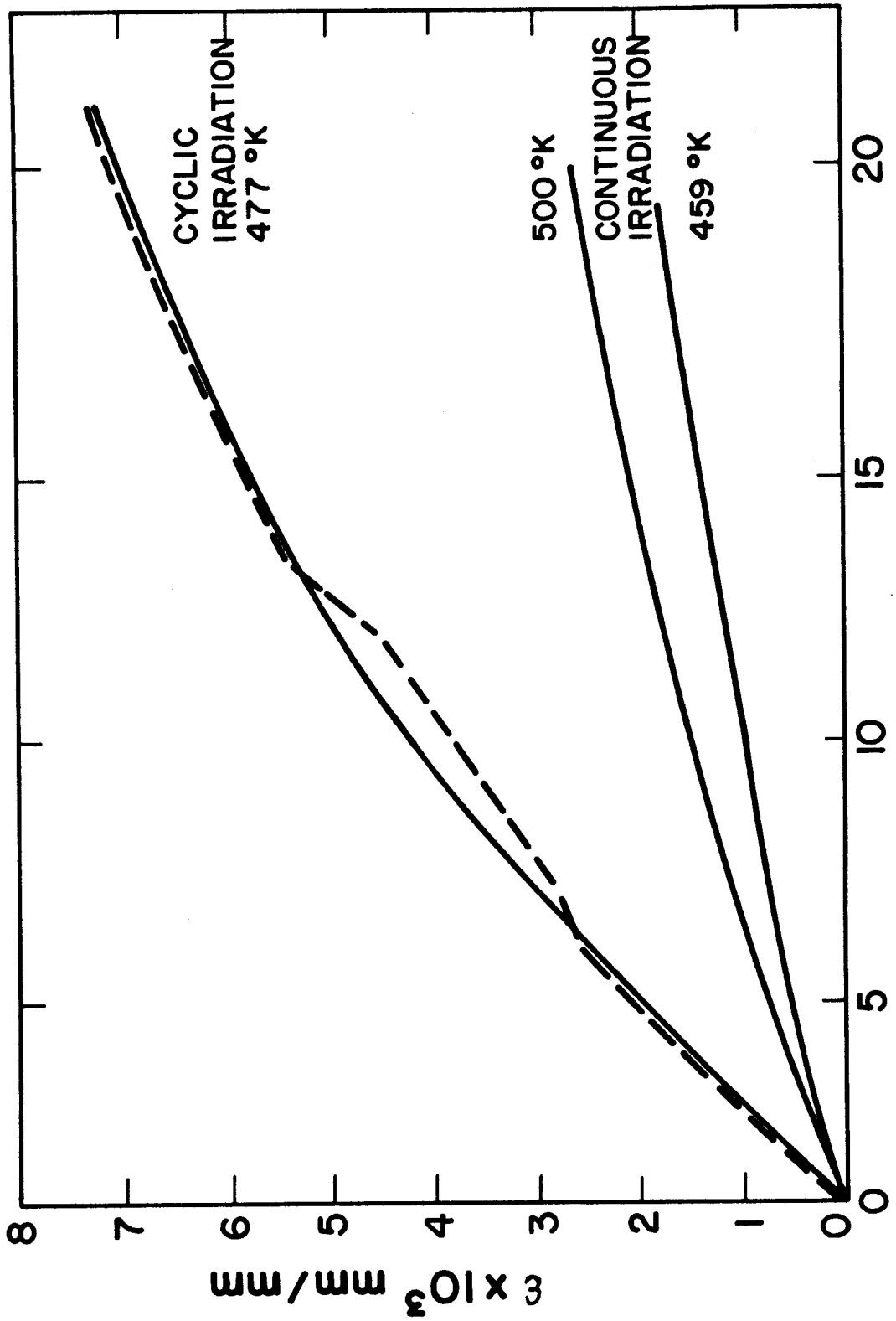

Figure 17 - Comparison of cyclic and continuous irradiation creep. The dashed curve indicates strain fluctuations in the raw data for the cyclic test whereas the solid curves indicate an averaged creep response.

$$J(n,t) = \beta_v(n)C(n,t) - [\beta_i(n+1)+\alpha(n+1)]C(n+1,t) \quad . \qquad (21)$$

Application of the equation of continuity converts equation (21) to a rate equation for the concentration C(n,t)

$$\frac{\partial C(n,t)}{\partial t} = -[\beta_v(n)+\beta_i(n)+\alpha_n(n)]C(n,t) + [\beta_i(n+1)+\alpha_v(n+1)]C(n+1,t)+\beta_v(n-1)C(n-1,t) \qquad (22)$$

where J(n,t) is the flux of n-vacancy to (n+1) vacancy voids, C(n,t) is the number of n-vacancy voids per unit volume at time t, $\beta_{v,i}(n)$ are vacancy/interstitial capture rates of n-vacancy voids and $\alpha_v(n)$ is the vacancy emission rate of an n-vacancy void. Choi et al. [50] proceeded to solve equations (22) with the impingement and emission rates depending on the instantaneous point defect concentration. This resulted in consumption of excessive computer time. Consequently, two approximations were made to relieve the computational difficulties.

1. The duty cycle, temperature and point defect concentrations were taken as step functions of time.
2. The void size classes were grouped for evaluation.

The resulting equations were given as

$$J(n,t) = [\beta_v(n+\frac{\Delta n}{2})C(n,t) - (\beta_i(n+\frac{\Delta n}{2})+\alpha_v(n+\frac{\Delta n}{2}))C(n+\Delta n,t)]/\Delta n \quad . \qquad (23)$$

The burn cycle was taken as 50 seconds, the total cycle time as 100 seconds and the atomic displacement rate was varied around 10^{-6} dpa/second. It was noted from their calculations that the incubation time for void nucleation is larger than the burn time by as much as an order of magnitude. They concluded therefore that the steady-state nucleation theory is inapplicable, and that the transient treatment is needed for pulsed irradiation.

The effect of gaseous impurities (such as helium) was modeled by assuming an internal pressure of 6×10^9 dyne/cm^2 during the burn cycle, and no gas gain or loss during the rest of the cycle. Nongaseous impurities were approximated by modifying the void surface energy.

It was found that very little void dissolution occurred during the cooling cycles. The effect of inert gas or surface-active impurities was found to decrease the critical nucleus size and to sharply increase the void nucleation rate. Inert gas was also concluded to further increase the swelling rate by preventing complete dissolution of voids during the cooling cycle.

Odette and Myers [51] examined the effects of pulsing on void nucleation. They formulated the time dependent rate equations describing voids of any size as

$$\begin{aligned} C_1 &= \text{prescribed vacancy concentration} \\ \frac{dC_1}{dt} &= \beta_1 C_1 - (\beta_2+\alpha_2)C_2 + \alpha_3 C_3 \\ &\vdots \\ \frac{dC_k}{dt} &= \beta_{k-1} C_{k-1} - (\beta_k+\alpha_k)C_k \end{aligned} \tag{24}$$

The current between adjacent clusters was written as

$$J_i = \beta_i^v C_i - \alpha_{i+1}^v C_{i+1} - \beta_{i+1}^v C_{i+1} \tag{25}$$

Point defect concentrations as well as impingement and emission rates were simplified as square wave functions in their preliminary analysis. The vacancy concentration was taken as $C_v = SC_v^e$ during each pulse, where S is the vacancy supersaturation and C_v^e is the thermal equilibrium vacancy concentration; and $C_v = 0$ during intervals between pulses. The maximum cluster size in their calculations was determined by solving for the constrained equilibrium ($J_i = 0$) distribution as described by Russell [52]. The cluster size

i+1 corresponding to an energy kT below the free energy maximum was taken as the nucleated state. Notice that this procedure contrasts with the Choi et al. [50] conclusions on the inapplicability of steady-state assumptions in the treatment of pulsed irradiation.

Rather than using a time consuming numerical integration, Odette and Myers used an analytical method for analyzing the decay processes in the interval between pulses. This resembles the Bateman solution of series radioactive decay [53]. The average nucleation rate $\bar{J}$ during each pulse was determined as

$$\bar{J} = \int_{tp} J_k dt/t_p \quad . \tag{26}$$

The ratio of $\bar{J}$ to the normal steady-state nucleation rate, J_{ss}, was considered as a good measure of the nucleation throttling due to pulsing. In their work, the steady-state source strength was taken to be the same as that existing during the pulse. Their calculations showed that a substantial reduction in the effective nucleation rates resulted from pulsed versus steady-state irradiations. The largest effect was found to be for short pulses and long pulse intervals. It is not clear, however, whether this conclusion is due to the effect of pulsing or because their comparison was not conducted at the same total dose in the considered pulsed and steady-irradiation systems.

Ghoniem and Cho [54] formulated a time-dependent rate theory for the simultaneous clustering of point defects during irradiation. Based on Wolfer's calculations for point defect diffusion [55], they incorporated size-dependent bias factors in computing point defect impingement and emission fluxes, which were determined by considering mixed rate reactions (diffusion and surface limited).

Assuming a homogeneous medium, and using the nomenclature of chemical rate theory, they wrote the following set of equations for the fractional concentrations:

$$\frac{dC_v}{dt} = P + K_i^c(2)C_1C_{2v} + (2\gamma_v^c(2) - K_v^c(2)C_v)C_{2v} + \sum_{x=3}^{x_{max}} (\gamma_v^c(x) - K_v^c(x)C_v)C_{xv} - \sum_{x=3}^{x_{max}} K_v^\ell(x)C_vC_x$$

$$\frac{dC_{2v}}{dt} = \frac{1}{2} K_v^c(1)C_v^2 + \gamma_v^c(3)C_{3v} + K_i^c(3)C_iC_{3v} + \rho_d D_{2v} C_{2v}^e - K_v^c(2)C_vC_{2v} - K_i^c(2)C_iC_{2v} - \gamma_v^c(2)C_{2v} - \rho_d D_{2v} C_{2v}$$

$$\vdots$$

$$\frac{dC_c(x)}{dt} = K_v^c(x-1)C_vC_c(x-1) - \{K_i^c(x)C_i + K_v^c(x)C_v + \gamma_v^c(x)\}C_c(x) + \{K_i^c(x+1)C_i + \gamma_v^c(x+1)\}C_c(x+1) \qquad (27)$$

$$\frac{dC_i}{dt} = P + K_v^\ell(2)C_vC_{2i} - K_c^c(1)C_i^2 - \alpha C_vC_i - K_i^\ell(2)C_iC_{2i} - K_i^c(2)C_iC_{2v} - \sum_{x=3}^{x_{max}} K_i^\ell(x)C_iC_{xi} = \sum_{x=3}^{x_{max}} K_v^c(x)C_iC_{xv} - Z_i\rho_d D_i C_i$$

$$\frac{dC_{2i}}{dt} = \frac{1}{2} K_i(2)C_i^2 + K_v(3)C_vC_{3i} - K_i^\ell(2)C_iC_{2i} - K_v^\ell(2)C_vC_{2i}$$

$$\vdots$$

$$\frac{dC_\ell(x)}{dt} = K_i^\ell(x-1)C_iC_\ell(x-1) + \gamma_v^\ell(x-1)C_\ell(x-1) - \{K_i^\ell(x)C_i + K_v^\ell(x)C_v + \gamma_v^\ell(x)\}C_\ell(x) + K_v^\ell(x+1)C_vC_\ell(x+1)$$

with the parameters; irradiation production rate of Frenkel pairs, P = (at/at/s), α = point defect recombination coefficient (s^{-1})

$$\alpha = 48\nu_i \exp(-\frac{E_i^m}{kT}) \quad , \tag{28}$$

$Z_{v,i}$ = point defect-straight dislocation bias factors, $\rho_d(cm^{-2})$ = straight dislocation density, $D_{v,i}(cm^{-2}\ s^{-1})$ = point defect diffusion coefficients, $D_{2v}(cm^{-2}\ s^{-1})$ = divacancy diffusion coefficient [56],

$$D_{2v} = \nu_v a^2 \exp(-\frac{E_m^{2v}}{kT}) \tag{29}$$

E_m^{2v} = migration energy of a divacancy, C_{2v}^e (at/at/s) = divacancy thermal fractional concentration [56],

$$C_{2v}^e = 6\ \exp(-\frac{2E_F^v - E_B^{2v}}{kT}) \quad . \tag{30}$$

The set of rate equations (27) are derived by considering the balance between various production and destruction processes for a certain cluster size. x is defined as the cluster size in atomic units, i stands for an interstitial, v for a vacancy, ℓ for a loop, and c for a cavity (void). Their theory was applied to both steady and pulsed-irradiation conditions. Ghoniem [57] studied the results of steady irradiation as compared to the microstructure of two equivalent pulsed systems. The irradiation conditions of the first pulsed system represented ICFRs with a pulse duration of 10^{-6} seconds and a period of 1 second. The second system was chosen to represent a pulsed simulation facility, such as a pulsed accelerator, with 10^{-3} seconds pulse duration and a period of 1 second. For the results to be meaningful, the average damage rate as well as the total dose were kept the same in all cases.

Figure (18) shows the interstitial loop size distribution of the steady irradiation system (e.g., Tokamak or Mirror Fusion Reactor), as compared to the Simulation Facility (Pulsed Accelerator) and the ICFR case. The distributions are given after an accumulated dose of $7x10^{-6}$ dpa. The distribution is found to be non-symmetrical for the highly pulsed system (ICFR) and to approach a Gaussian shape for the steady irradiation case (Tokamak or Mirror). The peak size is about 4 interstitials for the ICFR, 21 for the Pulsed Accelerator and 34 for the Tokamak. A comparison of the average loop size for the three systems is shown in Fig. (19), as a function of irradiation time. It is shown that, in the steady irradiation case, the average loop size increases linearly after an initial transient. On the other hand, the average loop size increases just at the beginning of every pulse in the ICFR and accelerator cases. Interstitial loops are shown to be smaller for the highly pulsed systems. After a dose of $7x10^{-6}$ dpa, the average loop size is about 34 atoms for the Tokamak, 21 for the Pulsed Accelerator and 7 for the ICFR. It is interesting to note that the average and peak size coincide for the cases of Tokamak and Pulsed Accelerator. The total loop concentrations are shown as functions of irradiation time and accumulated dose in Fig. (20). It can be observed from the figure that the loop concentration is much higher in the two pulsed systems. After 10 seconds of irradiation, the loop concentration is about 10^{10} loops/cm^3 for the Tokamak reactor, $2x10^{15}$ loops/cm^3 for the Pulsed Accelerator and $4x10^{16}$ loops/cm^3 for the ICFR.

The simultaneous formation of small-size vacancy clusters (voids) was also studied. It was found that, at the initial stages of irradiation in ICF conditions, the diinterstitial formation rate is faster than the point defect recombination rate. This effect protects the single vacancies from

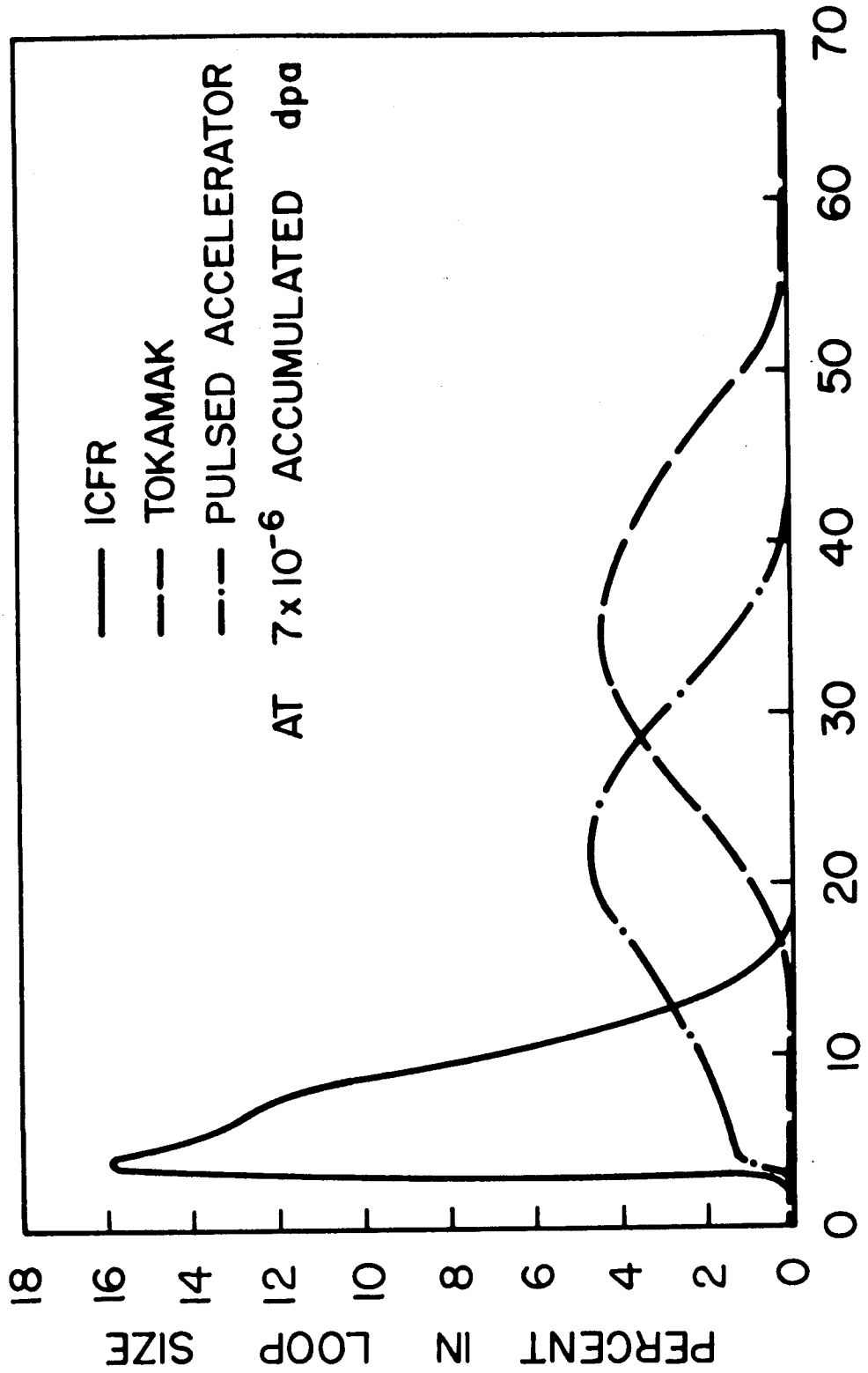

Figure 18 - Comparison of interstitial loop size distributions after 7 seconds of irradiation time between steady and pulsed irradiation systems.

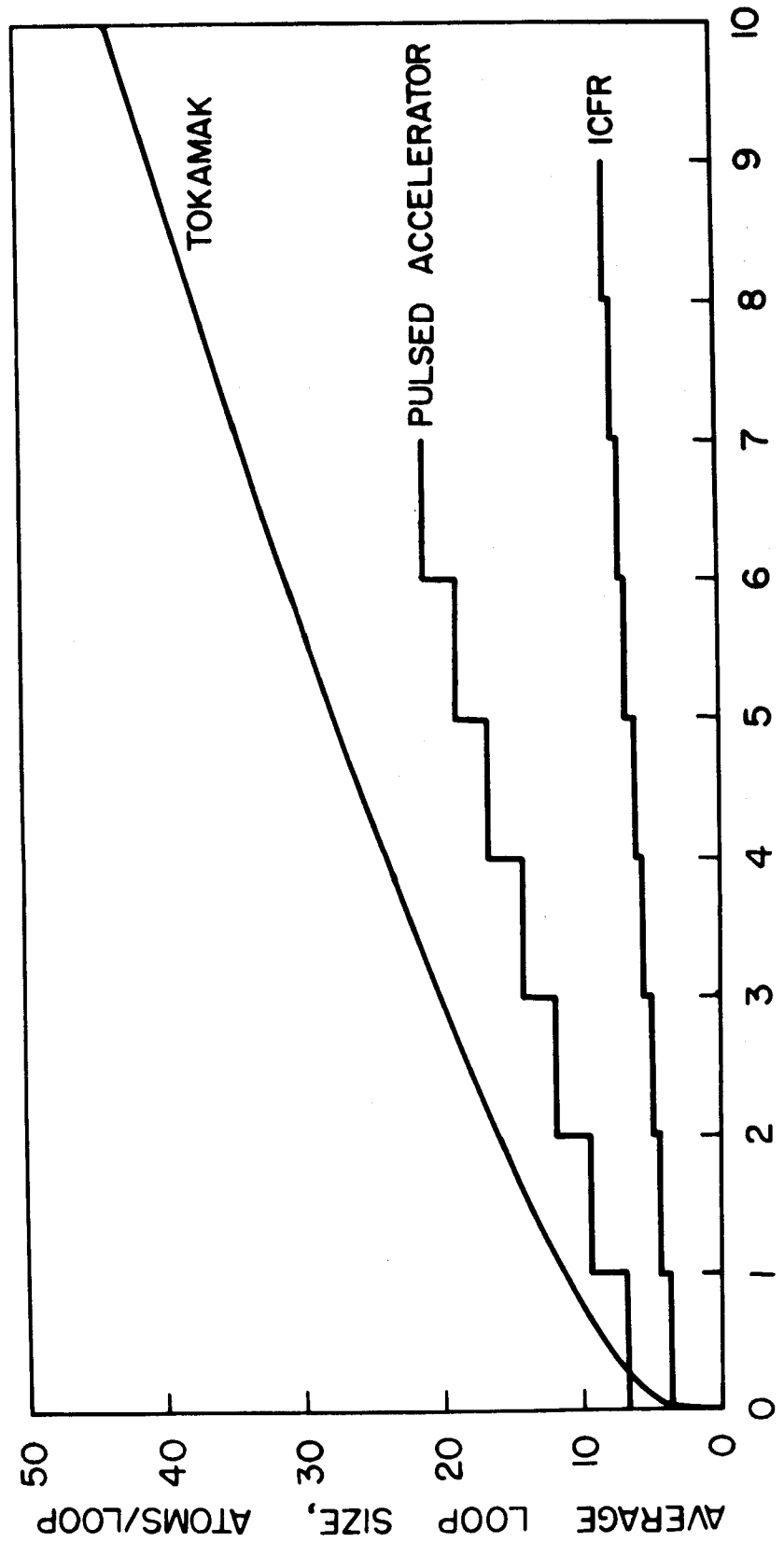

Figure 19 - Comparison of average loop sizes between steady and pulsed irradiation systems during 10 seconds of irradiation.

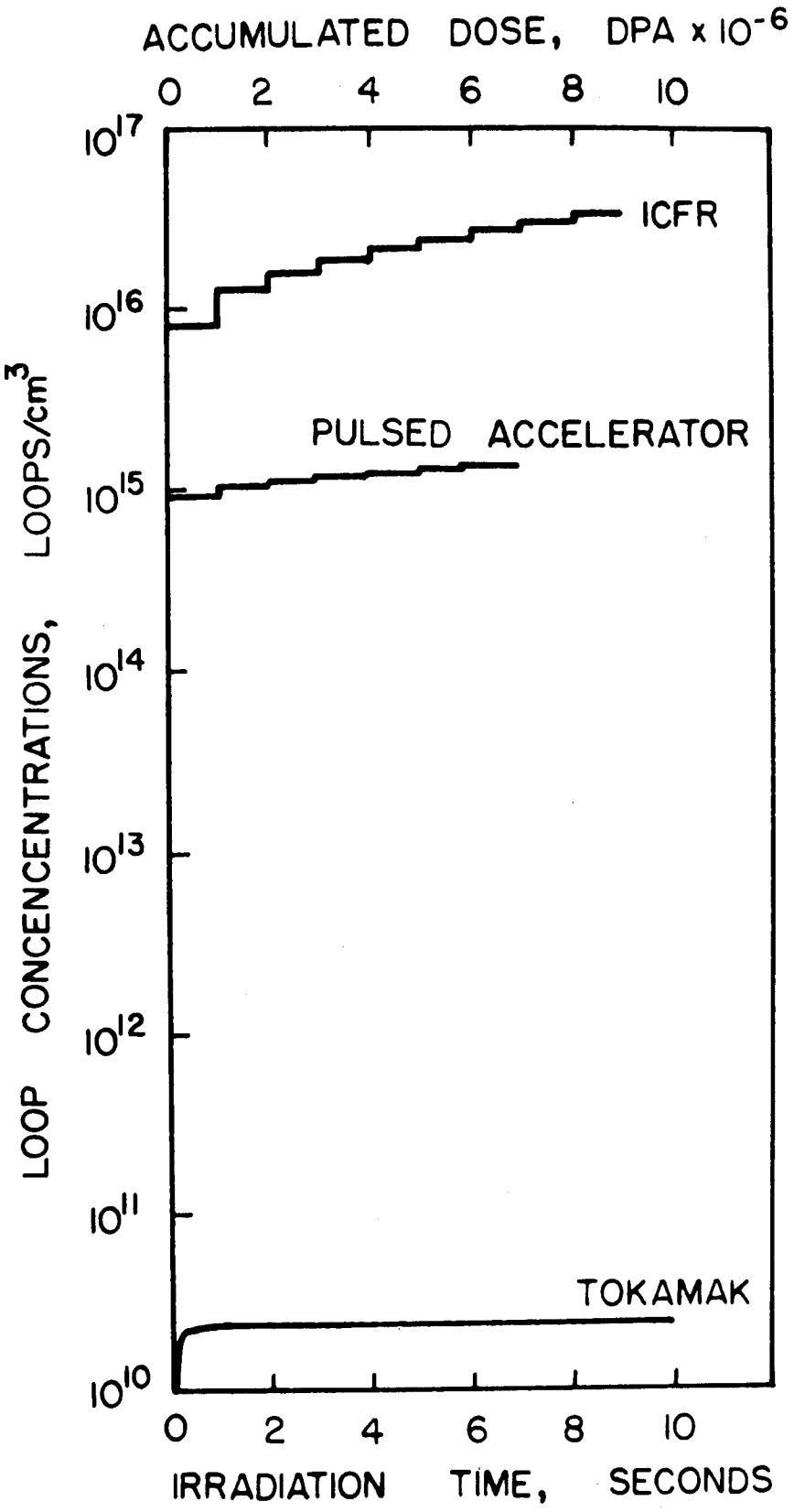

Figure 20 - Comparison of total loop concentrations between steady and Pulsed irradiation systems during 10 seconds of irradiation.

recombining with interstitials, and thereby increases the vacancy supersaturation in the ICFR first wall. Figure (21) shows the total microvoid concentrations (up to a cluster of 10 vacancies) as functions of irradiation time. It is interesting to note that some of the microvoids dissolve during the annealing period. However, the damage produced during each pulse results in large discontinuous additions to the total void population. At the end of seven seconds the total microvoid concentration is $\sim 10^{13}$ voids/cm^3 for the ICFR, while it is $\sim 10^{12}$ voids/cm^3 for the Pulsed Accelerator and Tokamak systems.

The basic conclusion from this study is that irradiation pulsing will enhance the nucleation and retard the growth of both interstitial loops and microvoids. This contrasts with the nucleation throttling idea of Odette and Myers [51], but agrees qualitatively with Powell and Odette's explanation of the effects of Pulsed HVEM irradiation on microstructure evolution [42].

6.2.2 Growth of Microstructural Defects

The complexity of the interactions between the various components of the microstructure during irradiation has led to a simplified distinction between the nucleation and growth phases of these components. It was experimentally observed, that the number densities of the microstructural components, such as dislocation loops, voids and gas filled cavities, do not change appreciably after a certain irradiation dose [58]. Such an observation has been useful in rendering the microstructure studies more tractable.

The effects of cyclic irradiation on the growth of gas containing voids was first studied by Schiffgens et al. [59] and later by Ghoniem and Kulcinski (GK) [60]. Schiffgens, Graves and Doran (SGD) [59] separated their analysis into three parts. The goal of the first part of this

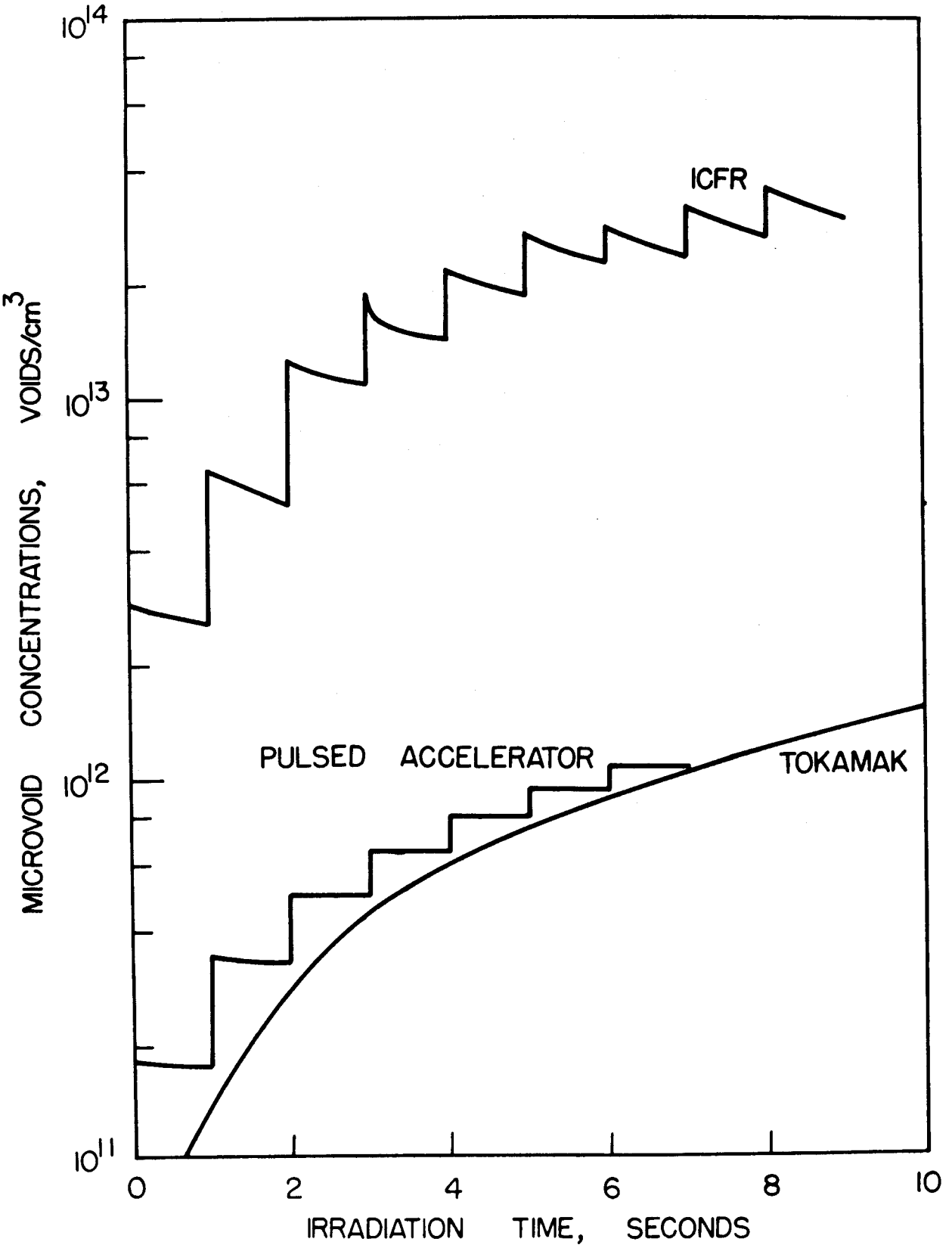

Figure 21 - Comparison of supersaturation of vacancies between steady and pulsed irradiation systems during 10 seconds of irradiation.

analysis was to obtain the probabilities for vacancy and interstitial leakage as functions of the dislocation density and temperature. The random dislocation configuration of a real solid was approximated by an idealized configuration consisting of a bundle of parallel straight dislocations for which end effects are neglected. The coupled, steady state, continuity equations for vacancies and interstitials, including the interactions between the defects and the stress fields of the dislocations, were solved for the concentration profiles in order to obtain the leakage rates of each and relate them to their average concentrations at the dislocation densities and temperatures of interest.

In the second part of the SGD analysis, it was assumed that vacancy and interstitial leakage rates (for a given temperature, dislocation density and set of defect properties) were proportional to the respective average concentrations at all times. The coupled rate equations which describe the defect balance throughout the cycle in terms of the spatially averaged concentrations were solved to obtain the time dependences of these average concentrations.

The third part of the analysis was built on the first and the second. It was assumed that voids growing among the dislocations may be treated simply as growing in the time varying average concentrations resulting from the annihilation-leakage competition. The fields and the spatial variations in the vacancy and interstitial concentrations near the dislocations were ignored. The uncoupled continuity equations describing diffusion in the region surrounding the void were solved with the requirement that the average concentration within the region be equal to the average concentration throughout the material at all times. For any given calculation, the volume source

terms for Frenkel pair production were obtained from a detailed analysis of damage production for the particular irradiation conditions of interest.

SGD's work [59] identified four regimes associated with void growth in pulsed systems. The first regime was characterized by two interrelated parameters, a zero growth pulse length t' and a minimum interval between pulses. This analysis shows that if the irradiation pulse length is less than about 10 μsec and the interval between pulses is greater than about 20 t', no void growth is possible in stainless steel regardless of temperature, dislocation density and pulse amplitude (instantaneous displacement rate). This conclusion is true provided no voids form in displacement cascades which are large enough to survive the time between pulses.

The second regime was characterized by a pulse amplitude which is large enough for growth of void nuclei but with pulse lengths short enough and/or cycle lengths long enough that void growth during the pulse is completely nullified by the shrinkage between pulses. The third regime was defined by pulse parameters which not only permit voids to grow on given nuclei but for all irradiation times cause more growth during a pulse than shrinkage between pulses. The boundaries for these regimes were more difficult to quantify. For any given set of pulse and cycle lengths, the regime boundaries were recognized to be complex functions of the physics of void nuclei, the dislocation density, and the temperature and displacement pulse amplitudes.

In the fourth regime, there was essentially no shrinkage between pulses and the total void growth is just the net growth per pulse summed over all pulses. Sample calculations showed that, for pulse parameters in the range of interest for CTR design, void growth is significantly altered. For large voids, with a dislocation density of 5×10^{10} cm^{-2}, at 500°C, the rate of change in volume of a void during a continuous irradiation at a displacement rate of

$1x10^{-6}$ dpa/sec is about 2.5 times the rate of change in volume of the same size void during a pulsed irradiation with $t_p = 0.4$ sec, $t_c = 10.4$ sec, and an average displacement rate of $1x10^{-6}$ dpa/sec.

GK [60] conducted a simplified study of void growth kinetics during an irradiation pulse typical of ICFRs. Assuming that dislocations are the most dominant sinks for point defect absorption, they obtained analytical solutions of the time-dependent rate equations for the average vacancy concentration, interstitial concentration and the average size void radius. Point defects were assumed to be generated as delta functions at the start of each irradiation pulse. Parametric studies on the sensitivity of void growth and annealing kinetics to irradiation temperature, dislocation density, amount of damage contained in each pulse and pulse repetition rate were established. The average void was found to go through an initial void shrinkage phase due to the fast migration of interstitials to pre-existing voids. This was found to be followed by a growth phase when voids receive the slower moving vacancies. During the entire pulse period, vacancies are emitted from the void surface at a rate dictated by the void surface energy and irradiation temperature. The competition between these three processes was established to determine the final fate of a pre-existing void. It was concluded that the combination of long periods and high temperatures can lead to a reduction of material swelling due to void growth in ICFRs.

Extending the fundamental notions in the rate theory applications to microstructural response during irradiation, GK [61] constructed a Fully Dynamic Rate Theory for void swelling during time-dependent irradiations. In their general formulation, a state variable approach was used to describe the behavior of various components. The state of a metal during irradiation was described by a vector $\bar{Y}$, whose components were defined as follows:

Y(1) = average void radius in cm, r_c

Y(2) = average nonaligned interstitial loop radius in cm, r_{il}^n

Y(3) = concentration of nonaligned vacancy loops per cm^3, N_{vl}^n

Y(4) = concentration of single vacancies tied up in nonaligned vacancy loops in at/at, q_v^n

Y(5) = total single vacancy concentration in at/at, C_v

Y(6) = total single interstitial concentration in at/at, C_i

Y(7) = average aligned interstitial loop radius in cm, r_{il}^a

Y(8) = concentration of aligned vacancy loops per cm^3, N_{vl}^a

Y(9) = concentration of single vacancies tied up in aligned vacancy loops in at/at, q_v^a

Y(10) = network creep strain in cm/cm, e

A loop is defined to be aligned if the stress is perpendicular to the plane of the loop. In a mathematical formulation that incorporates the kinetic behavior of different irradiation produced species, there exists a wide range of time constants related to those different components. A time constant, λ, is defined here as the inverse of the time required to go through one e-folding change in a particular property, i.e., the ln(parameter) = $-\lambda t$.

The diffusion coefficient of single interstitials is orders of magnitude larger than the diffusion coefficient of single vacancies so that once they are created by irradiation, interstitials tend to diffuse quickly to different sinks and to annihilate vacancies. Since the time constants of single point defects depend on the sinks present at a particular instant, they are explicit functions of the metal's microstructure, and therefore, implicit functions of time. Their microstructural dependence can be simply expressed as

$$\lambda_i = \lambda_i^d + \lambda_i^c \tag{31}$$

$$\lambda_v = \lambda_v^d + \lambda_v^c \tag{32}$$

$$\lambda_i^d = \rho_d D_i Z_i \tag{33}$$

$$\lambda_i^c = 4\pi N_C r_c D_i \tag{34}$$

$$\lambda_v^d = \rho_d D_v Z_v \tag{35}$$

$$\lambda_v^c = 4\pi N_C r_c D_v \tag{36}$$

where

λ_i is the total single interstitial time constant, s^{-1},

λ_v is the total single vacancy time constant, s^{-1},

λ_i^d is the single interstitial time constant due to dislocations, s^{-1},

λ_i^c is the single interstitial time constant due to voids, s^{-1},

λ_v^d is the single vacancy time constant due to dislocations, s^{-1},

λ_v^c is the single vacancy time constant due to voids, s^{-1}.

The importance of each type of sink on the dynamic behavior of point defects is reflected in the specific removal rate of the defect to that sink. Individual sink removal rates can be expressed as their relevant time constant, λ, multiplied by the temporal concentration of point defects. As indicated before, mutual recombination of point defects is a second order reaction that depends on the product of both concentrations. Total point defect removal rates are then expressed as:

$$P_{si} = \lambda_i C_i \tag{37}$$

$$P_{sv} = \lambda_v C_v \tag{38}$$

$$P_r = \alpha C_v C_i \tag{39}$$

$$\alpha = g(v_i \exp(-E_i^m/kT) + v_v \exp(-E_v^m/kT)) \tag{40}$$

where

P_{si} is the total sink removal rate for interstitials, s^{-1},

P_{sv} is the total sink removal rate for vacancies, s^{-1},

P_r is the total recombination rate of vacancies and interstitials, s^{-1},

α is the recombination coefficient, s^{-1},

g is the number of unstable sites around a vacancy,

$v_i \exp(-E_v^m/kT)$ is the interstitial jump frequency, s^{-1},

$v_v \exp(-E_v^m/kT)$ is the vacancy jump frequency, s^{-1}.

A FORTRAN Computer Code, TRANSWELL [62] was developed to solve the previous system of equations under a variety of irradiation conditions. Among TRANSWELL's subroutines is the GEAR package [63] for the solution of the initial value problem for systems of ODE's that have the form

$$\dot{Y} = f(Y,t) \tag{41}$$

or more specifically,

$$\frac{dY_i(t)}{dt} = f(Y_1(t),\ldots,Y_N(t),t) \tag{42}$$

where Y, $\dot{Y}$ and f are vectors of length $N \geq 1$.

The basic methods used for the solution are of implicit linear multistep type. The implicitness of the basic formulae requires an algebraic system of equations be solved at each time step.

The GEAR package allows the step size and the order to vary in a dynamic way throughout the problem. The system of equations described in the previous section is a highly stiff system due to the wide range of time constants for the different components. This behavior is particularly important in transient or pulsed irradiation analysis [61,64], as briefly described in the next section.

To illustrate the application of this theory, GK studied the time-dependent point defect and microstructure for 1 MeV electron irradiation of M316 S.S. Since collision cascades are not produced in electron irradiated metals, vacancy loop formation is not expected and the cascade efficiency can be set equal to zero. Furthermore, if the sample is not subject to external stresses we will have only four components of the vector Y; Y(1), Y(2), Y(5) and Y(6) or r_c, r_i^n, C_v and C_i respectively.

The materials parameters for M316 steel (solution treated) are those of Bullough, et al. [65]. The calculations were performed at 600°C with an experimentally measured void concentration [66] while the interstitial loop concentration was taken at 10^{14} loops/cm^3.

The four equations for r_c, r_i^n, C_v and C_i were then solved numerically with the initial conditions

$$r_c(0) = 10 \text{ Å} \tag{43}$$

$$r_{il}(0) = \sqrt{4r_c^3(0)N_c/3bN_{il}} \tag{44}$$

$$P_g(0) < 2Y/r_c(0) \ . \tag{45}$$

It was assumed here that the microstructure has already nucleated and its time dependence is studied after the radiation has started. The time dependent behavior of the vacancy and interstitial concentrations are shown in Figure (22). At irradiation times of the order of the first few microseconds, neither interstitials nor vacancies are mobile enough to migrate to neutral and biased sinks. Also their concentrations will be so low that the mutual recombination is negligible. Under these conditions the rate of change of the concentration of vacancies and interstitials is almost equal to the production rate. In Figure (22) the initial slope of $C_i(t)$ and $C_v(t)$ is about 5×10^{-3} at/at/sec; the actual production rate. The build-up of the interstitial concentration coupled with their high mobility will cause the interstitial sink

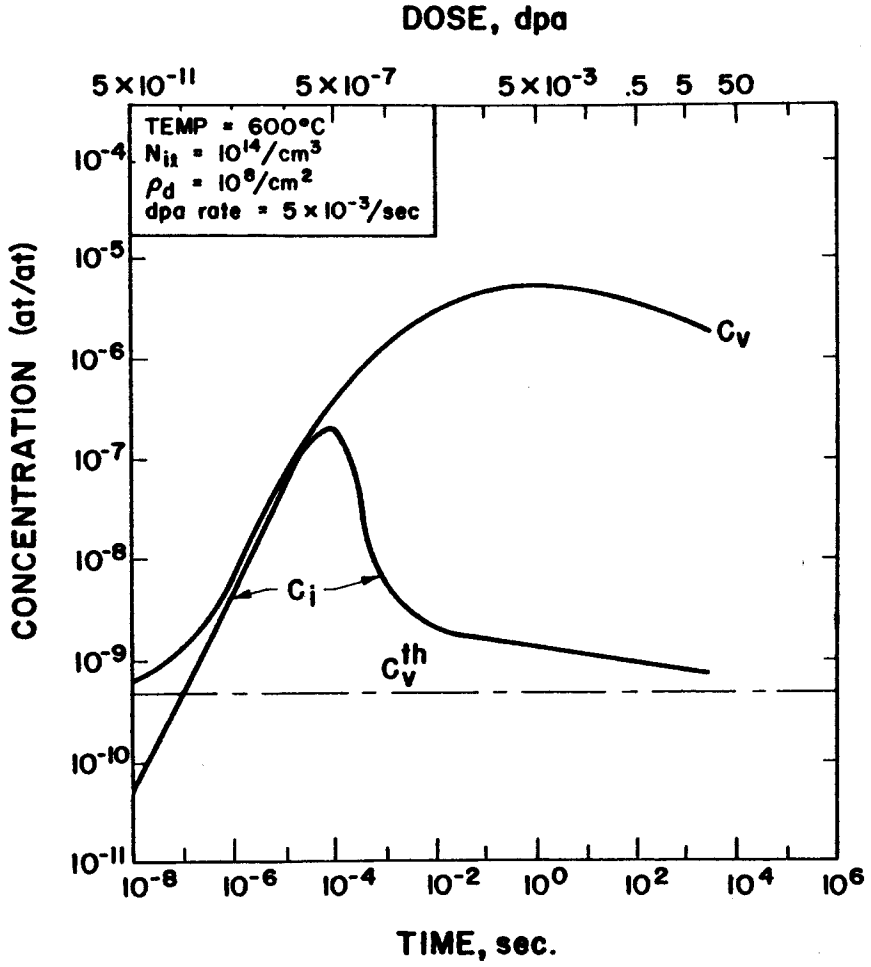

Figure 22 - Point defect concentrations in electron irradiated M316 SS using the fully dynamic rate theory (FDRT).

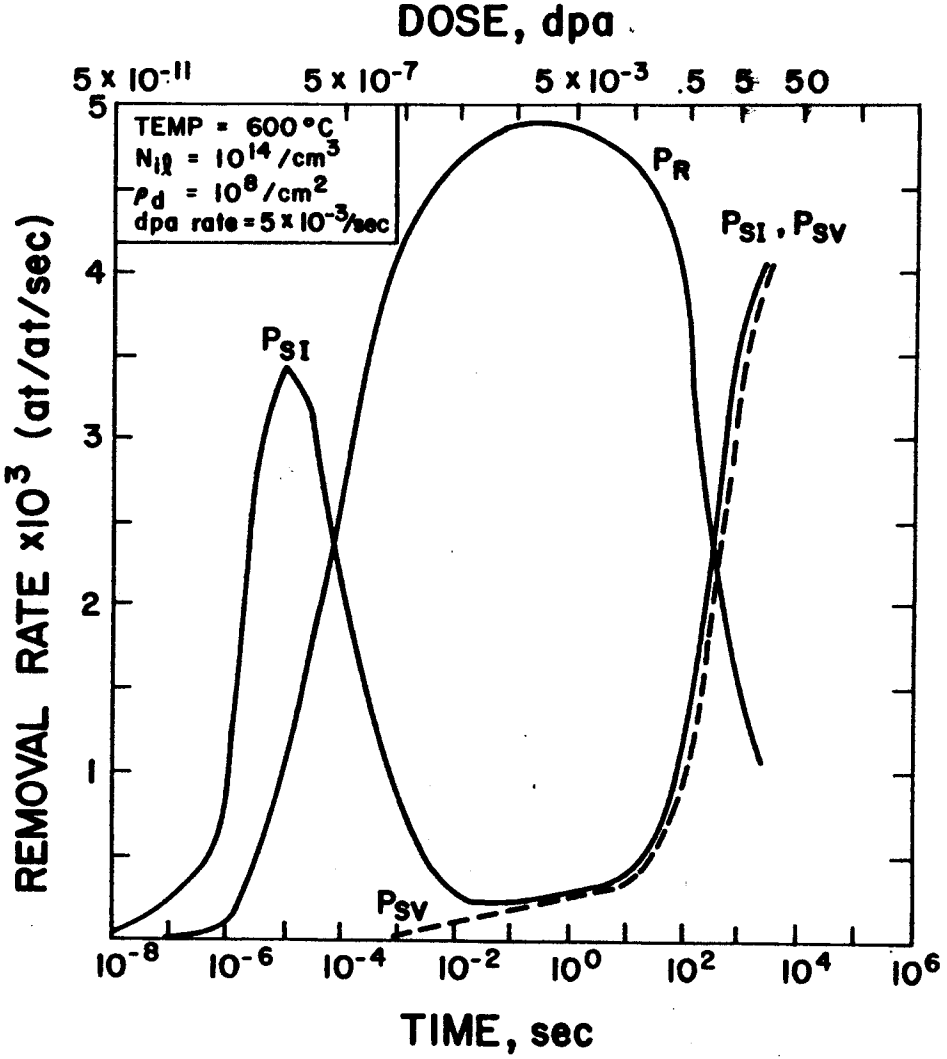

Figure 23 - Removal rates P_R, P_{SI}, P_{SV} in electron irradiated M316 SS using fully dynamic rate theory (FDRT).

removal rate to increase for ∿10 microseconds. The concurrent buildup of the vacancy concentration also produces a high recombination rate (which is proportional to $C_v C_i$).

Consequently the total interstitial concentration passes through a maximum and then decreases value as a function of time. As time progresses, the high vacancy concentration and the high mobility vacancies will result in a vacancy sink removal rate which increases with time. After a few vacancy mean lifetimes the vacancy concentration will decrease with time producing the broad maximum as shown in Figure (22).

The absolute defect removal rates are shown in Figure (23). As expected, the interstitial sink removal rate (P_{SI}) is high at short times ($\sim 10^{-5}$ seconds) while the recombination rate (P_R) is low. The buildup of vacancy concentration causes the recombination rate to dominate after $\sim 10^{-4}$ seconds. Eventually the buildup of dislocation loop and void sinks causes the point defect removal rates to become dominant again after ∿100 seconds (∿0.5 dpa). Note that in Figure (23), P_R is the point defect mutual recombination rate, P_{SI} is the total sink removal rate for interstitials and P_{SV} is the total sink removal rate for vacancies in units of at/at/sec.

The significance of Figures (22) and (23) is that there is a complex time relation between the point defect concentration rates and the dynamically changing microstructure. It is important to recognize the chronology of the defect structure development, because the microstructural description at 10 or 100 dpa may be entirely different than that during the early stages of irradiation.

Although the Fully Dynamic Rate Theory was primarily designed for applications where the irradiation source is a strong function of time, GK correlated the theory to existing experimental data on void swelling during both

steady and pulsed irradiations [67]. The application of the theory showed a successful prediction of the swelling behavior of different metals over a wide range of temperatures, dose rates, bombarding particles and irradiation source time structures. Swelling of 316 stainless steel, aluminum and nickel bombarded with heavy ions, neutrons and electrons at does rates varying from 10^{-6} to 10^{-1} dpa/second was studied for both steady-state and pulsed irradiations. A recent experimental study by Taylor et al. [40] has illustrated that pulsed irradiation of Ni to the same damage level and at the same damage rate as for a corresponding sample irradiated in a steady-state fashion, can give significantly different microstructural results. First, several Ni specimens were pre-injected with 5 appm of helium and then irradiated at 600°C to 5 dpa with a steady-state damage rate of $3x10^{-3}$ dpa/sec (A). Three specimens were then given a further irradiation at 500°C to 5 dpa with a damage rate of $3x10^{-3}$ dpa/sec (B). Another three specimens were irradiated to 5 dpa in 6.75 sec pulses separated by 6.75 sec intervals (C). A total of 247 pulses accumulated at the end of the experiment. The resultant void structures for these irradiations were listed in the previous section in Table 5.

The subsequent irradiations (cases B and C) of the pre-voided samples caused the void radius to grow; from 66 to 96 Å in the steady-state irradiation and from 66 to 121 Å in the pulsed study. The void densities decreased in both of the subsequent irradiations. Even when this is taken into account, it was observed that the total incremental swelling in the pulsed study was over twice that from the steady-state irradiation.

The TRANSWELL code was then used to simulate the conditions outlined in Table 4. The variation in void number density was accounted for by adjusting the value of the void density downwards in a linear fashion for every dpa of accumulated damage. First, the sink density due to vacancy loops in the pulsed

irradiation experiment never reaches such a high level as in the steady-state situation because of annealing between pulses. And second, vacancy loops emit large numbers of vacancies during the annealing period, which can then end in voids without recombination with interstitials. In this beam-off time, vacancy concentration drops slowly to its equilibrium value (which is $>C_v^d$ due to vacancy emission), while the interstitial concentration drops immediately ($\sim 10^{-6}$ seconds) to insignificant levels ($\sim 2.5 \times 10^{-27}$ at/at at 500°C). The slight increase in the equilibrium vacancy flux* (Figure 24) is due to the higher emission of vacancy loops as they shrink. The main parameter of interest, the average void radius, is plotted in Figure (24). Agreement between the void radius predicted by the model and that measured experimentally is good; within 1% for the steady-state irradiation and 10% for the pulsed irradiation. Aside from the absolute numbers, the TRANSWELL Code correctly predicted that the void swelling during this particular pulsed experiment is substantially greater than that observed during steady-state studies.

It is worthwhile repeating that the enhanced swelling in the pulsed case has been found to be due to the behavior of vacancy loops.

A more quantitative description of this effect is shown in Figure (25) where the flux of vacancies and interstitials to the voids is given along with the emission of vacancies from void surfaces during the 100th pulse (1.9943-2.0012 dpa). During the damage pulse, the void grows because the vacancy flux is greater than the combined interstitial and emission fluxes. When the damage pulse is over, D_iC_i drops quickly to 3.16×10^{-29} cm^2/sec, while the emission flux is essentially constant at 1.26×10^{-18} cm^2/sec. The D_vC_v term drops off

*The term "flux" is used for the product of the point defect diffusion coefficient and its fractional concentration (cm^3/s).

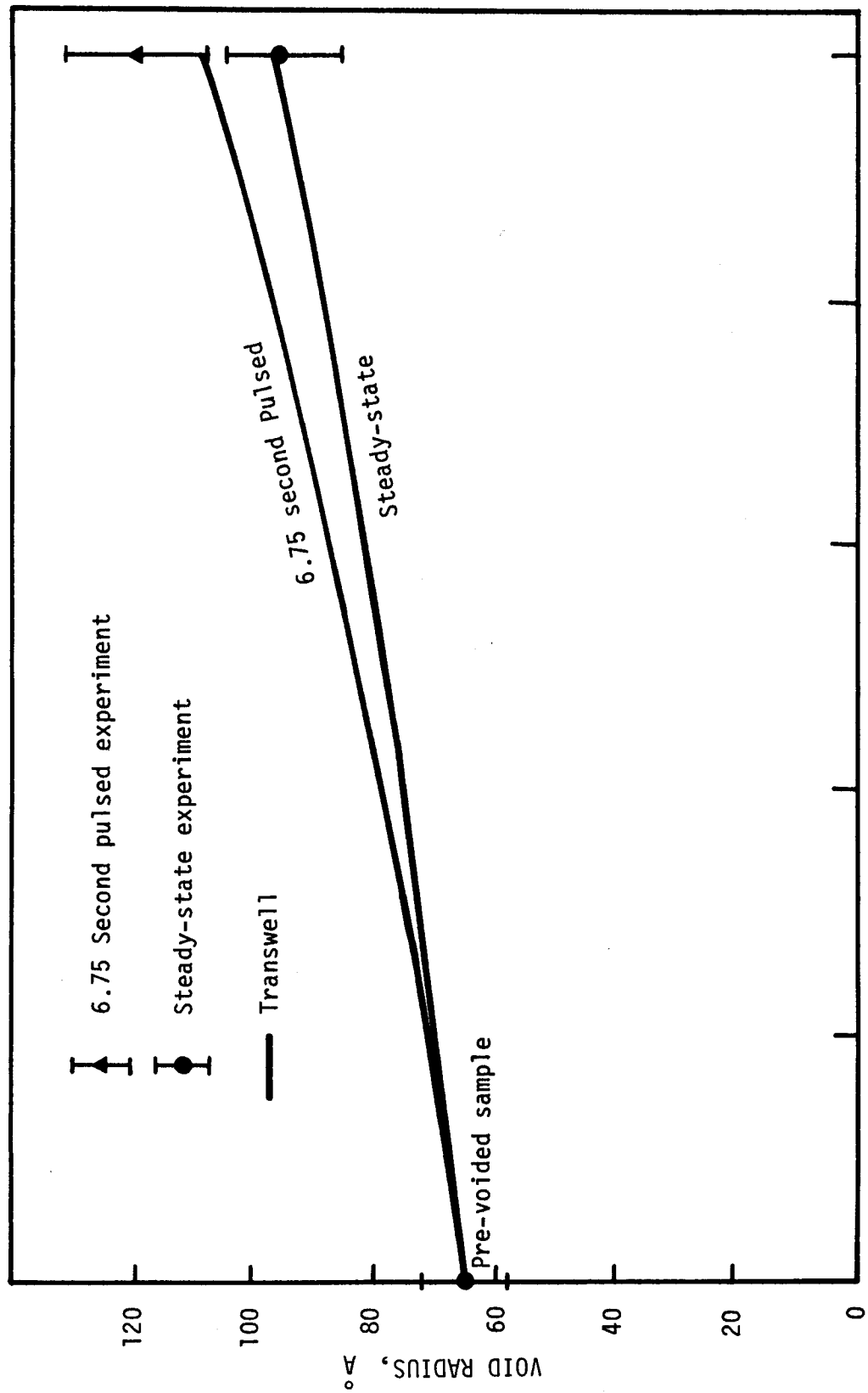

Figure 24. Dose dependence of steady state and pulsed average void radii in self-ion irradiated pure nickel at 500° C. Total dose is 5 dpa, dose rate = 3 x 10-3 dpa/sec and $t_{on} = t_{off} = 6.67$ sec. Data from Ref. 20.

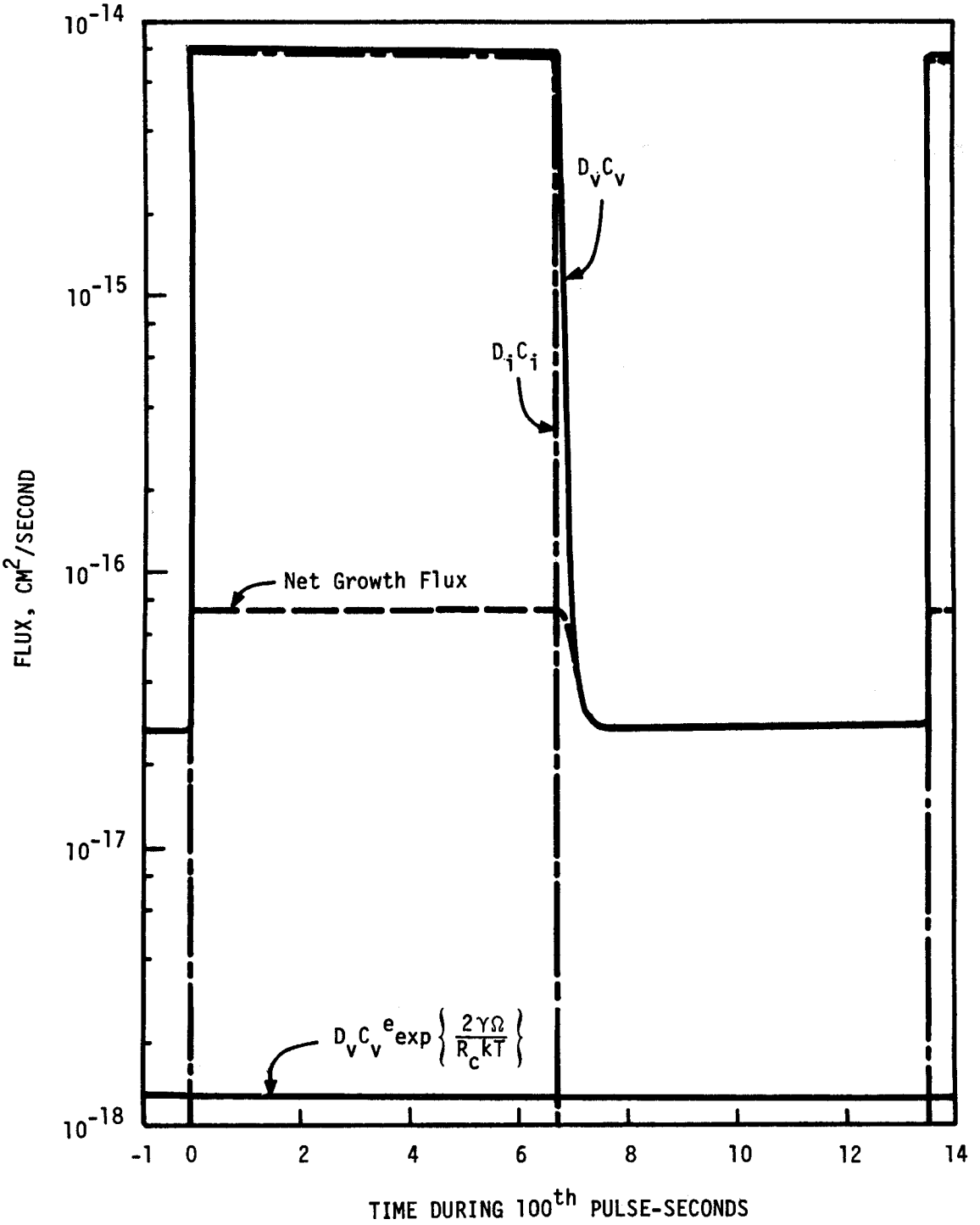

Figure 25. Point defect fluxes near an average void surface during the 100th pulse (0.9943-2.0012 dpa).

slower than D_iC_i, and for the entire 6.75 sec down period, the vacancy flux into the void is greater than the vacancy emission, hence the void continues to grow.

Analysis of the vacancy emission and absorption rates at the end of the annealing period for the 100th pulse of study C indicates that vacancy emission from vacancy loops is the cause of void growth in the interpulse period. The vacancy emission rate from vacancy loops is 9.2×10^{-4} at/at/s while their vacancy absorption rate is 5.9×10^{-4} at/at/s. The excess amount of vacancies injected into the matrix is essentially absorbed at voids and interstitial loops. While voids emit vacancies at the rate of 6.4×10^{-9} at/at/s and interstitial loops at 4.8×10^{-10} at/at/s, vacancies are absorbed at voids with the rate of 1.4×10^{-4} at/at/s and at loops with 1.9×10^{-4} at/at/s. It is this delayed vacancy emission in the absence of free interstitials which accounts for the enhanced growth rate over the steady-state irradiation.

The effects of pulsed irradiation on the swelling of 316 stainless steel first walls in ICFRs were also studied in detail by GK [64] and only the highlights are presented here.

An analysis of point defect behavior in typical Tokamak reactors showed that even for the relatively long burn cycles of these devices, point defects will not reach a steady-state condition. The microstructure, which depends on point defect kinetics, was shown to respond differently to pulsed versus steady irradiation.

In order to illustrate the multitude of possible pulsed damage conditions GK have conducted a parametric study over a wide range of pellet yields keeping the total output of an ICFR constant at 1000 MW_t and the radius of the chamber constant. (In reality the radius would probably increase with increasing pellet yield but for some designs such as the "liquid Li waterfall" proposed

by the LLL group [65] the radius changes might be minor with pellet yield.) A summary of the conditions considered is given in Table 6.

The constant power level of 1000 MW_t dictates that the time between pulses varies from 10 milliseconds for a 10 MJ per pellet yield to 10 s for a 10000 MJ yield. Within each pellet yield-frequency of pulse combination we have allowed the neutron damage to occur over time periods ranging from 1 ns to 1 μs. This should cover reasonable pulse widths from current pellet designs which range from 10-30 ns [66]. The use of a nominal cavity radius of 7 m means that the accumulated displacement damage will vary from approximately 10^{-8} to 10^{-5} dpa per shot or a 10^{-6} dpa/s average displacement rate over time. However, to achieve this average displacement rate the instantaneous damage rate can be as large as 10000 dpa/s for the 10000 MJ pellet with a 1 ns time spread in the neutron arrival rate to 0.01 dpa/s for a 10 MJ pellet yield when the neutrons arrive over a 1 μs time scale. Current pellet designs of 100 MJ indicate ≈10 ns time spreading and a 10 dpa/s damage rate. Higher yield pellet designs would increase the damage rate but since there will be considerable downscattering of the neutrons in these pellets, they will arrive over longer time periods. Anticipated damage rates for a 1000 MJ pellet would be in the 50 dpa/s range. A summary of pulse width and damage rate considerations for a 1000 MW_t reactor is given in Table 6.

Having set up the various time limitations on pulse widths and duration it is now important to consider how these compare to the defect lifetimes. For example, a vacancy mean lifetime can vary between 10^{-4} s at high temperatures (≈0.5 T_m) and high defect sink densities to 1 second at low temperature (≈0.3 T_m) and low sink densities. On the other hand, interstitial mean lifetimes can vary between 10^{-7} s at high temperatures and high sink densities to

TABLE 6

SUMMARY OF PULSE WIDTH AND DAMAGE RATE CONSIDERATIONS FOR A 1000 MW_t REACTOR

Case	Time Between Pulses (s)	Pellet Yield (MJ)	Pulse Width (s)	dpa/shot at 7 m.	Av. Dose Rate in Pulse (dpa/s)
1	10	10,000	10^{-9}	10^{-5}	10,000
			10^{-8}		1,000
			10^{-7}		100
			10^{-6}		10
2	1	1,000	10^{-9}	10^{-6}	1,000
			10^{-8}		100
			10^{-7}		10
			10^{-6}		1
3	0.1	100	10^{-9}	10^{-7}	100
			10^{-8}		10
			10^{-7}		1
			10^{-6}		0.1
4	0.01	10	10^{-9}	10^{-8}	10
			10^{-8}		1
			10^{-7}		0.1
			10^{-6}		0.01

10^{-5} s at low temperatures and low sink densities. Using the following notation: τ_i, interstitial mean lifetime in seconds; τ_v, vacancy mean lifetime in seconds; P_w, pulse width in seconds; Δt, pulse period in seconds, we find that there are four combinations of these parameters that might be important in pulsed fusion reactors.

$$(1)\ P_w < \tau_i < \tau_v\ , \qquad (2)\ \tau_i < P_w < \tau_v\ , \tag{46}$$

$$(3)\ \tau_i < \Delta t < \tau_v\ , \qquad (4)\ \tau_i < \tau_v < \Delta t\ . \tag{47}$$

We will now study the case of 1 pulse every 10 s with two different pulse widths, 1 ns and 1 μs. As an example, we will consider 316-SS as in our previous example. At low temperatures (400°C) the vacancy concentration during the pulse increases rapidly with time irrespective of pulse width as shown in Fig. 26. The vacancy concentration starts to decline from the high value achieved

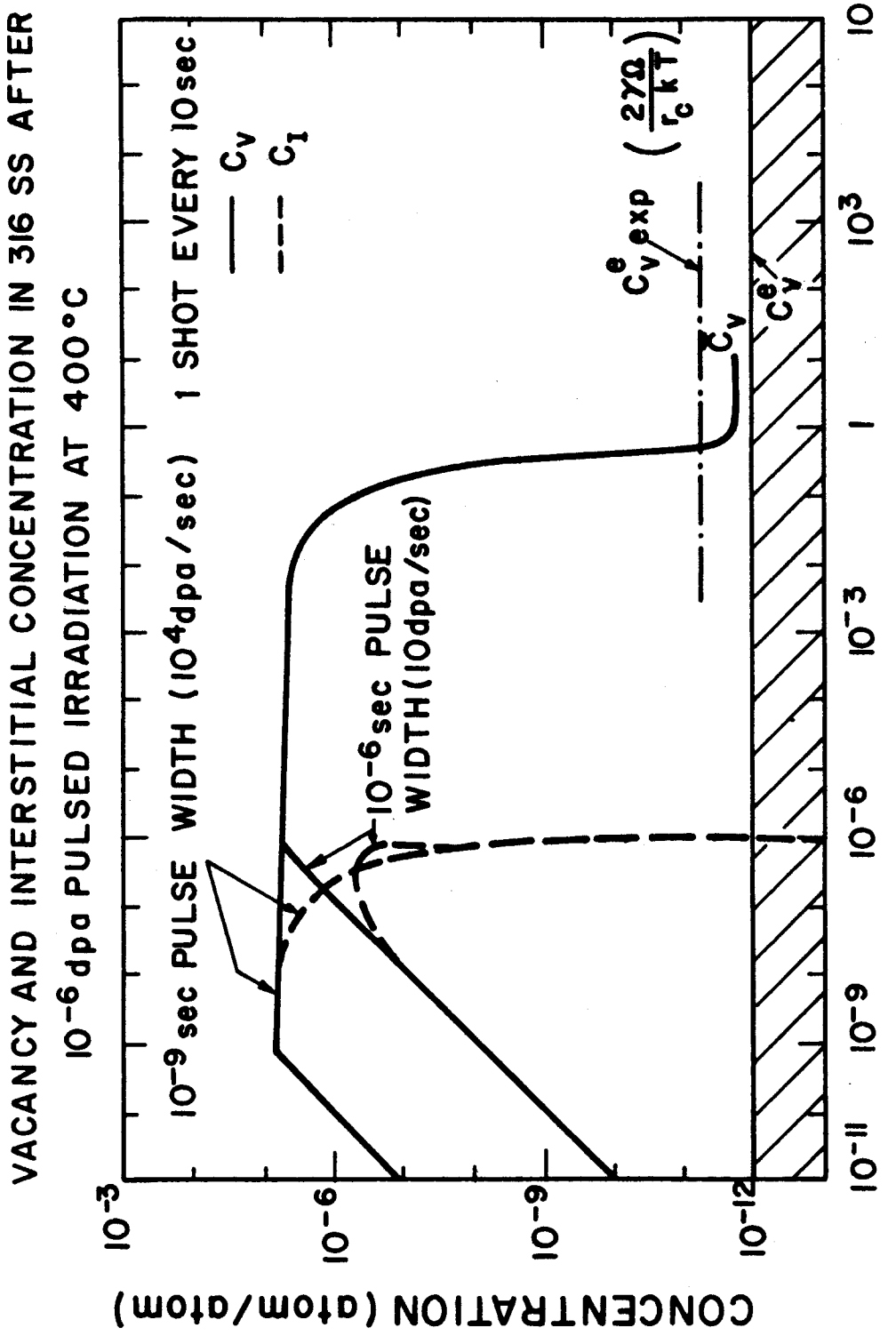

Figure 26 - Point defect concentrations in 316 SS for a 10^{-6} dpa pulsed irradiation at 400°C.

during the pulse ($\approx 10^{-5}$ at/at) to its equilibrium concentration, $\bar{C}_v$, at about 2 ms. The results in Fig. (26) indicate that the pulse width, and hence the details of the damage rates inside the pulse, have no effect on the vacancy concentration after the end of the pulse as $C_v \approx 10^{-5}$ for both cases. On the other hand, interstitial concentration increases linearly with time only for short pulses (10^{-9} s). The interstitial concentration tends to level off after about 10^{-7} s of a 10^{-6} s pulse because of the high interstitial mobility to sinks. Therefore, the interstitial concentration is dependent on the pulse width during the pulse.

At higher temperatures (600°C) the metal matrix contains less voids and dislocations, which in turn allows a higher interstitial concentration. As shown in Fig. (27), interstitials and vacancies exist with almost equal concentrations until the end of the pulse. This aspect enhances point defect mutual recombination and causes a considerable decrease in the vacancy concentration around 1-10 μs. It is observed from Fig. (26) that there is not effect of pulse width on the behavior of either point defect after about one microsecond. Finally the vacancy mean lifetime is a little shorter at the higher temperature ($\approx$15 ms at 600°C) which means that the vacancy concentration does not change significantly until around 10^{-2} s.

Another important feature of Figure (27) is that the vacancy concentration in the matrix does not reach the thermal equilibrium value, C_v^e, until a long time after the irradiation is turned off. Rather, it reaches an average value, $\bar{C}_v$, determined by the existing microstructure (voids and dislocations) and temperature. The vacancy concentrations on the surface of a void of radius R_c, in the absence of stresses and gas atoms inside, is determined by the simple expression:

$$C_v = C_v^e \exp(2\gamma\Omega/R_c kT) \quad . \tag{48}$$

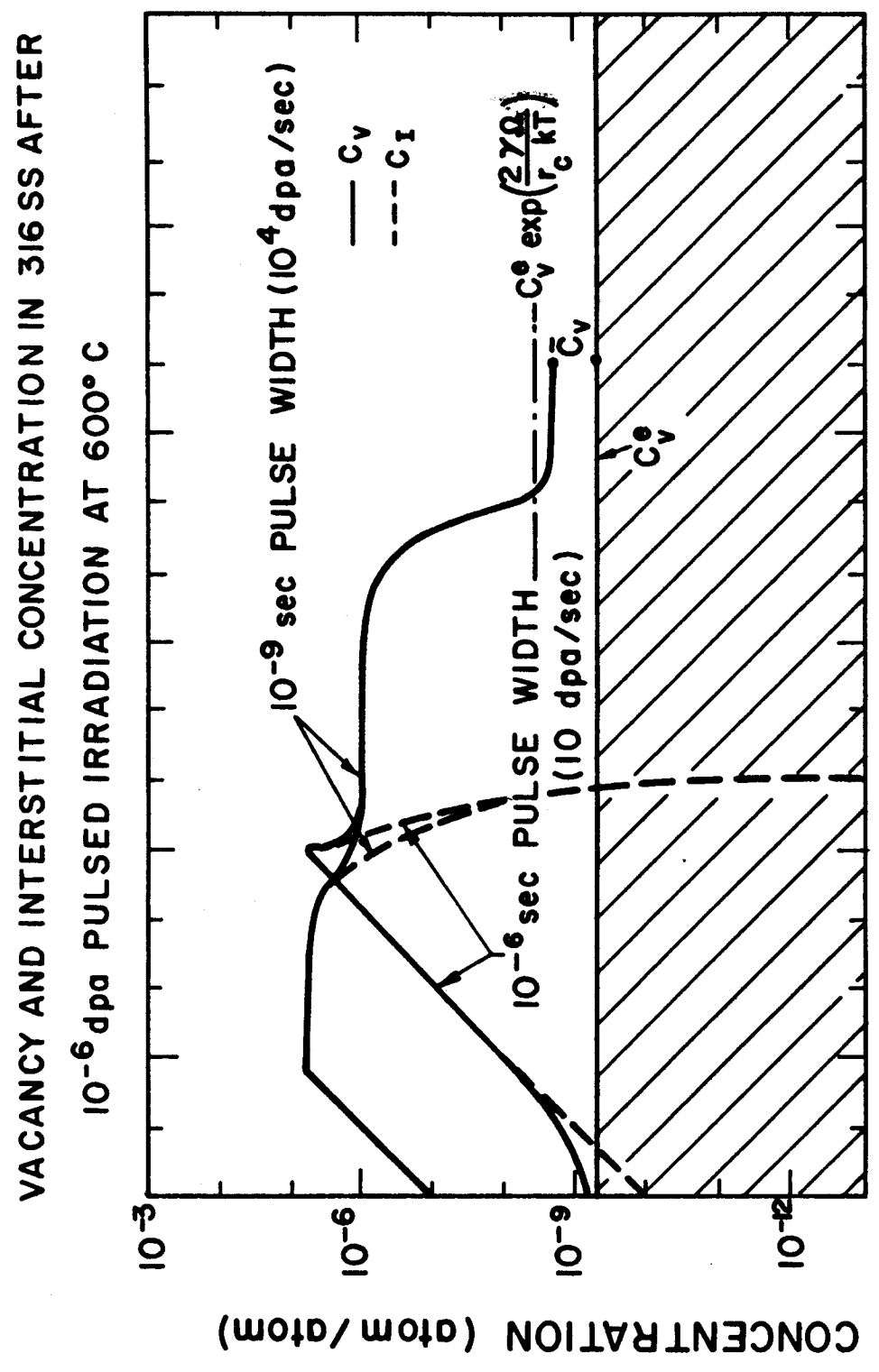

Figure 27 - Point defect concentrations in 316 SS for a 10^{-6} dpa pulsed irradiation at 600°C.

Due to the presence of dislocations, grain boundaries and free surfaces, the average matrix thermal vacancy concentration is smaller than the value given by expression (48). This creates a vacancy concentration gradient between the void surface and the bulk of the metal. A flow of vacancies from the void surface to the bulk of the metal is then set up, tending to reduce the void size.

A sensitivity study of the void growth kinetics in ICFRs for material and irradiation variables was then conducted by GK [64]. They examined the effects and pulse width and irradiation temperature on the void kinetics during one pulse. Then a study of the combined effects of temperature and pulse repetition rate on the kinetics due to a train of neutron pulses were explored. Pulsing was found to shift the high temperature void swelling cut-off value to lower temperatures. These important conclusions are summarized in Fig. (28), where the boundary between void growth and no growth conditions is given as a function of pulsing variables. In steady-state irradiation, this temperature is about 625°C for stainless steel at a dose rate of 10^{-6} dpa/s. The other extreme is that of a 10 s period between pulses which has a high temperature cut-off limit of only 575°C.

The following conclusions were drawn from GK's work [64].

1. Steady-state response of metals is not always achieved for pulsed systems. Even for systems with long burn cycles (i.e., tokamaks), point-defect concentrations, at the start and sometimes at the end of the cycle, are different from their steady-state values.

2. Annealing of voids in metals between shots is not only a function of the annealing temperature, but also a function of the microstructure present.

Figure 28

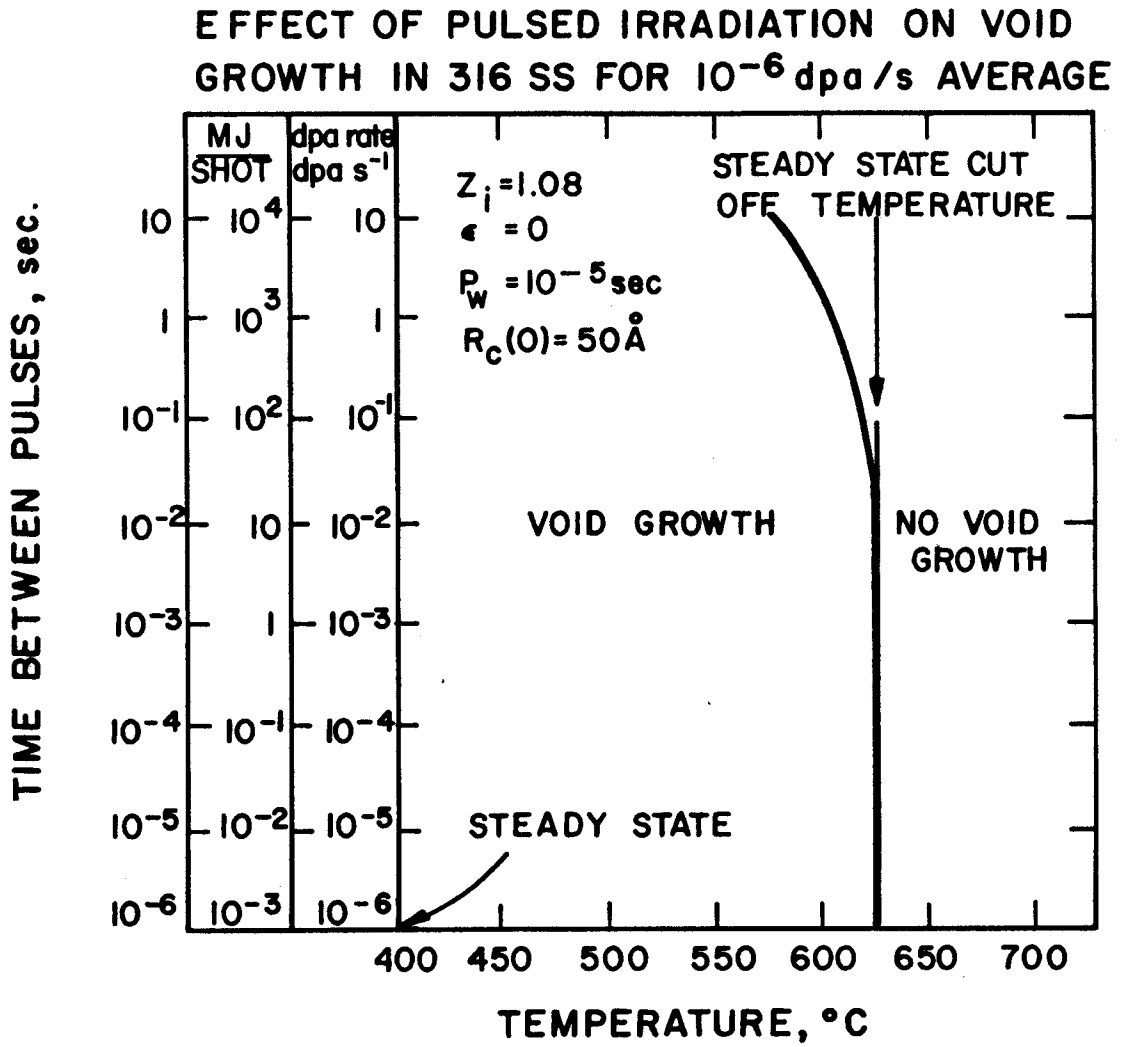
EFFECT OF PULSED IRRADIATION ON VOID GROWTH IN 316 SS FOR 10^{-6} dpa/s AVERAGE
MJ/SHOT
dpa rate dpa s^{-1}
Z_i=1.08
ϵ = 0
$P_w = 10^{-5}$ sec
$R_c(0)$= 50Å
STEADY STATE CUT OFF TEMPERATURE
VOID GROWTH
NO VOID GROWTH
STEADY STATE
TIME BETWEEN PULSES, sec.
10
1
10^{-1}
10^{-2}
10^{-3}
10^{-4}
10^{-5}
10^{-6}
10^4
10^3
10^2
10
1
10^{-1}
10^{-2}
10^{-3}
400 450 500 550 600 650 700
TEMPERATURE, °C

3. For ICFR pulsing conditions and pulse widths ranging from a nanosecond to a microsecond, the time structure of the dose rate during the pulse is not significant in the determination of the final swelling of first-wall materials. The integrated dose within the irradiation pulse is the important damage parameter.

4. The void growth behavior for the first few pulses in ICFRs is not necessarily an indication of the final metal swelling behavior. The void growth behavior has to be studied over a time span of about 1000-5000 τ_v, to determine the ultimate void growth characteristics.

5. Under pulsed irradiation, void growth behavior is a strong function of both the pulse repetition rate, the time between pulses and the irradiation temperature. Voids in stainless steel were shown to exhibit slower growth rates at high temperatures when there are long times between successive pulses. The dividing temperature between growth and no growth of voids can be reduced by as much as 50°C from the corresponding steady-state value, if the time between the pulses is as long as ten seconds.

6. Pulsed irradiation has been shown to be equivalent to steady-state irradiation, for an average dose rate of 10^{-6} dpa/s in stainless steel, only if the pulse repetition rate is greater than 500 pulses per second.

7. It has been found that smaller void radii and lower interstitial dislocation bias factors tend to accelerate interpulse annealing. This causes a lower net growth and further reduces the temperature boundary between growth and no growth conditions.

8. For a fixed operating temperature, geometry and ICFR plant power output, the amount of swelling in the first wall can be reduced by using higher yield pellets. This results from the higher mutual point-defect recombination rates and also because the annealing time between micro-explosions of large yield pellets is longer.

9. For a fixed geometry, ICFR power plant output and pellet yield, the amount of swelling in the first wall can be reduced by operating at the highest temperatures allowed by other design factors (e.g., embrittlement).

The complexity of the numerical solution of rate equations in pulsed problems prompted Ghoniem and Gurol [70] to propose an approximate analytical method to study void growth in ICFRs. The model, however, is restricted to sink-dominant point defect removal. The void growth equation was analytically solved for a series of delta functions representing defect generation in ICFR condtions. Approximating the vacancy emission term in Eq. (48), they obtained analytical results that compared well with previous numerical calculations.

6.2.3 Solute Segregation in Alloys

One of the important effects of high-temperature irradiation on alloys is the spatial redistribution of the alloying elements on a microscopic scale. The local compositional change may lead to precipitation of a new phase or, conversely, cause the dissolution of pre-existing precipitates. These phenomena result from radiation-induced segregation of alloying elements, which has its origin in the preferential coupling between defect and alloy-component fluxes.

Radiation-produced defects in concentrations that exceed the thermodynamic equilibrium concentrations anneal out by mutual recombination and diffusion to internal or external sinks if the temperature is sufficiently high to allow defects to migrate. If there exists a reasonably strong binding between defects and certain types of solute atoms, the defects can interact with those atoms in the process of diffusing to sinks giving rise to a driving force for the transport of solute to sinks. This preferential coupling will set up solute concentration gradients in the vicinity of sinks which, if

sufficiently steep, will then induce back diffusion of solutes to balance the defect-driven solute fluxes, leading to a steady state. If the sinks are enriched with solutes in concentrations greater than the solubility limit, a new phase or precipitate will be formed at the sink-matrix interface. On the other hand, if severe depletion of solute is found at sinks, the bulk region far from sinks can have a sufficiently high solute concentration such that precipitation may take place at preferential sites in the initially homogeneous bulk.

Segregation of substitutional solutes to external surfaces and internal sinks during steady irradiation has recently been investigated experimentally [71,72] and theoretically [73,74]. Theoretical predictions have been in good qualitative agreement with experimental results. In general, segregation under steady irradiation conditions can be understood due to monotonically changing fluxes of defects and defect-solute complexes. Under cyclic conditions, however, the concentration buildups and defect fluxes can change abruptly from one cycle to the next and solute-segregation behavior is somewhat more difficult to predict.

A basic kinetic model has recently been developed by Johnson and Lam, to study radiation-induced solute segregation to sinks in face-centered-cubic metals [75]. The model includes the effects of vacancy and interstitial diffusional encounters with solutes, as well as the formation, the dissociation and the migration of defect-solute complexes. Binding between interstitial and solute atoms is assumed to extend through second-neighbor distances, which leads to two types of bound interstitial solute complexes. The bound complexes labeled "isa" can migrate as a unit without complete dissociation and have a greater binding energy than complexes labeled "isb". Bound complexes "isb" are considered to be immobile. The migration energy of isa complexes is taken as the interstitial migration energy plus three-fifths of

the isa complex binding energy. Binding between a vacancy and a solute atom is assumed to extend to first-neighbor distances. The complex "vs" can migrate without dissociation with an energy equal to the vacancy migration energy. The model casts the segregation phenomenon in the form of combined diffusion and reaction-rate equations. For a detailed discussion of the migration of complexes, the reaction-rate constants and diffusion coefficients, and the resultant rate equations, the reader is referred to the papers of Johnson and Lam [73-75]. The same kinetic model was used to describe the segregation phenomenon under pulsed irradiation, except the beam is on and off in cycles whose duration is a calculational parameter. The boundary conditions have also been modified to account for the precipitation of solute in concentrations above the solubility limit.

Four defect production rates, P = 1 and 10 dpa/s (ICFR irradiation), P = 10^{-3} dpa/s (heavy ion bombardment) and P = 10^{-6} dpa/s (Tokamak or Mirror reactor irradiation) were considered. The temperature was kept at 500°C where appreciable segregation was theoretically found for the damage rates 10^{-3} dpa/s and 10^{-6} dpa/s. The effects of solute back diffusion and beam-off duration were studied at 700°C. The concentrations were calculated for 20 cycles for each set of parameters.

Lam, Leaf, and Johnson calculated the solute concentration profiles for a constant pulse width T_{on} = 1 s and various beam-off durations T_{off} = 10^2, 10^3 and 10^4 s [75]. The temperature was kept at 700°C where the solute diffusivity was high and a dependence of solute segregation on defect-production rate could be observed [75]. They performed the calculations for dilute Ni-base alloys. The profiles obtained for the first and twentieth cycle are plotted in Fig. (29). The solid curves represent the solute concentration profiles at the end of the beam-on period of that cycle and the

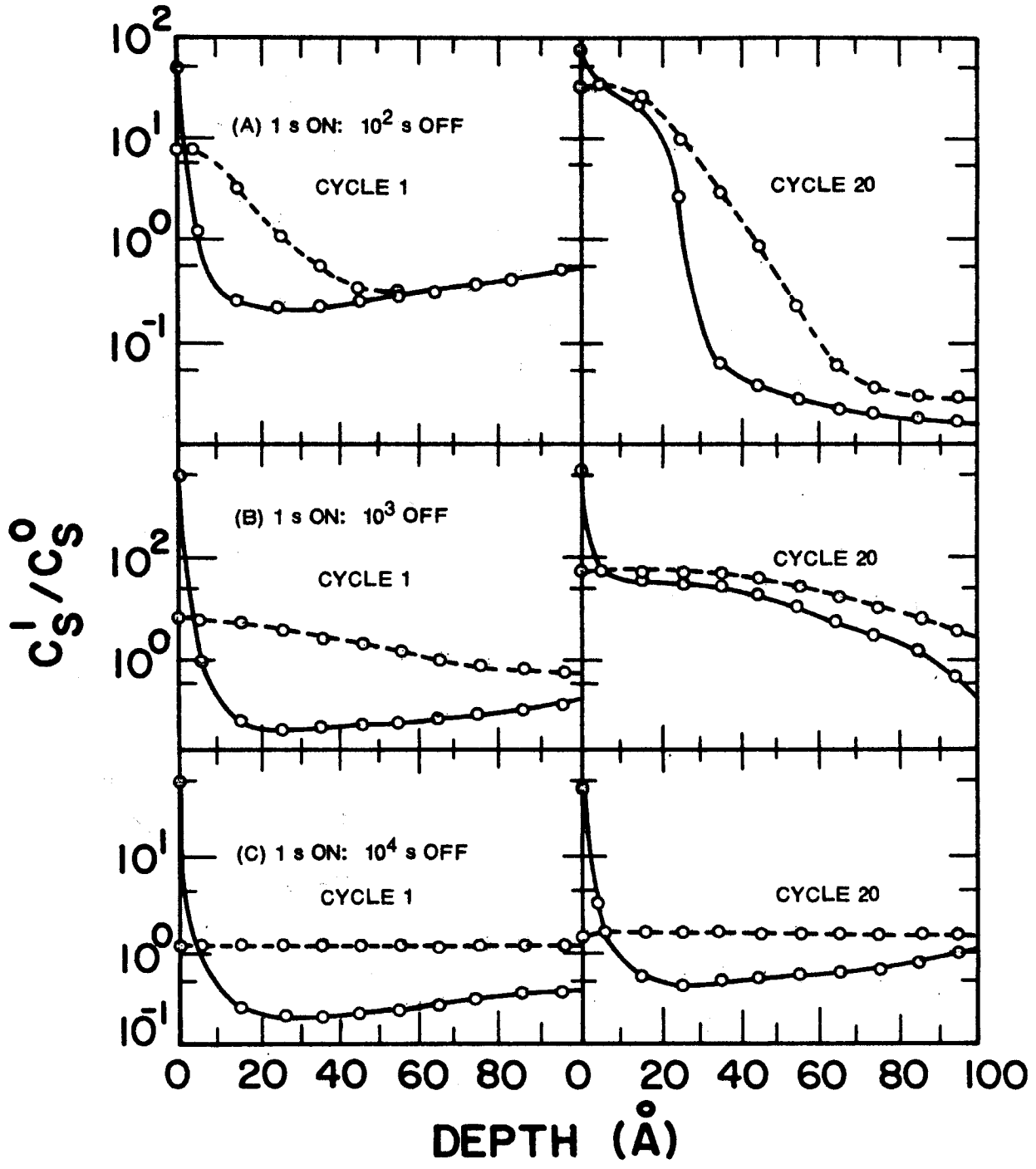

Figure 29 - Spatial distribution of the solutes calculated for the first and the twentieth cycle. The solid curves and dashed lines represent the solute concentration profiles at the end of the beam-on and beam-off periods of the cycle, respectively. T = 700°C, $K_0 = 10^{-3}$ dpa/s, $C_s^0 = 10^{-3}$ and 2000 Å foil.

dashed lines show the profiles at the end of the beam-off period. For relatively short T_{off} ($\leq 10^3$ s, Fig. A and B), the solute atoms do not have enough time to diffuse back to the matrix from the surface high concentration gradient region. Therefore, there exists significant differences between the first cycle profiles and the resultant profiles after the twentieth cycle. With $T_{off} \geq 10^4$ s (Fig. C), back-diffusion of solutes flattens out the solute concentration profiles at the end of each cycle. Consequently, there is no appreciable difference in the profiles from one cycle to another.

The detailed calculations of Lam et al. [75] indicated that for a fixed damage rate, the longer the pulse duration, the smaller the number of cycles needed to achieve a cyclic state (i.e., repetitive pattern of concentration variations from one cycle to another). This applies for point defects, defect-solute complexes, and a quasi-steady-state for solute segregation. For a fixed pulse duration, the higher the damage rate the fewer cycles required to observe the cyclic state. The quasi-steady-state solute segregation obtained under pulsed irradiation is similar to segregation achieved during steady bombardment depending on if the beam-off period is comparable to the pulse width. If the beam-off period is longer than the pulse width, then the solute segregation state is different than the steady-state conditions.

The cyclic changes in the concentrations of single defects and complexes result in a dynamic variation in the magnitudes of defect fluxes to sinks as well as defect recombination rates. Thus, microstructures can be produced that are different from those observed under continuous irradiation. In order to see the distinction between the effects of pulsed and steady-state irradiations, the pulse duration must be considerably less than the buildup time to steady-state measured for the steady case. An increase in the temperature of the system will increase the mobility of defects and defect-solute

complexes, and all kinetic processes will take place on shorter timescales. Therefore, for a constant damage rate, the higher the temperature the shorter the pulse duration must be in order to produce observable effects of cyclic irradiation.

The results of Lam et al., also suggest that theoretical calculations of the time evolution of microstructures performed for a single irradiation cycle can give unrealistic results. In order to study real effects of pulsed irradiation, the concentrations of all species of interest must be calculated as a function of time, over several irradiation cycles, until a cyclic state of concentrations is achieved.

7. EFFECTS OF PULSED IRRADIATION ON THE MECHANICAL PROPERTIES

This area has attracted the least attention from both experimental and theoretical investigators. Nevertheless, the accurate prediction of the mechanical behavior of reactor structural materials is of utmost importance to the designer. The difficulty of constructing a mechanistic model for mechanical properties is obvious, since any model will include a multitude of parameters and atomistic processes that are rarely well known. However, irradiation creep is one exception that has been predicted with reasonable success.

In particular, Simonen and Hendrick have focused on identifying a creep mechanism which would be compatible with their experimental results [45].

The thrust of the present discussion is on identifying a creep mechanism which is compatible with the experimental observations. The two models which they examined in detail were stress induced preferential absorption commonly referred to as SIPA and enhanced climb-glide creep. The basis for both models was the solution of the chemical rate equations for vacancies and interstitials. The two theories differ mechanistically in the origin of the

observed strain. With SIPA, the creep deformation is a result of excess precipitation of interstitials on planes normal to the stress axis. The partitioning of interstitials on these planes is driven by a stress induced interstitial bias; i.e., the sink efficiency of a dislocation is dependent on the dislocation orientation. In the climb-glide interpretation the deformation is a result of glide of dislocations which have been liberated from pinning sites by radiation-enhanced dislocation climb. The basis for calculating the climb-glide enhanced creep is the calculation of the net flux of point defects to dislocations, i.e., the climb rate.

The presence of the cyclic radiation environment in their work requires calculating the point defect histories as they vary for each irradiation cycle. The time dependent rate equations were solved with the computer package GEAR-B [76]. The rate algorithms and material constants for nickel provided by Yoo were used [77]. The only sinks assumed to be present in the material were a uniform distribution of dislocations such that one-third of them had a preferred orientation relative to the stress axis. Neglecting thermal emission, they solved the equations:

$$\frac{\partial C_i}{\partial t} = P - \alpha C_i C_v - A_i^A D_i C_i \rho_d^A - Z_i^O D_i C_i \rho_d^N \tag{49}$$

$$\frac{\partial C_v}{\partial t} = P - \alpha C_i C_v - Z_v^O D_v C_v (\rho_d^A + \rho_d^N) \tag{50}$$

$$\Delta Z_i = Z_i^A - A_i^O \tag{51}$$

$$\rho_d = \rho_d^A + \rho_d^N \tag{52}$$

The defect production rate, P, is calculated from the test beam flux. D and C are the defect diffusivities and concentrations, respectively. The total dislocation density, ρ_d, was divided between aligned, ρ_d^A, and non-aligned, ρ_d^N, dislocations. The defect bias in the absence of stress is shown by Z_i^O and Z_v^O.

The interstitial bias for aligned dislocations is Z_i^A such that the change in bias caused by stress is ΔZ_i. α is the recombination constant.

They expressed the SIPA creep rate $\dot{\varepsilon}_{SIPA}$ as [78]

$$\dot{\varepsilon}_{SIPA} = \frac{2}{9} \rho_d D_i C_i \Delta Z_i \tag{53}$$

and the enhanced climb-glide creep rate [79] $\dot{\varepsilon}_{cg}$ as

$$\dot{\varepsilon}_{cg} = \rho_d (\ell^*/h) b |V_c| \tag{54}$$

where V_c, the climb velocity, is shown by Mansur [78] to be in the absence of thermal emission

$$V_c = \frac{2}{3b} (Z_i^A D_i C_i - Z_v^O D_v C_v) \quad . \tag{55}$$

ℓ^* and h are the obstacle spacing and height, respectively, and b is the Burgers vector.

Solving the previous set of equations, Simonen and Hendrick concluded that the climb-glide model fits better with the experimental finding that pulsed irradiation increases the primary and secondary creep rates by a factor of about three compared to continuous irradiation. This enhancement has been rationalized with the climb-glide mechanism and fluctuating point defect histories. The conclusion was based on the calculated interstitial bias for dislocations that are either aligned or not aligned with the imposed stress axis. The stress induced bias necessary for the SIPA creep mechanism was too large to be considered realistic.

A theory of enhanced high temperature cyclic creep was recently formulated by Weertman and Green [80]. The creep rate enhancement under a superimposed cyclic stress, and without irradiation, was investigated. The mechanism that produces the enhancement in their theory was considered to involve the self-interstitial atoms that are created at jogs on moving screw dislocations.

Their analysis incorporated an athermal interstitial atom production rate that is significantly enhanced by cyclic stresses. They attempted to calculate this generation rate by assuming that the cyclic stress is so large that each dislocation source near a free surface or grain boundary creates at least one new dislocation loop each half cycle. They also assumed that such loops do not contract during the reverse cycle, that a new loop of opposite character is created during the reverse cycle, and that this loop expands and annihilates the previous loop. After annihilation of vacancies a net number of interstitials was considered to remain in existence.

Weertman and Green showed that the interstitial atoms produced athermally at jogs on screw dislocations (or mixed dislocations) are insufficient in number for them to have any appreciable influence on the steady state creep rate under constant stress conditions. Under cyclic stress conditions they concluded that it may be possible for athermal interstitial production rate to be large enough to cause creep acceleration. For the cyclic stress effect to be important the sample must have a fine grain size (say, of the order of, or smaller than, 0.1 mm) and the temperature must be in a well-defined region. The temperature must be below about one-half the melting temperature because at temperatures above that, thermal creep dominates. On the other hand, the temperature must be above about one-third the melting temperature because creep rates generally are immeasurably small at lower temperatures. In addition the magnitude of the cyclic stress component should be large enough to create, in each alternate stress half cycle, a dislocation loop of character opposite to that of the loop immediately preceding it. Thus, the cyclic stress amplitude should be comparable with or larger than the static stress component. The cyclic stress effect is enhanced by increasing the frequency of the cyclic stress.

A very high generation rate of interstitial atoms and their annihilation at edge-type dislocations was concluded to disrupt the dislocation morphology established under steady state creep conditions when only a small number of athermal interstitial atoms are produced. Because of such a disruption of the most stable dislocation arrangement, the creep rate was found to be increased substantially.

8. CONCLUSIONS AND RECOMMENDATIONS FOR FUTURE WORK

In the previous sections, a chronological review of the effects of pulsed irradiation has been presented. The philosophy was to relate what had already been done to the challenges and compromises confronting fusion reactor designers. If we consider ICFRs as an example, a comprehensive picture of the radiation damage environment has to be established in order to understand the microstructural changes which will be introduced. The spatial and temporal interactions of the different reactor components was shown to have a primary impact on both reactor and pellet designs. Once the effects are understood, the reactor design can be optimized. It is not possible to establish a broad set of conclusions on the basis of what theoretical and experimental work has already been done. Instead we will enumerate the important areas of future research that the past work suggests might be reasonably pursued.

(1) Modifications in the pellet designs of ICFRs can be made in order to optimize the energy partitioning between different pellet debris. This has to be iterated with the reactor design with the objective being an increase in the lifetime of structural materials.

(2) The effects of pulsed irradiation on the near surface behavior of helium bubbles are not well-established. Kaletta's experimental data [43] showed a considerable enhancement of bubble mobility as

well as coalescence rates. This may also have a significant impact on limiters in Magnetic Confinement Fusion Reactors.

(3) It was shown that large temperature and stress transients will simultaneously exist with the displacement damage. It is important to understand if such transients can change the residual (or "free") point defect production rates. Because instantaneous short-term annealing (recombination) of point defects can be influenced by temperature and stress transients, we know that the microstructure will be far from our previous observations of steady-state irradiated metals.

(4) Heavy ions resulting from reactor-grade tamped pellets were found to result in very high instantaneous displacement rates in ICFRs. The influence of cascade spatial overlap on the final production rate of surviving defects needs to be established.

(5) Point defects are generated in collision cascades that produce local pulses of vacancy and interstitial fluxes. The effects of inhomogeneous spatial point defect production during pulsing is not yet understood.

(6) It has been shown that the high temperatures resulting from the energy deposition in ICFR first walls will result in annealing the near-surface microstructures. This can result in very low sink densities for point defects, and therefore the spatial diffusion of the point defects in such a "clean" matrix should be considered.

(7) The high rate of α-particle implantation near the surface of the ICFR first wall will most probably result in bubbles rather than voids. The behavior of those bubbles in the high temperature (and possibly stress) transients needs to be considered.

(8) It is possible that high temperature transients which approach the melting point for a small fraction of time can have a considerable influence on enhancing temperature sensitive phenomena such as grain growth. If larger grains will result as a consequence of pulsing, the mechanical strength of the first wall can be degraded. It is important to understand microstructure phenomena that are especially sensitive to high temperatures.

(9) Although separate microstructure nucleation and growth models are informative in their own right, they can be misleading as to the total picture. Phenomena predicted by some growth models may be negated by the fact that the same environment could suppress nucleation of the defect in the first place. Comprehensive microstructure evolution models are extremely important in this area.

(10) There is a general lack of both theoretical and experimental investigations in the area of mechanical behavior associated with pulsed fusion reactor first walls.

(11) There is a general need for more carefully planned experiments which are coupled to verification of theoretical models. At the same time, data interpretation with the aid of models based on fundamental mechanisms can be beneficial to both experiment and theory. This emphasizes the fact that the pulsed irradiation damage field is still in the basic science mode and we are far from alloy and materials optimization studies.

Acknowledgement

Partial support for this work was provided by the United States Department of Energy, Division of Laser Fusion.

REFERENCES

1. B. Badger, et al., "UWMAK-III, A Non-Circular Tokamak Power Reactor Design", Electric Power Research Inst. Report ER-368, EPRI, July (1976).

2. R. W. Moir, et al. "Preliminary Design Study of the Tandem Mirror Reactor (TMR)", UCRL-52302, July (1977).

3. B. Badger, et al. "NUWMAK, A Tokamak Reactor Design Study", Univ. of Wisconsin, Fusion Design Report, UWFDM-330, March (1979).

4. L. A. Booth, "Central Station Power Generation by Laser-Driven Fusion", LA-4858, Vol. 1, Los Alamos Scientific Laboratory, February (1972).

5. G. L. Kulcinski, "Radiation Damage by Neutrons to Materials in DT Fusion Reactors", IAEA-CN-33/S 3-1; Reprint from Plasma Physics and Controlled Nuclear Fusion Research, 1974, Vol. II, International Atomic Energy Agency, Vienna, (1975).

6. G. L. Kulcinski, et al. "Comparison of Displacement and Gas Production Rates in Current Fission and Future Fusion Reactors", Special Technical Production 570, American Society for Testing and Materials (1976).

7. F. H. Southworth and H. D. Campbell, Transactions of the American Nuclear Society, 21 (1975) 15.

8. T. D. Beynon and G. Constantine, Journal of Physics G: Nuclear Physics, 1 (1975) L23.

9. F. Beranek and R. Conn, to be published.

10. S. A. Dupree, et al. "Time Dependent Neutron and Photon Transport Calculations Using the Method of Discrete Ordinates", Joint Los Alamos Scientific Laboratory and Oak Ridge National Laboratory Report LA-4557 (ORNL-4662) (1971).

11. M. Ragheb and R. Lewis, to be published.

12. M. Ragheb, G. A. Moses, and C. W. Maynard, "Pellet and Pellet-Blanket Neutronics and Photonics for Electron-Beam-Fusion Microexplosions," Univ. of Wisconsin Fusion Design Report UWFDM-295 (1979).

13. T. O. Hunter and G. L. Kulcinski, "Description of the Response of Materials to Pulsed Thermonuclear Radiation (Part II)", Univ. of Wisconsin Fusion Design Report UWFDM-217 (1977).

14. J. Lindhard, et al. "Range Concepts and Heavy Ion Ranges", Mat. Fys. Medd. Dan. Vid. Selsk, 33, No. 14 (1963).

15. M. Robinson, Proc. of Conf. on "Radiation Induced Voids in Metals", J. W. Corbett and L. C. Ianniello, eds., National Technical Information Service, CONF-710601, p. 397 (1973).

16. D. G. Doran, et al., Report of Working group on Displacement Models and Procedures for Damage Calculations, Hanford Engineering and Development Laboratory Report, HEDL-TME-73-76 (1973).

17. D. K. Brice, "Ion Implantation Range and Energy Deposition Codes: COREL, RASE4 and DAMG2", Sandia Laboratory Report, SAND75-0622 (1977).

18. T. O. Hunter and G. L. Kulcinski, J. Nucl. Mat., 76 (1978) 383.

19. G. L. Kulcinski, "First Wall Protection Schemes for Inertial Confinement Fusion Reactors", Proc. of First Topical Meeting on Fusion Reactor Materials, Miami Beach, FL; Jan. 29-31 (1979).

20. T. Frank, D. Freiwald, T. Merson and H. Devaney, Proc. First Topical Meeting on Tech. Controlled Thermonuclear Fusion, G. R. Hopkins, ed., CONF-740402-P1 (1974) 183.

21. R. J. Burke, Argonne Report, ENG/CTR/TM-31, (1974).

22. S. G. Vernado and G. A. Carlson, Nucl. Tech., 29 (1976) 415.

23. R. W. Conn, et al. "SOLASE, A Conceptual Laser Fusion Reactor Design", Univ. of Wisconsin Fusion Design Report, UWFDM-220 (1977).

24. T. O. Hunter and G. L. Kulcinski, "Description of the Response of Materials to Pulsed Thermonuclear Radiation (Part III)", Univ. of Wisconsin Fusion Design Report, UWFDM-232 (1978).

25. T. J. McCarville, A. M. Hassanein and G. L. Kulcinski, "The Response of Stainless Steel to the Pellet Debris in a Laser Fusion Reactor", Univ. of Wisconsin Fusion Design Report, UWFDM-282 (1978).

26. J. Hovingh, "First Wall Studies of a Laser-Fusion Hybrid Reactor Design", Proc. of 2nd Topical Meeting on the Technology of Controlled Nuclear Fusion, Richland, WA (1976).

27. D. K. Brice, "Three-Parameter Formula for the Electronic Stopping Cross-Section at Non-Relativistic Velocities", Physical Review A, 6, No. 5 (1972).

28. M. A. Abdou, C. W. Maynard and R. Q. Wright, "MACK: A Program to Calculate Neutron Energy Release Parameters (Fluence-to-Kerma Factors) and Multigroup Neutron Reaction Cross Sections from Nuclear Data in ENDF Format", ORNL-TM-3994, also Univ. of Wisconsin Fusion Design Report UWFDM-37 (1972).

29. W. W. Engle, Jr., "A User's Manual for ANISN", K-1693 (1967).

30. H. S. Carlslaw and J. C. Jaeger, Conduction of Heat in Solids, 2nd ed., Oxford (1959).

31. T. O. Hunter and G. L. Kulcinski, Univ. of Wisconsin Report, UWFDM-247 (1978).

32. I. O. Bohachevsky, Los Alamos Laboratory Report, LA-7014-MS (1977).

33. T. O. Hunter and G. L. Kulcinski, "Description of the Response of Reactor First Walls to Pulsed Thermonuclear Radiation (Part I)", Univ. of Wisconsin Report, UWFDM-196 (1977).

34. G. Taylor, Proc. Royal Soc., A201 (1950) 159.

35. S. A. Metz and F. A. Smidt, Jr., "Production of Vacancies by Laser Bombardment", Appl. Phys. Lett., 19 (1971) 207.

36. F. A. Smidt, Jr., and S. A. Metz, Proc. of Conf. on Rad.-Induced Voids in Metals, Albany, NY, June 9-11 (1971) 613.

37. H. Kressel and N. Brown, "Lattice Defects in Shock-Deformed and Cold-Worked Nickel", J. Appl. Phys., 38 (1967) 1618.

38. J. A. Sprague and F. A. Smidt, Jr., NRL Memorandum Report 2629 (1973).

39. A. Taylor, et al. Argonne National Laboratory Report, ANL/CTR/TM-39 (1975).

40. A. Taylor, D. I. Potter and H. Wiedersich, Argonne National Laboratory Report, ANL/FPP-79-3 (1979).

41. T. D. Ryan, Ph.D. Thesis, Univ. of Michigan (1974).

42. R. W. Powell and G. R. Odette, "The Effect of Pulsed HVEM Irradiation on Microstructure Evolution in a Simple Fe-Ni-Cr Alloy", Ref. 19 above (1979).

43. D. Kaletta, "The Microstructure of Vanadium Implanted with 2-MeV Helium Ions Under Pulsed Conditions", Ref. 19 above (1979).

44. D. Kaletta, J. Nucl. Mater., 76 & 77 (1978) 221.

45. D. J. Michel, P. L. Hendrick and A. G. Pieper, J. Nucl. Mater., 75 (1978) 1.

46. E. P. Simonen and P. L. Hendrick, "Light Ion Irradiation-Induced Creep Mechanisms in Nickel", Ref. 19 above (1979).

47. I. Manning and G. P. Mueller, Computer Phys. Comm., 7 (1974) 85.

48. P. L. Hendrick, D. J. Michel, A. G. Pieper, R. E. Surratt and A. L. Bement, Proc. of Conf. on Radiation Effects and Tritium Technology for Fusion Reactors, J. S. Watson and F. W. Wiffen, eds., Gatlinburg, TN, 1975, U.S. Department of Commerce, CONF-750989.

49. J. S. Koehler, J. Nucl. Mater., 69/70 (1978).

50. Y. H. Choi, A. L. Bement and K. C. Russell, Ref. 48 above, p. II-1.

51. G. R. Odette and R. Myers, Hanford Laboratory CTR Quart. Prog. Rept., HEDL TME/7590, April-June (1975) p. 2.

52. K. C. Russell, Acta Met., 19 (1971) 753.

53. R. Bateman, Proc. Camb. Phil. Soc., 15 (1910) 423.

54. N. M. Ghoniem and D. D. Cho, Phys. Status Solidi (a), 54 (1979).

55. W. G. Wolfer and M. Ashkin, J. Appl. Phys., 46 (1975) 547.

56. A. C. Damask and G. Dienes, Phys. Rev. 120 (1960) 99.

57. N. Ghoniem, submitted to J. Nucl. Mater.

58. J. O. Stiegler, "Void Formation in Neutron-Irradiation Metals", Ref. 15 above, p. 292.

59. J. O. Schiffgens, N. J. Graves and D. G. Doran, Ref. 45 above, p. I-532.

60. N. M. Ghoniem and G. L. Kulcinski, Univ. of Wisconsin Report, UWFDM-138 (1975).

61. N. M. Ghoniem and G. L. Kulcinski, Rad. Eff., 39, No. 1 (1978) 47.

62. N. M. Ghoniem and G. L. Kulcinski, "TRANSWELL, A Computer Code for Metal Swelling and Creep Under Transient, Pulsed or Steady Irradiation Conditions", Univ. of Wisconsin Report, UWFDM-181 (1976).

63. A. C. Hindmarsh, Lawrence Livermore Laboratory Report UCID-30001, Rev. 3 (1974).

64. N. M. Ghoniem and G. L. Kulcinski, Nuclear Eng. and Design, 52, No. 1 (1979) 111.

65. J. A. Maniscalco, W. R. Meier and M. J. Monsler, Trans. Am. Nucl. Soc., 27 (1977) 34.

66. G. L. Kulcinski, "The Newest Frontier in Radiation Damage Research--Laser Fusion Reactors", Proc. of the Third Topical Meeting on the Technology of Controlled Thermonuclear Fusion, ANS, Santa Fe, NM, 9-11 May (1978).

67. R. Bullough, B. Eyre and R. Krishan, Proc. Royal Soc. London, A-346 (1975) 81.

68. M. J. Makin and G. P. Walters, Proc. of Conf. on Physics of Voids, Harwell, Edited by R. S. Nelson, AERE-R 7934 (1974).

69. N. M. Ghoniem and G. L. Kulcinski, Rad. Eff. 41 (1979) 81.

70. N. Ghoniem and H. Gurol, "An Analytical Approach to Void Growth in Inertial Confinement Fusion Reactor First Walls", submitted to J. Nucl. Mater.

71. P. R. Okamoto, S. D. Harkness and J. J. Laidler, ANS Transactions, 16 (1973) 70.

72. L. E. Rehn, P. R. Okamoto, D. J. Potter and H. Wiedersich, J. Nucl. Mater., 74 (1978) 242.

73. R. A. Johnson and Nghi Q. Lam, Phys. Rev., B13 (1976) 364.

74. Nghi Q. Lam and R. R. Johnson, Nucl. Mat., 20 (1976) 121.

75. Nghi Q. Lam, G. Leaf and R. A. Johnson, J. Nucl. Mater., 74 (1978) 277.

76. A. E. Hindmarsh, Lawrence Livermore Laboratory Report, UCID-30059, Rev. 1, March (1975).

77. M. H. Yoo, J. Nucl. Mater., 68 (1977) 193.

78. L. K. Mansur, Oak Ridge National Laboratory Report, ORNL/TM-6443 (1978).

79. D. J. Michel, P. L. Hendrich and A. G. Pieper, J. Nucl. Mater., 75 (1978) 1.

80. J. Weertman and W. V. Green, J. Nucl. Mater., 68 (1977) 205.

81. N. M. Ghoniem and G. L. Kulcinski, "Void Growth Characteristics in Laser Fusion First Walls", Ref. 16 above (1979).